STUDIA UNIVERSITATIS
BABEŞ-BOLYAI

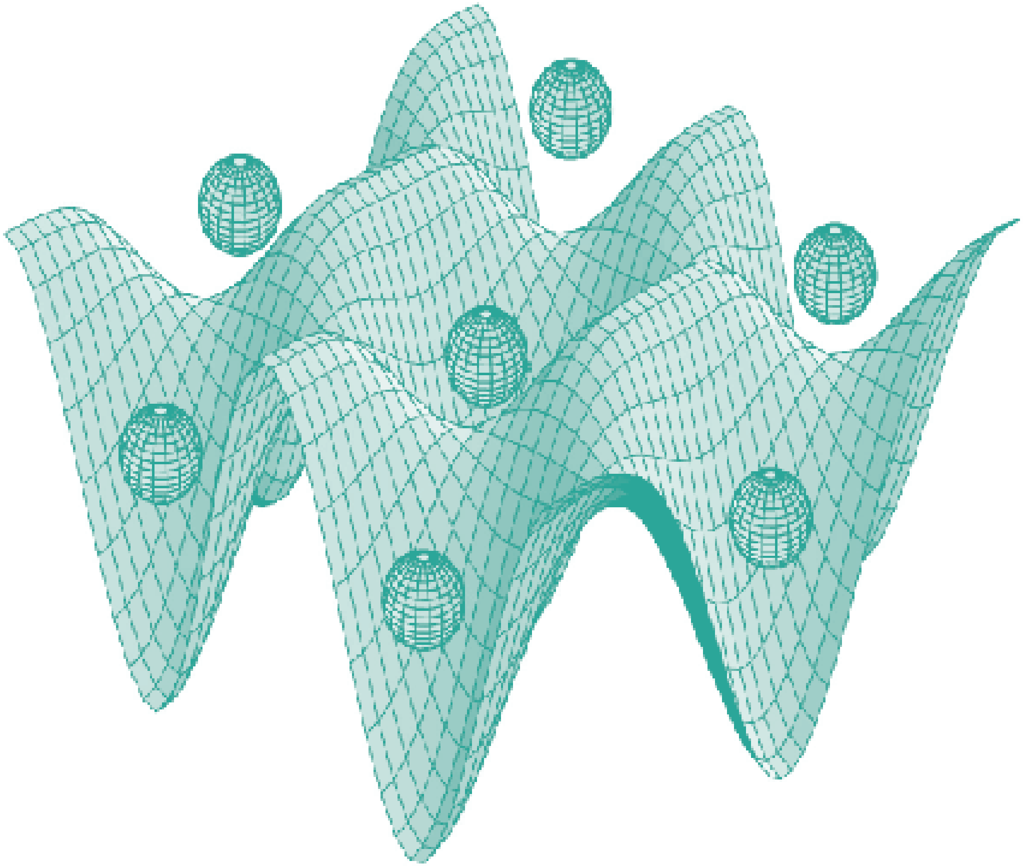

PHYSICA

2/2012

YEAR Volume 57 (LVII) 2012
MONTH DECEMBER
ISSUE 2

STUDIA
UNIVERSITATIS BABEŞ–BOLYAI

PHYSICA

2

Desktop Editing Office: 51st B.P. Hasdeu, Cluj-Napoca, Romania, Phone + 40 264-40.53.52

CUPRINS – CONTENT – SOMMAIRE – INHALT

STUDIA UBB PHYSICA, Vol. 57(LVII), 2, 2012, pp. 3-12
(RECOMMENDED CITATION)

^{63}Cu(n,γ) ^{64}Cu NUCLEAR REACTION CROSS-SECTION MEASUREMENT AT THERMAL NEUTRONS USING ISOTOPIC NEUTRON SOURCES FOR ^{64}Cu PRODUCTION

LAURA DARABAN[a], **C. COSMA**[a], **L. DARABAN**[a,*]

ABSTRACT. The nuclear reaction ^{63}Cu(n,γ)^{64}Cu was applied by irradiation with thermal neutrons in order to obtain the β^+ emitter radioisotope ^{64}Cu ($T_{1/2}$ = 12.7 h), used for medical applications in P.E.T. The irradiation block contains 2 isotopic neutron sources type ^{241}Am-^{9}Be and ^{239}Pu-^{9}Be, inserted in paraffin with a fluence of $6.6\cdot10^7$ n/s. The thermal neutron cross-section was determined from over the thermal neutron spectrum using the activation method. In order to calculate the yield of the reaction, simultaneously the thermal neutron flux was monitorized by using some foils of Au, based on the nuclear reaction ^{197}Au(n,γ)^{198}Au and using cadmium filters in order to limit the thermal neutron spectrum. The calibration in efficiency of the HPGe detector was made by manufacturing some standard sources of ThO_2 with the same size as the irradiated samples, according to a new method. In conclusion, we can produce ^{64}Cu to be used for the P.E.T. application, by using a high flux of thermal neutrons at the nuclear reactor, having enough time to transport it to the clinics.

Keywords: *thermal neutrons, cross section, Cu-64, positron emission.*

1. INTRODUCTION

The isotope ^{64}Cu (Fig. 1), is used as one of the β^+ emitting radioisotopes in nuclear medicine for Positron Emission Tomography, heaving a long half-life (12.7 h). ^{64}Cu was produced at a cyclotron via the reaction ^{64}Zn(d,2p)^{64}Cu [1] and ^{64}Ni(d,2n) ^{64}Cu [2], the excitation function and properties of these reactions being well studied in the first by *the stack foil method* for the production of a medical radioisotope. In the case of ^{nat}Zn target, the total yield for the production of ^{64}Cu by deuteron irradiation is about 26.06 MBq/μAh [1].

---

[a] Faculty of Engineering and Environmental Science, Faculty of Physics, University Babes-Bolyai, Cluj-Napoca, Romania
* Corresponding author: liviu.daraban@phys.ubbcluj.ro

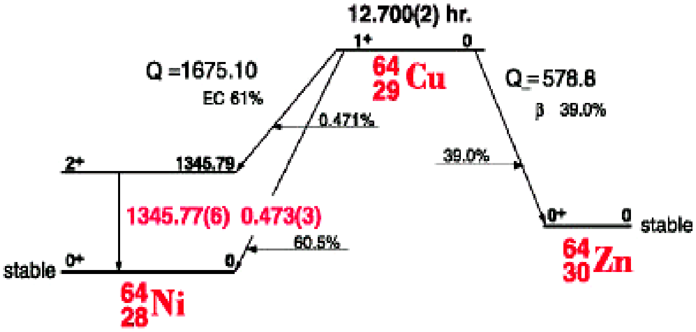

Fig. 1. The disintegration scheme of ^{64}Cu

Due to its suitable decay characteristics ^{64}Cu can be also produced with thermal neutrons in a nuclear reactor using the ^{63}Cu(n,γ)^{64}Cu reaction. The accurate knowledge of the thermal neutron cross-section and resonance integral of this reaction become very important when producing ^{64}Cu [4-6] with thermal neutrons for P.E.T. applications.

Usually, thermal cross-sections and resonance integrals (Fig.2) can be determined experimentally by using the *activation method* [7], which consists of a foil activation and comparison of the cadmium (Cd) ratios for the foils (copper) to the cadmium ratios of a reference monitor material, such as gold foils. ^{113}Cd is used because of its cut-off property meaning that at 0.55 eV neutron energy thin Cd foils act as thermal neutron filters (Fig.3).

For thermal neutrons cross section determination the gold foils was used as flux monitor by standard monitor reaction ^{197}Au(n,γ)^{198}Au with the well known ^{198}Au radioisotope ($\sigma_0 = 98.65 \pm 0.09\ b$, $I_0 = 1550 \pm 28\ b$).

The method consists of irradiating 2 thin foils, one has a known cross-section as a monitor foil. For example Au or In reactions are suitable as monitors due to their cross-sections, have a 1/v dependence up to 1-2 eV. The 2 foils were irradiated in the same position in a sandwich type geometry, were then covered with 1 mm thick Cd covers foil in order to separate the thermal neutron activation from the epithermal neutron activation [8]. After calculating the reaction rates for each of the uncovered foil and the Cd covered foils, the cadmium ratios were determined.

It is also known that characterizing a highly intense field of neutrons can be difficult, mainly because of the burn-up effects that occur in the ^{197}Au monitor foil, resulting from the fact that the activities induced by neutrons will no longer be proportional to the neutron flux.

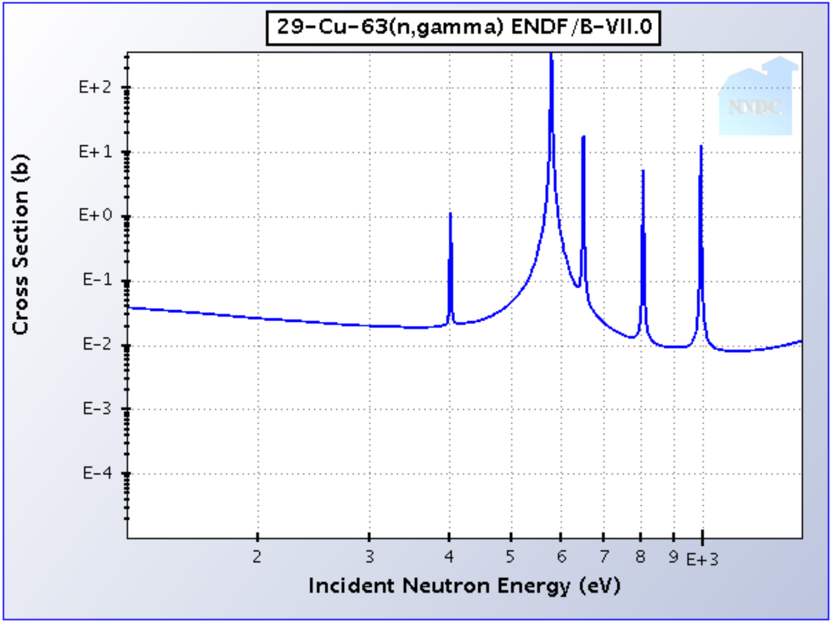

Fig. 2. Cooper total cross-section in function of the neutrons energy

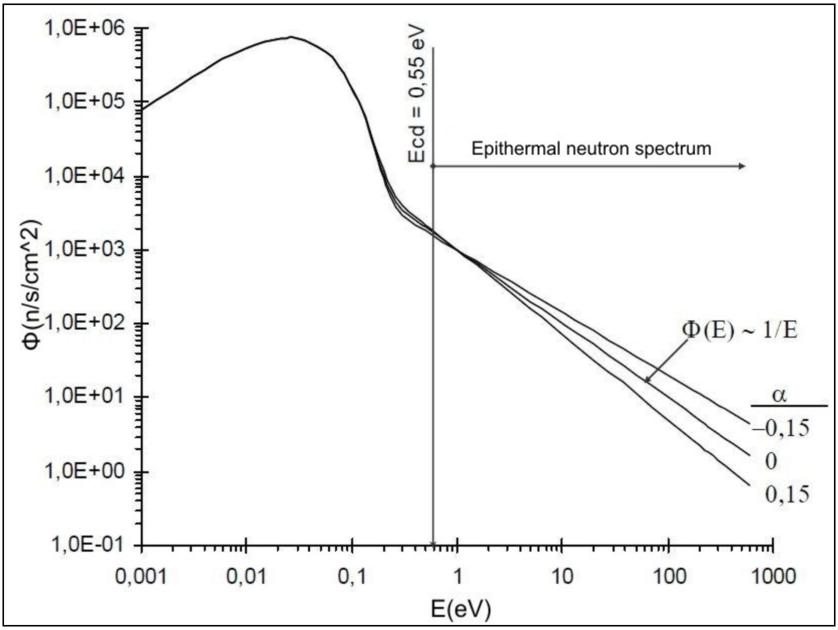

Fig. 3. Deviation from the ideal *1/E* epithermal neutron spectrum [8]

2. EXPERIMENTAL

2.1. Neutron irradiation facility

It has been shown by Karadag et al. [9] that a lower neutron flux (lower than that of a nuclear reactor) can be used when producing nuclear reactions and calculating cross-sections and resonance integrals. In our case, the neutron field of two isotopic neutron sources, *^{241}Am-^{9}Be* and *^{239}Pu-^{9}Be,* was used. Also, the ^{197}Au monitor foil can be used, while ^{197}Au has its first main resonance at 4.9 eV [10], which is near to the 1/v region of the cross-section and thus the activity induced by the epithermal and thermal neutrons can not be well separated.

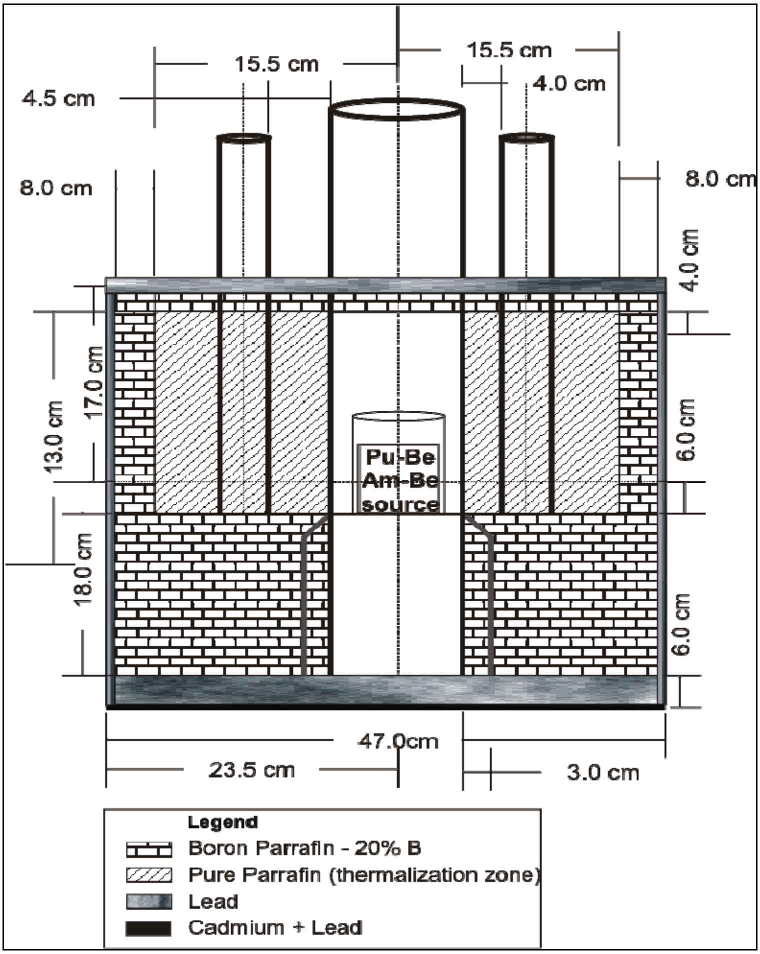

Fig. 4. Irradiation bloc scheme with ^{241}Am-^{9}Be and ^{239}Pu-^{9}Be isotopic neutron sources

In our measurements we used Cu and Au metallic foils that were irradiated in the neutron field produced by the two isotopic neutron sources in the Nuclear Physics Laboratory of the Faculty of Physics at UBB Cluj-Napoca, Romania. Metallic foils samples were used for irradiation in a sandwich geometry Cu-Au, covered with a Cd foil. In order to obtain results as accurate as possible, several corrections had to be made. Then, they were exposed to the thermal neutron flux in one of the side being inserted in the irradiation holes in paraffin block, as it can be seen in Fig. 4. The neutron field was obtained from 2 isotopic neutron sources, immersed in paraffin and covered with a cylindrical lead shield, ^{241}Am-^{9}Be with an activity of 5 Ci and ^{239}Pu-^{9}Be with an activity of 33 Ci, having a total fluence of $6.6\cdot10^{7}$ n/s.

The characteristics of the irradiated samples are given in Table 1. The foils were irradiated and another set of samples were covered in Cd case shields of 1 mm thickness. This procedure is known as the *cadmium ratio method* and it is described in [7].

2.2. Photopeak efficiency of the spectrometer

The induced activities of the samples were then measured with the help of the gamma spectrometry using a GC1519 HPGe Detector (germanium coaxial type detector Canberra), having a measuring interval between 50 keV and 1500 keV, in conjunction with a Multiport II multi-channel analyzer (MCA) and the Genie2000 gamma spectroscopy software.

In order to calibrate the detector in efficiency, according to formula (1), standard sources were used.

$$\varepsilon = N/(t\ .\Lambda\ .p) \tag{1}$$

where: ε – the energetic efficiency;

N – the peak area in number of counts at that energy;

Λ – the absolute activity of the standard sample [Bq];

t – the measurement time;

p – the disintegration probability of the radioisotope at that energy;

It can be noticed that there are few measurement points on the graph, therefore we used another source of ^{226}Ra with known activity of 3,33 kBq, which emits many energies in secular equilibrium with its descendants. The efficiency of the detector was therefore determined with the help of the known activities of standard point sources such as: ^{60}Co, ^{137}Cs, ^{241}Am, ^{133}Ba, ^{226}Ra.

By applying formula (1), the N peak areas can be read on each peak with energy E and also by taking in account the scheme factor p, the efficiency can be calculated. In literature there are many studies on the efficiency calculation and detectors calibration [11-13]. The obtained efficiency curve [8] is presented in Fig. 5 for checking the experimental method.

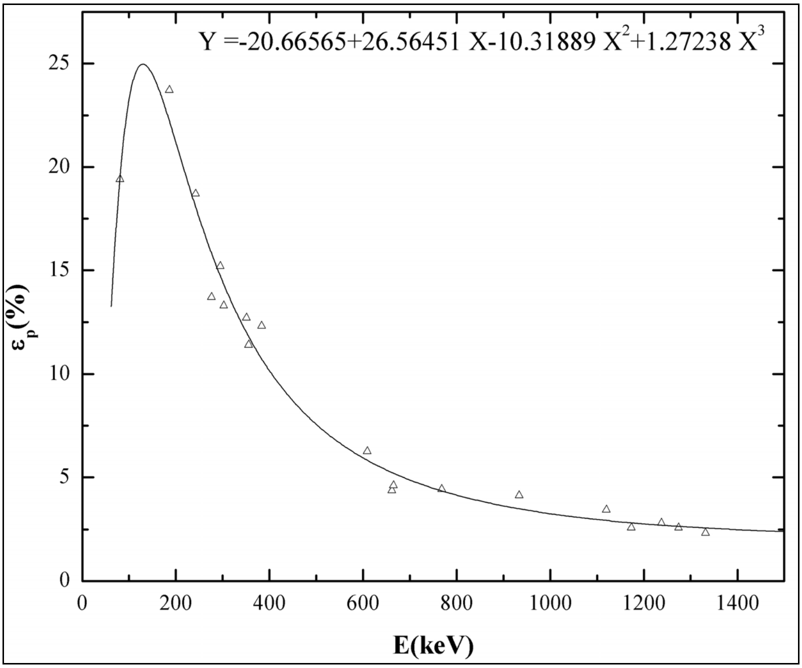

Fig. 5. Photopeak efficiency curve for the HPGe Coaxial Germanium Detector

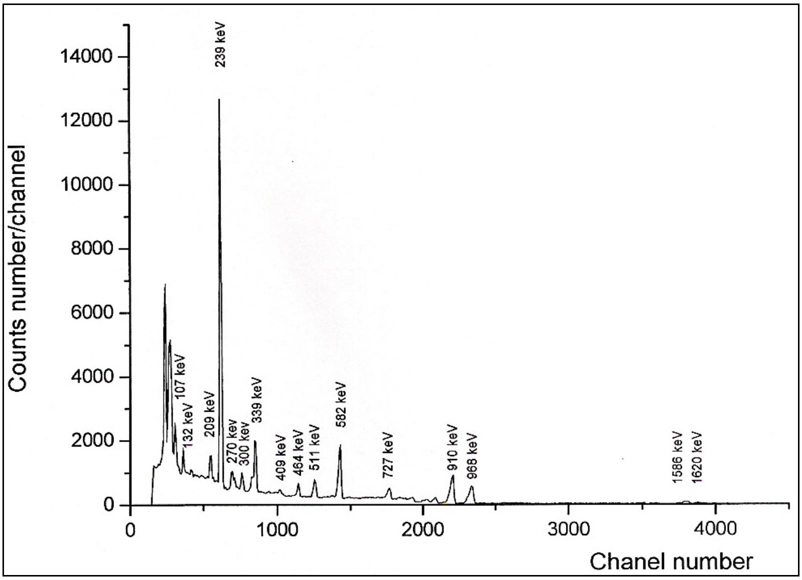

Fig. 6. Characteristic gamma spectrum of ThO_2 of 0.305 g in a 2π geometry

Due to the fact that we used foils of Cu and Au with a size of 13 x 17 mm and not point sources, in order to determine the cross-section of the reaction ^{63}Cu(n,γ)^{64}Cu, the efficiency must be reconsidered and was determined in the region of interest, with the help of calibration sources of the same size as the samples. Therefore, we prepared according to the published data from [14-18] a standard source type foil of the same size, made from ThO_2 older than 30 years, in equilibrium with its descendants, which can be used to calibrate the detector in efficiency. From literature [17], the absolute activity of ThO_2 in equilibrium with its daughter nuclei, is well known of 3872 Bq/g of ThO_2. The calibration in energy was performed over the analyzer channels and then the spectrum of this source was aquired (Fig.6) in different geometries and then the efficiency was determined only in the interest point.

A value of this efficiency of 11.5 % was obtained on the peak of 411 keV for ^{198}Au and 8.9% on the peak of 511 keV for ^{64}Cu.

3. RESULTS AND DISCUSSIONS

The thermal neutron cross section of the ^{63}Cu(n,γ)^{64}Cu reaction was determined relative to the value of the ^{197}Au(n,γ)^{198}Au reaction with a cross-section value of $\sigma_{0,Au} = 97.8 \pm 0.1$ *b* [1].

It was calculated by using equation (2):

$$\sigma_{0,Cu} = \frac{(R_s - F_{Cd} \cdot R_{s,Cd})_{Cu}}{\left(R_s - F_{Cd} \cdot R_{s,Cd}\right)_{Au}} \cdot \frac{g_{Au}}{g_{Cu}} \cdot \frac{G_{th,Au}}{G_{th,Cu}} \cdot \frac{F_{g,Cu}}{F_{g,Au}} \cdot \sigma_{0,Au} \qquad (2)$$

where R_s and $R_{s,Cd}$ are the reaction rates per target atom of the foil and respectively the cadmium covered isotope, F_{Cd} is the cadmium transmission factor, which arise from the fact that the specific epithermal reaction rate of a foil isotope is different from the specific epithermal reaction rate of the cadmium covered isotope, g_{Au} and g_{Cu} are the Westcott factors that describe the deviation of the cross-section from the 1/v – law. For Au $g_{Au} = 1.0004$ (20^{0}C) [10] and for Cu $g_{Cu} = 1.003$ (20 ^{0}C) [10]. The neutron self-shielding effects must be taken into account and are described by the $G_{th,Au}$ and $G_{th,Cu}$ correction factors [8]. $F_{g,Au}$ and $F_{g,Cu}$ are the gamma-ray attenuation factors and describe the attenuation of the gamma rays in the volume of the samples and $\sigma_{0,Au}$ represents the thermal neutron cross-section of the ^{197}Au(n,γ)^{198}Au reaction. The characteristics of the samples and irradiation parameters of monitor is done in Table 1 and Table 2.

Table. 1. Characteristics of the samples

Irradiated foils	Target isotope	Mass [g]	Sample surface [mm^2]	Thickness [mm]
Cu-foils	^{63}Cu	0.566	221	0.3
Au-foils	^{197}Au	1.283	221	0.32

Table. 2. Characteristics and parameters of the monitor irradiated foils

Reaction	Foil mass [g]	Foil thickness [mm]	σ_0 [a][b]	I_0 [a][b]	$\overline{E}_r$ [b] [eV]	G_e	E_{Cd} [eV]	R
^{197}Au(n,γ)^{198}Au	1.285	0.32	9.87E+01	1.57E+03	5.47	0.263	0.55	10.376

[a] taken from [10]; [b] taken from [19]

Irradiations were performed at saturation in a sandwich structure, at a constant neutrons flux for 10 days. After irradiation, the samples were measured by high resolution gamma spectrometry (Fig.7 and 8) and the activity decreasing curve for Cu was determined in order to calculate the half-life. A half-life of 12.7 h for ^{64}Cu was determined, due to the fact that another Cu isotope β^+ is present ^{66}Cu with a half-life of 6 min.

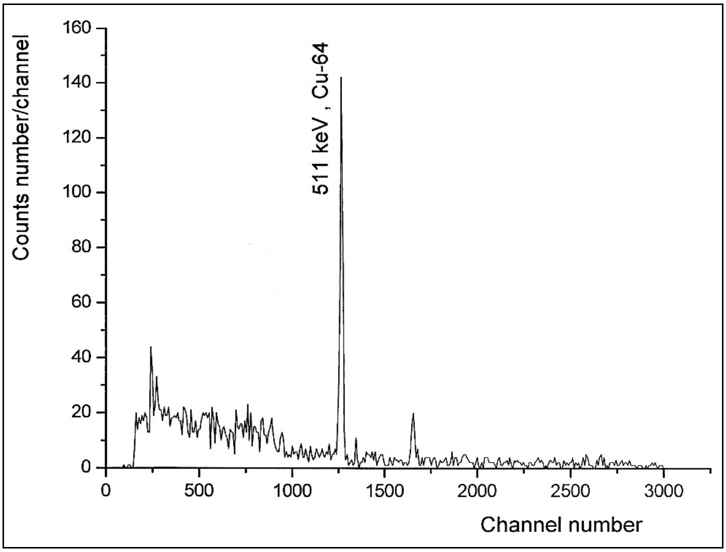

Fig. 7. Characteristic gamma spectrum of a foil of Cu irradiated at saturation in the block with isotopic neutron sources

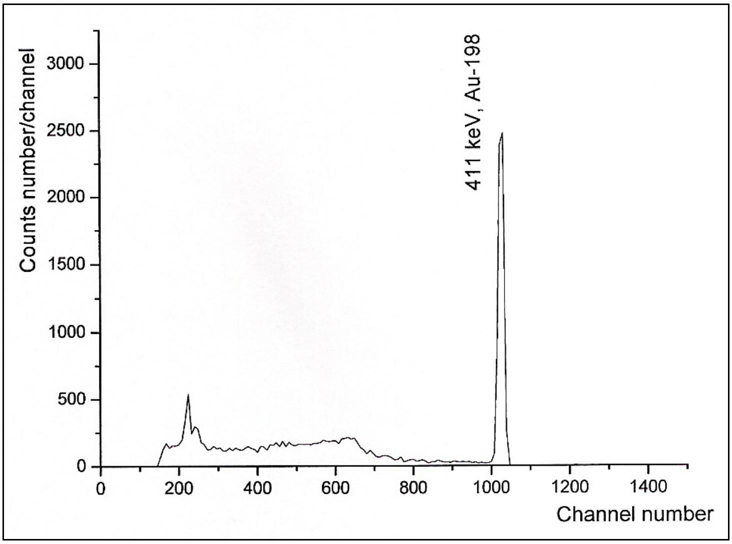

Fig. 8. Characteristic gamma spectrum of a monitor foil of Au activated at saturation

After the determination of the factors from formula (2), the thermal neutron cross section for the $^{63}Cu(n,\gamma)^{64}Cu$ nuclear reaction was determined relative to the value of the thermal neutron cross-section of the monitor reaction of Au ($\sigma_{0,Au} = 98.7 \pm 0.1$ *b*) and a mean value of $\boldsymbol{\sigma_{Cu} = 3.2 \pm 0.8}$ ***b*** was obtained for the range between: 0.025 eV- 0.55 eV. From calculation we concluded that at a neutron flux of $\Phi = 10^{12}$ n/s·cm^2 in a nuclear reactor, the specific activity to produce ^{64}Cu by thermal neutrons is about Λ/m= 790 mCi/g.

4. CONCLUSIONS

In this paper were studied nuclear resonance reactions involving neutrons, producing the ^{64}Cu and ^{198}Au radioisotopes by using isotopic neutron sources. We also studied the activation method, the cut-off cadmium method and the cadmium ratio method in order to measure the thermal neutron cross-section for a particular (n,γ) reaction for the $^{63}Cu(n,\gamma)^{64}Cu$ nuclear reaction by preparing samples cadmium covered foils, which were irradiated in the neutron flux produced by 2 isotopic neutron sources of ^{241}Am-^{9}Be and ^{239}Pu-^{9}Be, all the correction factors were calculated in the case of foil samples and a mean value of $\sigma_{Cu} = 3.2 \pm 0.8$ *b* for the thermal neutron cross-section was obtained. This value is in good agreement with other data published in literature [10]. In conclusion, in the case there is no cyclotron available in order to produce ^{64}Cu to be used for P.E.T. in local clinics, the method by irradiation with thermal neutrons at a nuclear reactor can be a good choice.

REFERENCES

[1] Laura Daraban, K. Abbas, F. Simonelli, N. Gibson, *Applied Radiation and Isotopes*, 66, 261(2008)

[2] Laura Daraban, R. Adam Rebeles, A. Hermanne, *Applied Radiation and Isotopes*, 67, 506 (2009)

[3] S.F. Mughabghab et al., Neutron Cross Section from Neutron Resonance Parameters and Thermal Cross Sections, Academic Press, New York (1981)

[4] L. Daraban, R. Adam Rebeles, *Studia UBB Physica*, L, nr.1, 49 (2005)

[5] Laura Daraban, O. Cozar, Li. Daraban, *Studia UBB Physica*, 51, 2, 61(2006)

[6] L. Daraban, Laura Daraban, O. Cozar, R. Adam Rebeles, The 5th International Conference on Isotopes, 25-29 Appril, Bruxelles, Belgium, International Proceedings, 257 (2005)

[7] H.K. Beckurts, K. Wirtz, Neutron Physics, pp. 277-282, Springer-Verlag, Berlin (1964)

[8] S.P. Gosuly, L. Daraban, *Studia UBB Physica*, LV, nr.2, 41 (2010)

[9] M. Karadag, H. Yucel, M. Tan, A. Ozmen, *Nucl. Instr. Meth A* 501, 524 (2003)

[10] National Nuclear Data Center, BNL, http://www.nndc.bnl.gov/

[11] C.A. Adesanmi, F.A. Balogun, M.K. Fasasi, I.A. Tubosun, A.A. Oladipo, *J. Radioanal. and Nucl. Chem.*, 249, No. 3, 607 (2001)

[12] Mahmoud I. Abbas, *Appl. Radiation and Isotopes* 64, 1661 (2006)

[13] D. Arnolda, O. Sima, *Applied Radiation and Isotopes* 61, 117 (2004)

[14] Z.B. Alfassi, F. Groppi, *Nucl. Instr. Meth. A*, 574, 280 (2007)

[15] N. Lavi, Z.B. Alfassib, N. Drndarski, *Nucl.Instr.Meth.Phys.Res.A* 385, 376 (1997)

[16] N. Lavi, Z.B. Alfassi, *Appl. Radiat.Isotopes* 61, 1437 (2004)

[17] N. Lavi, Z.B. Alfassi, *Radiation Measurements*, 39, 15 (2005)

[18] J. Saegusaa, K. Kawasakia, A. Miharaa, M. Itob, M. Yoshida, *Appl. Radiation and Isotopes* 61, 1383 (2004)

[19] F. De Corte, L. Moens, K. Sordo-El Hammami, A. Simonits, J. Hoste, *J. Radioanal. Chem*. 52, (2), 305 (1979)

STUDIA UBB PHYSICA, Vol. 57(LVII), 2, 2012, pp. 13-18
(RECOMMENDED CITATION)

LANE-CHANGING WITH DECISION IN A TWO-LANE SPRING-BLOCK TRAFFIC MODEL

F. JÁRAI-SZABÓ[a]

ABSTRACT. A decision-based advancing strategy is proposed and analyzed in the framework of the one-directional two-lane spring-block traffic model. A fraction *q* of cars is allowed to change lanes, while the others will keep their initial lane. One single car in the row is acting with decision-based strategy. Its lane-changing attempt is decided based on the behavior of other cars in the row. As a function of the parameter *q* the winning probability and the average gain in the advancement for this car is computed. It is concluded, that this decision-based strategy used only by one car in the row is advantageous in any conditions for the driver.

Keywords: *highway traffic modeling; spring-block models; advancing strategies; competition.*

INTRODUCTION

Road traffic is a non-linear complex phenomenon that produces various forms of collective behavior. This is the reason why it is intensively studied since the last few decades [1-6]. Moreover, a jammed traffic system is a good example of a complex system formed by many competing agents. Accordingly, in case of stop-and-go traffic jams on a multi-lane road it is crucial for a driver to use the best lane-changing strategy. The selection of these strategies is not so straightforward. However, a good driver simply “feels” what strategy to use for a better advance.

Very recently, using the spring-block model of the two-lane highway traffic [7] two simple advancing strategies have been analyzed. Based on the results of this previous study, in the present work a new decision based advancing strategy is proposed and analyzed in the framework of the spring-block model. First, the two-lane spring-block traffic model is shortly described. Then, the decision-based lane-changing strategy is presented and analyzed in detail. Finally, conclusions are drawn based on our large-scale computer simulation results.

---

[a] Babeş-Bolyai University, Faculty of Physics, 1 Kogălniceanu Str., 400084 Cluj-Napoca, Romania, ferenc.jarai@phys.ubbcluj.ro

SPRING-BLOCK MODEL OF THE TWO-LANE HIGHWAY TRAFFIC

The used model belongs to the spring-block model family, which has many interdisciplinary applications and it proved to be efficient in explaining complex dynamics or structure formation by collective behavior [8-13].

The spring-block model of the single-lane highway traffic was described in detail in our previous works [14,15]. Blocks are modeling cars in a lane. Furthermore, springs that acts unidirectional from the car ahead to the car in the back, model distance keeping interaction of cars. With these simple elements a spring-block chain is built. Then, the first block is dragged with constant velocity v_0, inducing the movement of the whole chain. Besides these basic elements, there is the friction that acts on each block and opposing it's free sliding. In analogy with classical mechanics the movement of blocks is opposed by static or kinetic friction force (F_S or F_K). The ratio $f = F_K / F_S$ is kept constant. These friction forces are generated randomly from a normal distribution with mean value $<F_S>$ and standard deviation σ for each new position of each car. This introduces a characteristic disorder in the system, with a major influence on the observed collective dynamics. The friction itself models differences, imperfections and unpredictable reactions of the drivers, while the difference between F_S and F_K models the so-called slow-to-start rule [16]. Accordingly, in this approach, one has to deal with three free parameters f, $<F_S>$, σ. They effects on the model behavior have been analyzed recently [15].

The dynamics of the spring-block chain is simulated following the typical steps of a simplified molecular dynamics simulation. Technical details and algorithm tests are specifically described in our previous works [14,15].

The single-lane spring-block model described above has been recently extended to handle unidirectional two-lane traffic conditions [7]. For this reason two identical spring-block chains and simple lane-changing rules have been considered. In defining the lane-changing rules we had in mind that usually, a driver will try to change lanes when there is a car in his/her front that is advancing slower than he/she. Accordingly, a block is selected for lane changing, if the distance to the previous block in the row is smaller than the average distance between cars measured at single-lane conditions. Also, in order to be eligible for lane changing, the velocity of the car has to be greater or equal to the velocity of the car ahead. The cars eligible for lane changing will execute the maneuver only if there is enough space next to them on the other lane for entering safely. Moreover, we impose that the distance to the next car in the other lane has to be large enough in order to ensure an advance of the newly entered car in the next simulation step.

The behavior of the resulted model system has been studied in the congested traffic regime defined by fixed model parameter values $<F_S> = 9.6$, $\sigma = 2.6$ and $f = 0.8$. The efficiency of two driving strategies, one with lane-changing maneuvers allowed and another with lane-changing maneuvers disabled, have been compared.

From our computer simulation results [7] one may learn that the best or winning strategy is the one adopted by the less number of cars. However, this was a first approach for a quite complex phenomenon, and in reality the problem proves to be more complicated. Drivers are not stuck to one of these strategies, and their driving style continuously changes.

DECISION BASED LANE-CHANGING STRATEGY

Based on conclusions of the previous study [7], a decision based lane-changing strategy (DBS) is proposed. We assume, that a smart driver can make a decision based on the "statistics" of a few number n of cars that are advancing in his/her front in both lanes. If more than a half of the detected cars is acting with lane-changing strategy (LCS) then, the smart driver will advance keeping his/her initial lane. In contrast, if more than a half of cars is keeping their lanes (LKS) then, the smart driver will act with lane-changing strategy.

In order to test the efficiency of the DBS strategy two lanes of N = 1000 cars are considered. As in case of previous study [7] the parameter values are fixed in the congested traffic regime $<F_S> = 9.6$, $\sigma = 2.6$ and $f = 0.8$. The last car of the first row is set to follow this DBS strategy while the last car of the other lane is set to advance respecting the LKS strategy. At the beginning of each simulation the advancing strategy of the other cars in the queue is set to LCS with probability q and to LKS with probability $1-q$. After initializing the system, the first car of both rows is dragged in a parallel manner through a distance of $D = 5000$ simulation units. At the end of each simulation the distance d between the selected cars is measured and their positions are compared. The car that is closer to the beginning of the row is declared as winner. The simulations are repeated and from a statistics of *1000* simulations the winning probability w of DBS strategy is determined.

RESULTS

In Figure 1 these winning probabilities are presented as a function of the fraction q of cars following LCS strategy. Different curves on the figure represent results for DBS strategies where the decision is made on a basis of n cars. The results may be compared to the winning probabilities of LCS strategy, as well. On one hand, for $q < 0.5$ the winning probabilities are exactly one for both DBS and LCS strategies. This may be explained taking into account that in this regime the DBS is working mostly without lane changing. On the other hand, for $q > 0.5$ there is a big difference in the winning probabilities. It is immediately observable that the winning probability of DBS is increased relative to the LCS and it fluctuates around *0.5*. This means that the strategy in this regime becomes equivalent to LKS strategy. Accordingly, the DBS strategy proved to be as good as the LCS strategy when the rest of cars mostly act with LKS strategy. The same strategy however, proved to be similar to the LKS strategy when the rest of the cars act mostly with LCS strategy. The same trend is visible in case of all values *n* in the Figure 1.

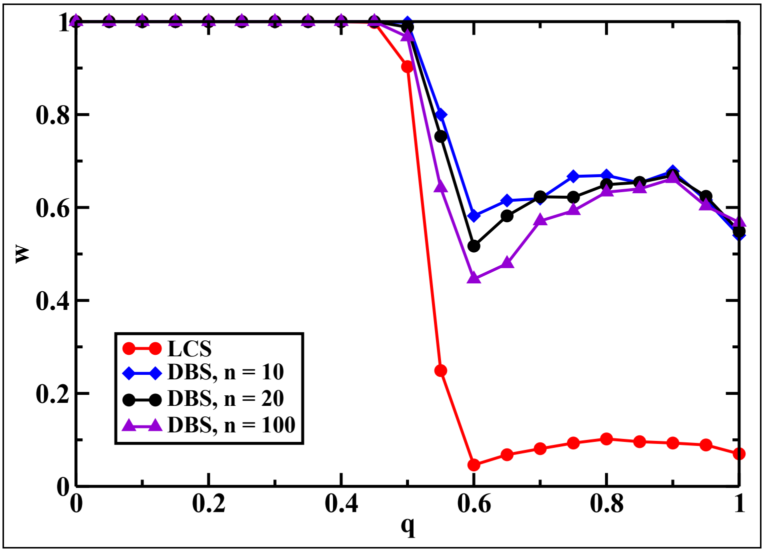

Fig. 1. Winning probabilities of DBS strategy plotted as a function of the fraction q of cars acting with LCS strategy. Different curves shows DBS strategies with decision made on a basis of n cars. As reference, winning probabilities of the LCS strategy [7] are plotted, as well.

In addition, the results above may be confirmed by using another characteristic measure, namely the average winning distance <*d*> of the DBS strategy. In order to get a value independent on the dragging distance *D*, the distances are scaled relative to this value. The results are plotted in the Figure 2, and they shows again that in case of q < 0.5 the DBS strategy has same winning distances as the LCS strategy. In contrast, for q > 0.5 in agreement with the winning probabilities around *w = 0.5* the DBS winning distances are fluctuating around 0. This confirms again that in this regime the DBS strategy is equivalent to the LKS strategy.

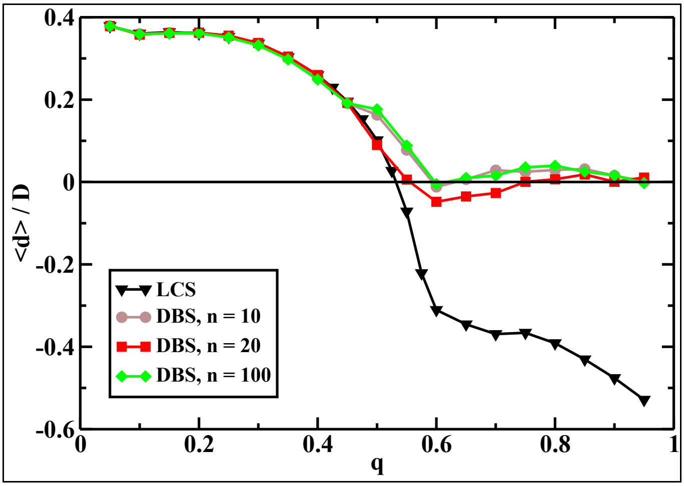

Fig. 2. Average scaled winning distance *<d>/ D* as a function of the fraction q of cars acting with LCS strategy. Different curves shows DBS strategies with decision made on a basis of n cars. As reference, average scaled winning distances of the LCS strategy [7] are plotted, as well.

CONCLUSIONS

In conclusion, a spring-block type two-lane traffic model has been used to study the efficiency of a proposed decision based driving strategy in case of congested traffic conditions. Based on the presented simulation results we can conclude that regardless of the driving conditions the decision-based strategy used only by a single car in the queue keeps the advantage of both lane-changing and lane-keeping strategies. It has to be noted, that by using significantly more computational power, the present model can be made more complex assuming many cars acting with DBA strategy or decision to be made on a basis of the actual efficiency of the current strategy. However, this is beyond the scope of the present work.

The main conclusion of our recent study [7] it was that the winning strategy is the one adopted by the less number of cars. This is confirmed here again because in all of our simulations, independently to the other drivers' option, the best strategy proved to be the DBA strategy, which has been used only by a single car in the row.

ACKNOWLEDGMENTS

This work was supported by CNCSIS-UEFISCSU, project number PN II-RU PD404/2010.

REFERENCES

1. T. Nagatani, *Rep. Prog. Phys.*, 65, 1331 (2002).
2. B.S. Kerner, The physics of traffic, Springer, Berlin, NewYork (2004).
3. D. Chowdhury, L. Santen, A. Schadschneider, *Physics Reports*, 329,199 (2000).
4. D. Helbing, *Rev. Mod. Phys.*, 73, 1067 (2001).
5. S. Maerivoet and B. de Moor, *Physics Reports*, 419, 1 (2005).
6. S. Darbha, K.R. Rajagopal and V. Tyagi, *Nonlinear Analysis*, 69, 950 (2008).
7. F. Jarai-Szabo and Z. Neda, *Int. J. Mod. Phys. C,* 23, 1250063 (2012).
8. G. Mate, Z. Neda, J. Benedek, PLOS One 6 (8), e16518/1-8 (2011).
9. K.T. Leung and Z. Néda, *Phys. Rev. Lett.*, 85, 662 (2000).
10. K.T. Leung, L. Jozsa, M. Ravasz and Z. Néda, *Nature,* 410, 166 (2001).
11. F. Járai-Szabó, S. Astilean and Z. Néda, *Chem. Phys. Lett.*, 408, 241 (2005).
12. F. Járai-Szabó, E.Á. Horvát, R. Vajtai, Z. Néda, *Chem. Phys. Lett.*, 511, 378 (2011).
13. K. Kovács and Z. Néda, *Physics Letters A*, 361, 18 (2007).
14. F. Járai-Szabó, B. Sándor, Z. Néda, *Cent. Eur. J. Phys.*, 9(4), 1002 (2011).
15. F. Járai-Szabó, Z. Néda, *Physica A*, 391, 5727 (2012).
16. R. Barlovic, L. Santen, A. Schadschneider, M. Schreckenberg*, Eur. Phys. J. B.,* 5 (3), 793–800 (1998).

STUDIA UBB PHYSICA, Vol. 57(LVII), 2, 2012, pp. 19-29
(RECOMMENDED CITATION)

THE OSCILLATION MODES INDUCED BY SPECIAL DRIVERS IN SOLAR CORONAL LOOPS

N. MAGYAR[a], A. PARDI[a], S. ONTANU-CRACIUN[a], A. MARCU[a,*]

ABSTRACT. In this paper we perform a numerical study of transversal oscillations in coronal loops represented as a straight thin flux tube, which are generated under the effect of an external force, the global coronal EIT wave.

Given the equation that describes the transversal oscillations in coronal loops, we consider several forms for the driver (e.g. wave train, interaction points separated by a delay time, non-harmonic), and then solve it numerically. We discuss the dependence between the induced oscillation modes and the nature of the driver and its parameters.

Keywords: *magnetohydrodynamics (MHD) simulations, EIT waves, coronal loops*

INTRODUCTION

EIT waves are one of the major discoveries of the Extreme ultraviolet Imaging Telescope of SOHO. However, their nature continues to be debated. Explanations for the signatures include: fast mode shock [1], fast mode waves [2][3], solitons [4]. We are interested in the interaction of these waves with coronal loops. Observational evidence for these interactions has been provided by satellites (SOHO, TRACE/EUV, STEREO/EUVI). Due to these uncertainties, and to the wide range of possible explanations, we need to consider and discuss separately the cases of drivers of different nature.

The present paper is mainly based on the analytical study from Ballai et al (2008)[5]. The main purpose is to extend this study for drivers that are not described in the article mentioned before (soliton, wavetrain), by the means of numerical analysis. We also discuss the dependence between the induced oscillation modes and the loop length. A comparison between analytical and numerical results is also presented.

---

[a] Babes-Bolyai University, Faculty of Physics, 1 Kogalniceanu str., 400084 Cluj-Napoca, Romania
* Corresponding author: alexandru.marcu@phys.ubbcluj.ro

The paper is organized as follows: The mathematical model used is described in Sect. 2, the numerical results are presented and discussed in Sect 3, and finally, in Sect. 4 we summarize our results and discuss some possible extensions.

MATHEMATICAL MODELS

We model the interaction between the external force and the coronal loop considering some assumptions: the coronal loop can be approximated with a straight thin flux tube with fixed footpoints, embedded in a magnetic-free environment under the effect of gravity.

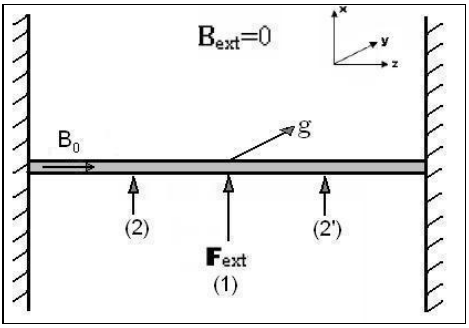

Fig. 1. Schematic representation of the model. Depending on the driver, the external force will act at one point (1) or at two symmetrically placed points (2) – (2')

We assume that the EIT wave is acting with a force ***F*** on the tube and the direction of this force is parallel with the *x*-axis. The EIT wave is modeled as a pulse in position, in one or more points. A schematic representation of the model is shown in **Fig. 1**.

The equation that describes the transversal oscillations in the tube can be derived from the linearised ideal MHD equations. It is not our goal, however, to obtain this equation.

We will adopt the equation derived in [5]

$$\frac{\partial^2 \xi}{\partial t^2} = -\frac{\rho_i - \rho_e}{\rho_i + \rho_e} g \frac{\partial \xi}{\partial z} + \frac{\rho_i v_A^2}{\rho_i + \rho_e} \frac{\partial^2 \xi}{\partial z^2} + \frac{F}{\rho_i + \rho_e} \qquad (1)$$

here ρ_i, ρ_e are the internal, respectively external density, g is the gravitational acceleration, $v_A^2 = \frac{B^2}{\mu \rho_i}$ is the internal Alfvén speed, ξ *(z,t)* is the horizontal displacement of the tube. Equation (1) describes the propagation of transversal oscillations of a vertical flux tube, in the presence of an external force, ***F***.

Instead of using this equation, we introduce a new function Q, defined as $\xi = Qe^{\lambda z}$ We can choose the value of λ such that the coefficient of the first derivative with respect to z in eq. (1) vanish.

We obtain
$$\lambda = g\frac{\rho_i - \rho_e}{2\rho_i v_A^2} \tag{2}$$

Then, using some new notations, Eq. (1) becomes

$$\frac{\partial^2 Q}{\partial t^2} - c_K^2\frac{\partial^2 Q}{\partial z^2} + \omega_c^2 Q = \mathcal{F} \tag{3}$$

where $\mathcal{F} = Fe^{-\lambda z}/(\rho_i+\rho_e)$

The waves will propagate with the speed given by the second term on the left hand side:

$$c_K = \sqrt{\frac{\rho_i}{\rho_i + \rho_e}} \tag{4}$$

which is the *kink speed.*

The cut-off frequency for kink modes propagating in coronal loops appears here as the coefficient of the third term:

$$\omega_c = \frac{g}{2v_A}\sqrt{\frac{(\rho_i - \rho_e)^2}{(\rho_i + \rho_e)\rho_i}} \tag{5}$$

For typical coronal parameters
$(g = 274 \text{ ms}^{-2}, v_A = 900 \text{ kms}^{-1}, \rho_i/\rho_e = 10)$, ω_c is about 0.13

NUMERICAL RESULTS

The simulations were performed with PDE2D code [6]. The numerical code utilizes the Galerkin finite element method with piecewise polynomial basis funtions in space and the second-order Crank-Nicolson method in time. Equation (3) is solved numerically on the 1D interval (0,L). This interval consists of 100 cells. The numerical results are not affected by insufficient spatial resolution, statement based on grid refinement studies (we performed simulations with 50 and 100 grids, and there is no qualitative difference between the results). We apply fixed boundary conditions at the endpoints, so $Q|_{x=0}$, $Q|_{x=L}$ and $\frac{\partial Q}{\partial t}|_{x=0}$, $\frac{\partial Q}{\partial t}|_{x=L}$ are all zero. Thus, the tube has fixed footpoints. This appears to be a reasonable constraint because the motions in the solar corona does not affect the high density photosphere. The tube is motionless at t=0, which means that the initial conditions are supplied by: $Q|_{t=0} = 0$ and $\frac{\partial Q}{\partial t}|_{t=0} = 0$.

Drivers of particular form

As EIT waves was explained in the context of wavelike or pulse-like behaviour, we need to consider harmonic and non-harmonic drivers of various forms. Also, it is difficult to estimate the direction and magnitude of this force or the way it interacts with the coronal loop.

We begin with the harmonic drivers. The simplest case is when the driver interacts in only one point with the tube, and its amplitude remains constant. We can model this case by giving F the form:

$$\mathcal{F} = E_{EIT}\lambda_e \frac{\delta(z-z_0)e^{-\lambda z}e^{i\omega_{EIT}t}}{\rho_i+\rho_e} \tag{6}$$

where $\delta(z)$ is the Dirac-delta function and ω_{EIT} is the frequency of EIT waves.

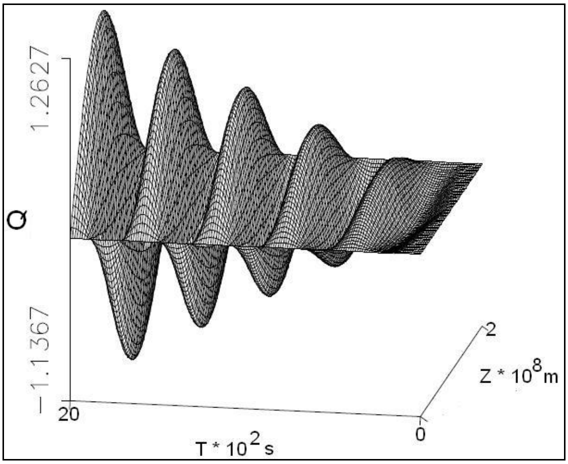

Fig 2. 3D plot of the amplitude of the oscillation(arbitrary units) for tube length L = 200 Mm; $T_{EIT} = \frac{2\pi}{\omega_{EIT}}$ = 400 s. The tube (represented here from Z = 0 to Z = 2* 10^8) initially is motionless (T = 0s), and the system evolves until T =2*10^3s. The only mode excited is the fundamental mode.

The periods of oscillations are in very good agreement with the analytically calculated periods in [5]. We present here (**Fig. 2**) a special case, when the generated loop oscillation is in resonance with the external driver. As we considered the ideal MHD equations, there are no damping mechanism, so this resonance will eventually lead to an infinite growth in amplitude. The total simulation time (t_f = 2000 s) is set such that there is a compromise between the number of oscillations that fit in this time (around 6-7) and the simulation running time. Also, the number of complete oscillations observed for a single loop is usually no more than 5-7.

The next driver we implemented is the same as the first, harmonic driver, but acting at 2 symetrically placed points from the apex. This choice seems to be a good one if the EIT wave is an oscillating front colliding with the coronal loop. We must discuss about the existence of a delay time between these interactions. In reality it is more likely that the front of the EIT wave is not absolutely perpendicular to the axis of the loop, so there will be a time required for the other end of the wavefront to reach the loop. In this case, the acting force will have a spatial and temporal dependence of the form

$$\delta(z-z_0)e^{iw_{EIT}t}+\ \delta(z-L+z_0)e^{iw_{EIT}(t-T_d)}H(t-T_d) \tag{7}$$

here T_d is the delay time and $H(t)$ is the Heaviside step function.

First we consider the simplest case, when there is no delay time (T_d = 0 s), i.e. the EIT wave hits the loop perpendicularly. In **Fig. 3** we compared the resulting oscillations of single-point excitation and double-point excitation for a special case, when $T_{EIT} = \frac{2\pi}{\omega_{EIT}}$ = 200 s. With the help of figure 3 from [5], we know that the modes generated (for double-point excitation) are the fundamental mode (400 s) and the second harmonic (133 s), but no first harmonic can be generated. On the other hand, with single point excitation, only the first harmonic mode can be generated. In this case there is a resonance between the driver and the coronal loop. We can clearly see in **Fig. 3** that for double-point interaction the fundamental mode and the second harmonic (appearing as the "shoulder" of the fundamental mode) are generated. As the period of the second harmonic mode is three times smaller than the period of fundamental mode, this "shoulder" (in reality the outer peaks of the second harmonic) appears with every period of the fundamental mode, so they are in phase. The oscillation pattern from single-point excitation contains only the first harmonic (right image of **Fig. 3**).

These results and observations are in perfect accordance with the analytically deduced oscillation patterns.

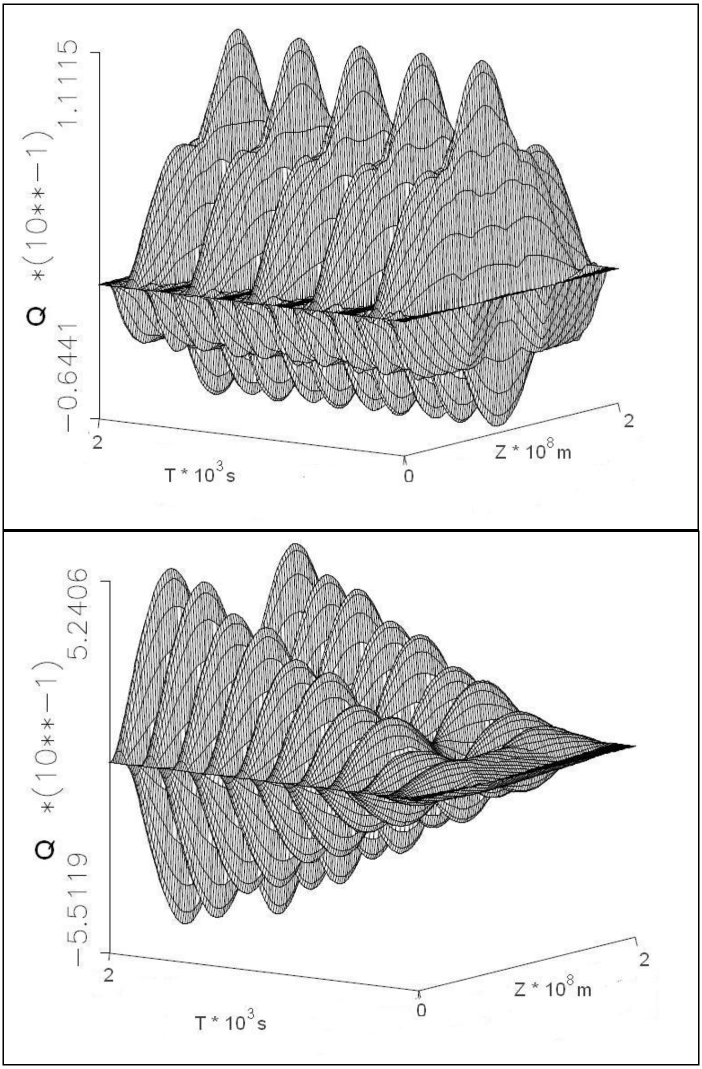

Fig. 3. 3D plot of the amplitude of the oscillation(arbitrary units) for double-point interaction (left image), and single-point (right image). The period of the driving force is the same for both cases (T_{EIT}=200s).

However, to make one step closer to reality, as we mentioned before, there will be a time required for the second interaction to reach the loop. In this case, considering the delay time T_d= 1.5T_{EIT}, the resulting graph of the system evolution is nearly similar in shape with the right image of **Fig. 3**. Other interesting discussion is on the amplitude of the oscillations as a function of the delay time (see **Fig. 4**).

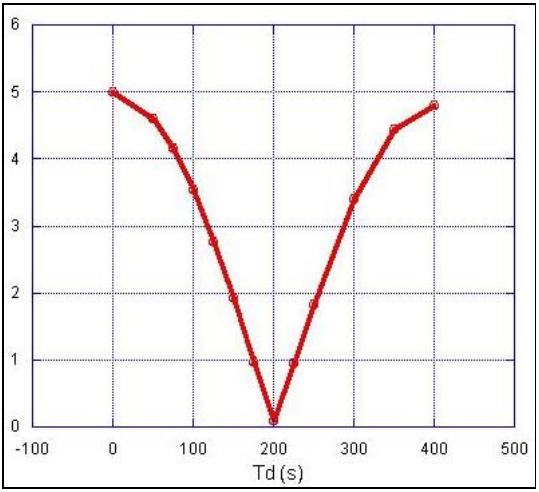

Fig. 4. Amplitude of the fundamental mode as a function of delay time (ranging from 0 to T_{EIT}= 400 s)

Until now we considered the EIT "wave" a static phenomenon, with constant amplitude. Further on, our study focus on drivers with a pulse-like behavior. [4] speculated that the EIT waves might be best explained as a soliton-like phenomenon, say, a slow-mode solitary wave. However, there is no modeling of such an idea. So, we consider a basic model, with the envelope described by the *sech = cosh*$^{-1}$ function, and a carrier wave with period T_{EIT}. At the first approximation, this is a wave-packet. The temporal dependence of the driver will have the form

$$e^{iw_{EIT}t}\ sech^2(a(b-t)) \tag{8}$$

where *a* ,*b* are two constants that define the temporal width and maximum of the solitary wave. We chose the width of the pulse to be 10 times T_{EIT}. In **Fig. 5** is showed a comparison between single and double-point excitation in the form for the driver.

The oscillation modes generated are the same as in **Fig. 4**. That is not surprising because for both cases we used the same conditions and period for the EIT wave. So, there are no differences in the generated modes if the wave is modulated or not, at least in this particular case. The main difference between the graphs of **Fig. 5** is the amplitude of the remanent oscillation, i.e. the oscillation sustained after the loop was excited. We can see that, for double-point excitation, the induced modes are very weakly self-sustained after the interaction ceased, with only about 2% of the maximum amplitude. Practically, the amplitude of the oscillations varies with the amplitude of the driving force.

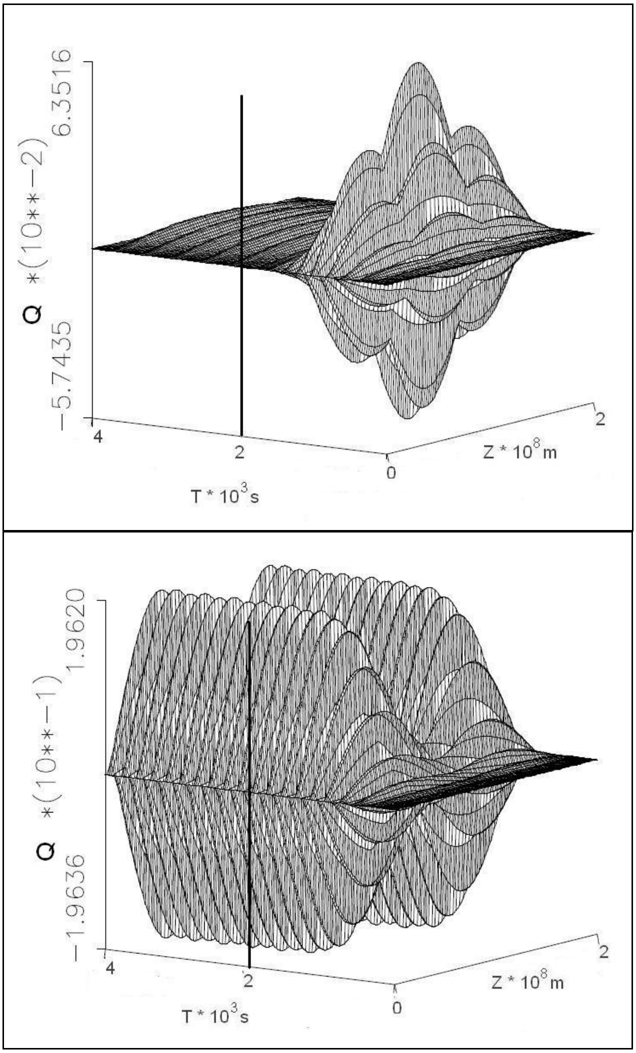

Fig. 5. 3D plot of the amplitude of the oscillation (arbitrary units) for double-point interaction (left image), and single-point (right image).
The period of the driving force is the same for both cases (T_{EIT}=200s).
The black line at t = 2 * 10^3 s represents the point at which the solitary wave has entirely left the coronal loop, i.e. the driving force is practically zero.

In the second case (**Fig. 5**, right image), the oscillation amplitude grows gradually, and the oscillation is self-sustained with no loss in amplitude after the interaction ceased. This is a consequence of resonance.

A more general case would be a “train” of such wave-packets, i.e. wave packets coming one after another, periodically. Considering this “period” between two wave-packets to be 10 T_{EIT}, the evolution of the system is presented in **Fig 6**. In this case, for the system in resonance (right image), we can see how the contributions from each wave packet add up, resulting in a smoothed staircase grow in amplitude. For not self-sustaining case (left image), the amplitude of oscillations follows the period of wave-packets, with no adding up in time.

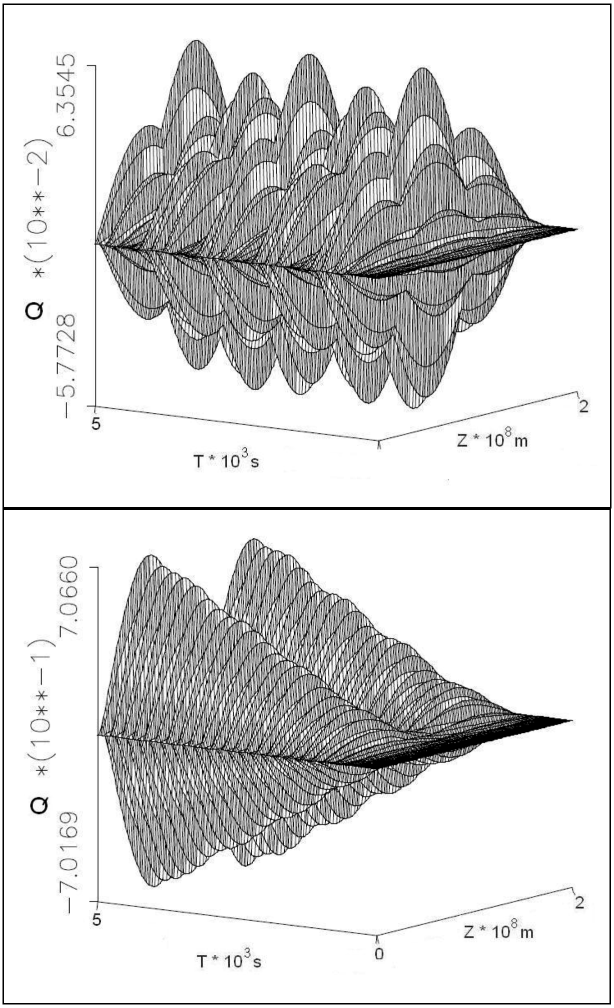

Fig 6. 3D plot of the amplitude of the oscillation f(arbitrary units) for double-point interaction (left image), and single-point (right image).
The period of the driving force is the same for both cases (T_{EIT}=200s).

Finally, we consider a non-harmonic driver: a pulse of finite amplitude of the form

$$\mathcal{F} = E_{EIT}\lambda_e \frac{e^{-\lambda z}\left[H(z-z_0)-H(z-z_0')\right]}{\rho_i+\rho_e}\,\delta(t) \tag{9}$$

Which means that the external driving force is represented by a finite width (z_0-z_0') front acting only at t = 0s. This form of the EIT wave will produce oscillations at the natural frequency of the loop only.

Now, we discuss about the changes induced by modifying the length of the loop. The natural frequency of the loop varies with length. Using the property that a non-harmonic driver will produce oscillations only at the natural (fundamental) frequency of the loop, we perform numerical simulations for different loop lengths to see what is the period of the induced natural mode.

The considered loop lengths were: 200Mm (used previously in our study), 150 Mm and 100 Mm, and the associated natural frequencies of the fundamental mode, in this order, were: 400s, 300s, 200s. Consequently, for a loop of 100 Mm length, for example, a single-point excitation with driver of the form eq.(6), T_{EIT} = 200 s, will produce the same oscillation like in **Fig 2**, of course, with smaller amplitude. From our results, we see that in resonance mode (400s, 300s, 200s), the amplitudes at $t = 2 * 10^3\ s$ decreases proportional with the loop length, in the same ratio: 2 : 1.5 : 1.

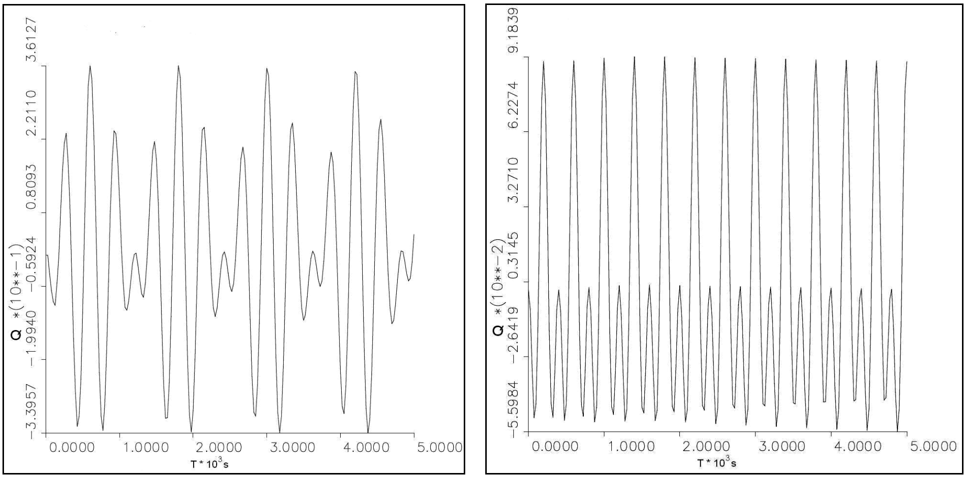

Fig 7. The displacement of the apex as a functon of time, for a loop length of 150 Mm (left image), 100 Mm (right image). The driver used is listed as eq.(7), with no delay time between the interactions. The period of the driving force is the same for both cases (T_{EIT}=400s).

In **Fig.7** we compared the oscillations of the apex for the same driving period for different loop lengths. For 200 Mm the graph is not shown, the reader can see this case in **Fig. 2**. For shorter lengths, there is a superposition of two modes: the natural mode and the “forced” mode with the same frequency of the driver. This case appears for larger periods than 400 s in **Fig. 3** of [5].

CONCLUSIONS

The oscillations generated in coronal loops by interactions with EIT-waves is studied.

Given the equation describing the motion of the loop, an inhomogeneous Klein-Gordon-type equation, we solve it numerically considering different types of external forces. We can conclude that our results are in good agreement with the analytical results of [5]. The main objective of this study was to consider other forms for the acting EIT-wave, since there exists various explanations for its nature. We found that resonance modes are self-sustaining (see e.g. **Fig 5**, right image), i.e. the oscillations are maintained even after the interaction with the EIT-wave ceased.

Of course, in reality, the remaining oscillations would damp rapidly. For the case when the driver is composed of an envelope and a carrier wave, there is no strong dependence of the resulting oscillations on the form of the envelope of the harmonic driver. The frequency of the driver has the most important role in the resulting oscillations of the loop.

REFERENCES

1. Y. Uchida, *Solar Physics*, 4, 30-44, 1968.
2. Y-M. Wang, *ApJ,* 543, 89, 2000.
3. S.T. Wu; Zheng, Huinan; Wang, S.; Thompson, B.J.; Plunkett, S.P.; Zhao, X.P.; Dryer, M., *Journal of Geophysical Research*, 106, A11, 25089-25102.
4. Wills-Davey, M.J.; DeForest, C.E.; Stenflo, J.O., *ApJ*, 664, 556, 2007.
5. I. Ballai, M. Douglas, A. Marcu, *A&A*, 488, 1125, 2008.
6. G. Sewell, The Numerical Solution of Ordinary and Partial Differential Equations, 2005.

STUDIA UBB PHYSICA, Vol. 57(LVII), 2, 2012, pp. 31-39
(RECOMMENDED CITATION)

PHOSPHORUS EFFECT ON THE TEXTURAL PROPERTIES OF SOL-GEL Si_2O-CaO-P_2O_5 BIOACTIVE GLASS SYSTEM

K. MAGYARI[a], L. BAIA[a,*], O. POPESCU[b,c], S. SIMON[a], V. SIMON[a]

ABSTRACT. This study is focused on the structural, morphological and textural characterization of the (64-x)SiO_2·(36-x)CaO·2xP_2O_5 bioactive glass system, where x=0, 1, 2 and 4 mol%. The obtained sol-gel samples were characterized using X-ray diffraction (XRD), Fourier transform infrared spectroscopy (FTIR), particle size distribution analysis and N_2-sorption measurements. XRD patterns of the samples with phosphorus content show the presence of the tricalcium phosphate phase. It was found that by P_2O_5 addition, the mesopores diameter decreases below 10 nm and the pores become interconnected.

Keywords: *bioactive glasses, sol-gel, structure, morphology*

INTRODUCTION

The bioactive glasses constitute an important group of bioactive materials that have found wide application in medicine as bone implants [1-3].These materials have specific response *in vivo* at the interface with biological media. They are able to bind with a strong chemical bond with bone in a living organism through the formation of carbonate apatite like layer on the implant site [3]. Glasses based on SiO_2-CaO-P_2O_5 compositions can bond to both soft and hard tissue without an intervening fibrous layer [2].

Roughness, porosity, pore size distribution and particle size of biomaterials play a critical role in protein adsorption [4]. The protein molecules bond to the biomaterial surfaces through different ways, such as electrostatic force, hydrophobicity

---

[a] Babes-Bolyai University, Faculty of Physics & Interdisciplinary Research Institute on Bio-Nano-Sciences, 400084 Cluj-Napoca, Romania
*Corresponding author: lucian.baia@phys.ubbcluj.ro
[b] Babes-Bolyai University, Molecular Biology Center of Interdisciplinary Research Institute on Bio-Nano-Sciences, 400271 Cluj-Napoca, Romania
[c] Romanian Academy, Institute of Biology, 060031 Bucharest, Romania

and so on [4-7]. It is generally accepted that on the higher surface area the quantity of protein adsorbed is higher [4]. Thus, modeling the roughness, porosity, pore size and particle size of biomaterials it can create more surface area.

Based on the fact that the higher SiO_2 amount the higher surface area and taking into consideration that glasses with SiO_2 content between 58-65 mol% have cylindrical pore open at both ends with occasional necks along the pore [1, 8], one of our goals has been to analyze the influence of P_2O_5 content on surface texture.

The aim of this study was to determine the effects of P_2O_5 on sol-gel SiO_2-CaO-P_2O_5 bioactive glass system texture. Therefore, the SiO_2/CaO ratio was approximately constant; P_2O_5 was introduced on the expense of both SiO_2 and CaO.

EXPERIMENTAL

Formation of System

The system compositions $(64\text{-}x)SiO_2 \cdot (36\text{-}x)CaO \cdot 2xP_2O_5 \cdot$with x=0, 1, 2 and 4mol% were prepared by sol-gel method. The sol-gel precursors were tetraethyl orthosilicate (TEOS) and calcium nitrate tetrahydrate ($Ca(NO_3) \cdot 4H_2O$), hydrolyzed in presence of nitric acid, the (HNO_3+H_2O)/(TEOS+TEP) molar ratio being constant and equal to 8. Reactants were added consecutively after 1-h intervals, with continuous stirring. The solution (*sol*) was poured into closed containers which were kept at room temperature until gelation (*gel*) was reached (2-3 days depending on the sol composition). The resultant gel was aged at room temperature and by thermal treatment at 70^0C for 72 h and atmospheric dried in an oven at 120^0C for 48 h. Nitrate elimination and material stabilization was carried out at 700^0C/3h. This temperature was determined by differential thermal analysis of the dried gels.

Methods

The X-ray diffraction analysis was carried out on a Shimadzu XRD-6000 diffractometer using CuKα radiation (λ=1.5418 Å), with Ni-filter. The diffractograms were recorded after the samples were annealed at 700°C.

FT-IR spectra were recorded in reflection configuration in the range of 4000-650 cm^{-1} with the resolution 4 cm^{-1} using a Jasco IRT-5000 FT-IR microscope coupled to a Jasco FT-IR-6000 spectrometer. The recorded spectra were smoothed by 5-point Savitzky-Golay smoothing function.

The particle size distribution of the bioactive samples was determined on a Shimadzu Nano Particle Size Distribution Analyzer SALD-7101 using a laser diffraction method with a UV semiconductor laser (375 nm wavelength).

The specific surface area, pore volume and pore radius of the samples were obtained from N_2-adsorption-desorption isotherms, using a Sorptomatic 1990 apparatus. The specific surface area was obtained by the Brunauer–Emmett–Teller (BET) method, while the pore volume and pore size distribution were determined by the Barret–Joyner–Halenda (BJH) method.

RESULTS AND DISCUSSION

SiO_2-CaO-P_2O_5 system is one of the most studied systems in the field of bioactive sol-gel glasses. The diffraction patterns of the prepared samples are shown in Figure 1. It can be seen that the bioactive system powders exhibit mainly amorphous characteristics (Fig. 1a) corresponding to glass, but the weak and broad signal centered at $2\Theta=32°$ indicates the presence of a crystalline structure that can be associated with the crystallization of tricalcium phosphate phase, identified as $Ca_3(PO_4)_2 \cdot H_2O$ [9, 10].This is more pronounced in the sample with x=2.

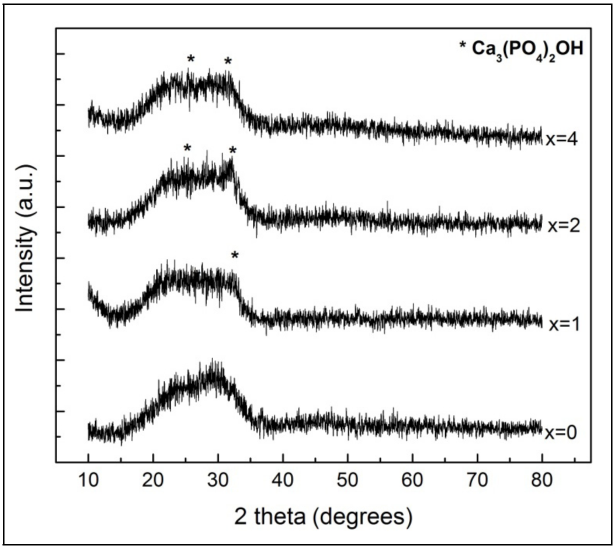

Fig. 1. XRD patterns of heat treated sol-gel derived samples belonging to the system (64-x)SiO_2·(36-x)CaO·2xP_2O_5

The FTIR spectra show the typical absorption bands of the bioactive glasses (Fig. 2). In these spectra were identified two transverse optical mode of the Si-O-Si groups: the bending Si-O vibration identified around 800 cm^{-1}, and the antisymmetric stretching mode Si-O located in the range 1000-1300 cm^{-1} composed of an intense adsorption band centered around 1070 cm^{-1} and a shoulder around 1220 cm^{-1} [5, 11].

The band at 940 cm^{-1} can be assigned to SiO non-bridging oxygens (NBO) formed because of the presence of network-modifier cations, in particular Ca [2]. The spectra exhibit an absorption band located in the range 465-475 cm^{-1} attributed to Si-O-Si bending vibration [12].

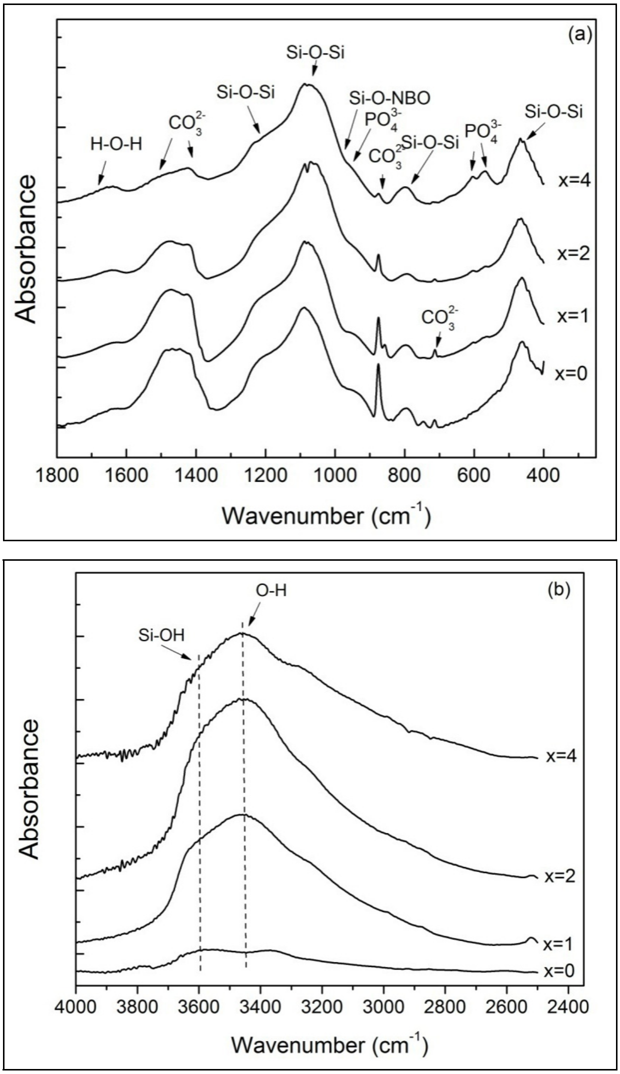

Fig. 2. FT-IR spectra of the (64-x)SiO_2·(36-x)CaO·2xP_2O_5·samples for different spectral ranges as follows: 1800-400 cm^{-1} (a) and 4000-2500 cm^{-1} (b)

The presence of phosphate groups in the samples with P_2O_5 content is shown in the infrared spectra by double band located around 604 and 565 cm^{-1} [13]. This doublet is usually attributed to the PO_4^{3-} bending vibrations in a crystal-like environment [12, 14, 15], but in the results reported by Aguiar et al. [13] these doublet corresponds to P-O-NOB vibrations and its signature is associated with the presence of the Ca content. They demonstrated that these bands are not visible in the spectra of CaO-free glasses [13]. These FTIR doublet increases in intensity with increasing the amount of P_2O_5.The band around 565 cm^{-1} is not visible for the sample with 2 mol% P_2O_5, but the band around 470 cm^{-1} is broadening (Fig. 2a). The presence of the CO_3^{2-}groups in the bending and stretching mode is detected at 712, 875 and 1420 cm^{-1} [14, 17]. These bands decrease with the increasing of the amount of P_2O_5. The presence of molecular water is indicated by the band around 1640 cm^{-1}, which can be associated with a deformation mode of adsorbed molecular water in the sample [2, 5, 13]. This is confirmed by the presence of a broad band around 3450 cm^{-1}, attributed to O-H stretching vibration [17, 18].

To determine the effects of changing the SiO_2/P_2O_5 amounts in the bioactive glass system, in the next step particle size distribution of heat treated samples was measured. The particle size of milled and ultrasonicated samples ranged from 0.012 µm to 0.034 µm (Fig. 3). Particle size distributions for all samples obtained are similar.

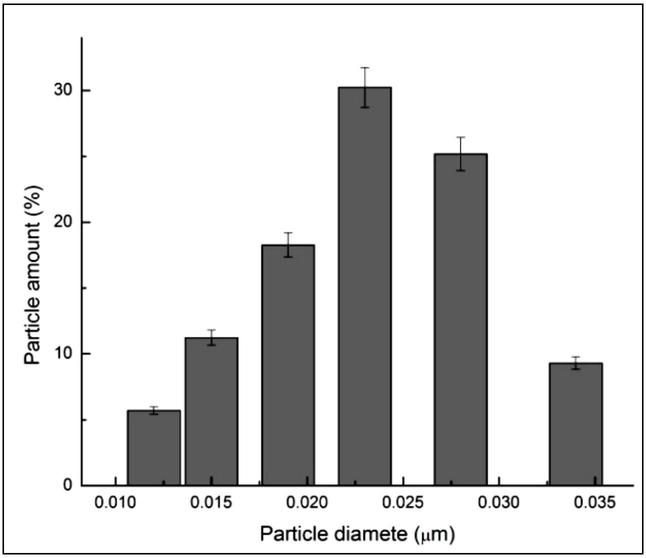

Fig. 3. Particle size distribution ofSiO_2-CaO-P_2O_5·investigated samples

The textural analysis was performed using BET and BJH methods by determining specific surface area, pore volume and pore size distribution, respectively. In Figure 4a one can see that the addition of phosphorus in the sample results in increased surface area. The difference between specific surface areas recorded for the investigated samples which contain phosphorus is negligible. The total pore volume of bioactive glass samples ranged between 0.16-0.24 cm^3/g. This value was higher for the sample x=2 (Fig. 4b).

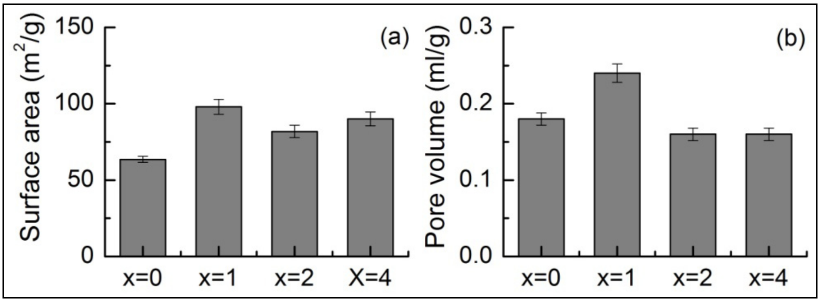

Fig. 4. The BET surfaces area (a) and pore volumes (b) of the $(64-x)SiO_2\cdot(36-x)CaO\cdot 2xP_2O_5\cdot$samples

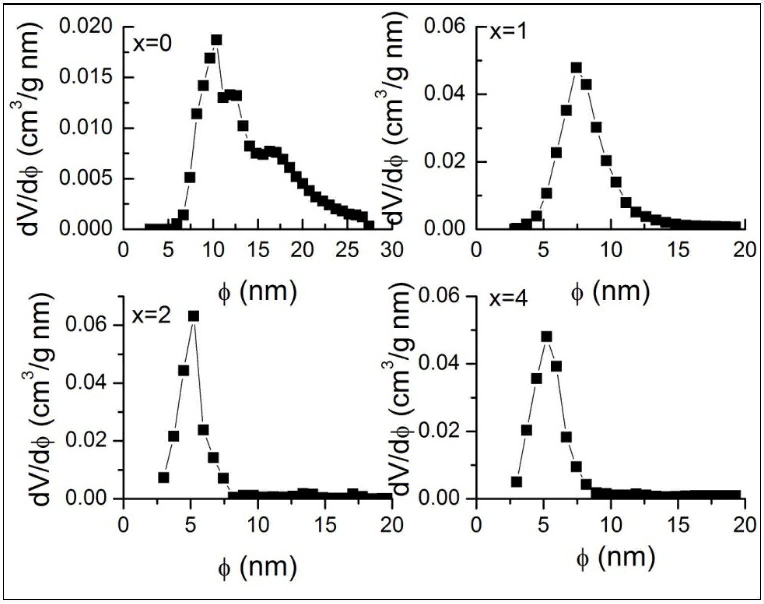

Fig. 5. Pore size distribution of the $(64-x)SiO_2\cdot(36-x)CaO\cdot 2xP_2O_5\cdot$bioactive glass system obtained by BJH method from the nitrogen adsorption isotherms

According to the IUPAC classification the textural pore size was therefore in the mesopores range with diameters between 2-50 nm [19]. With the addition of phosphorus in the system composition one observes a decrease of the pore diameters (Fig. 5), reaching values below 10 nm for the samples with x = 2 and x=4.

The hysteresis loops in the IUPAC classification reflect a widely accepted correlation between the shape of the hysteresis loop and the morphology of the mesoporous adsorbent [20]. The samples with x=0, 1, 2 exhibit type H1 hysteresis loops, and the sample with x=4 type H2 hysteresis loops (Fig. 6). Types H1 and H2 hysteresis loops, typical for mesoporous silica, correspond to cylindrical pores open at both ends and of disordered/interconnected porous material, respectively [20, 21]. Thus, one can conclude that with increasing phosphorous content the pores are more intensely interconnected.

Based on the IUPAC classification the isotherms obtained from the sample without P_2O_5 are of type V and those from the samples with P_2O_5 are of type IV (Fig. 8) [19]. When the material is mesoporous the types IV and V occur for strong and weak fluid-wall forces, respectively [22].

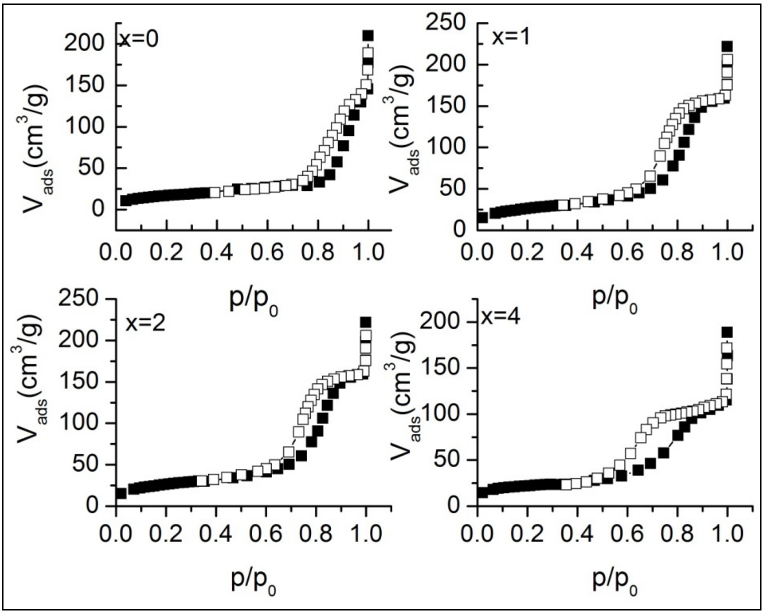

Fig. 6. The adsorption-desorption isotherms of nitrogen on the (64-x)SiO_2·(36-x)CaO·2xP_2O_5·bioactive systems

CONCLUSIONS

Bioactive glass samples of (64-x)SiO_2·(36-x)CaO·2xP_2O_5 system($0 \le x \le 4$ mol%) obtained by sol-gel method present beside the amorphous structure a weak crystalline phase, corresponding to tricalcium phosphate phase, as $x \neq 0$. FTIR spectra evidence the absorption bands typical for bioactive glasses. The results show that specific surface area increases with the addition of phosphorus, and higher surface area is expected to lead to higher porosity in the samples with phosphorous. Taking into account that the total pore volume is high only in the sample with x=1 and the pore diameters decrease to value below 10 nm in samples with x=2 and x=4, it could be considered that the porosity of bioactive systems can increase by adding the phosphorous, but the pore size decreases with increasing the amount of phosphorus. The samples with x = 0, 1 and 2 have the cylindrical pores open at both ends. The results obtained for the sample with x= 4 show that with increasing phosphorus content in the system the pores are interconnected.

Based on the fact that ensuring spatially uniform cell distribution, cell survival, proliferation and migration *in vitro* interconnected pores request, we consider that the optimal bioactive glass composition is $60SiO_2 \cdot 32CaO \cdot 8P_2O_5$.

ACKNOWLEDGMENTS

This work was possible with the financial support of the Sectoral Operational Program for Human Resources Development 2007-2013, co-financed by the European Social Fund, within the project POSDRU 89/1.5/S/60189 with the title „Postdoctoral Programs for Sustainable Development in a Knowledge Based Society”.

REFERENCES

1. M. Vallet-Regi, C.V. Ragel, A.J. Salinas, *Eur. J. Inorg. Chem*, 6 1029 (2003).
2. A. Balamurugan, G. Sockalingum, J. Michel, J. Fauré, V. Banchet, L. Wortham, S. Bouthors, D. Laurent-Maquin, G. Balossier, *Mater. Lett,* 60, 3752 (2006).
3. D. Arcos, M. Vallet-Regi, *Acta Biomater,* 6, 2874, (2010).
4. K. Wang, C. Zhou, Y. Hong, X. Zhang, *Interface Focus,* 2, 259 (2012).
5. K. Magyari, L. Baia, O. Popescu, S. Simon, V. Simon, *Vib Spec,* 62, 172 (2012).
6. O. Yang, Y. Zhang, M. Liu, M. Ye, Y.Q. Zhang, S. Yao, *Anal. Chim. Acta,* 597, 58 (2007).
7. K. Magyari, O. Popescu, V. Simon, *J. Mater. Sci: Mater. Med.*, 21, 1913 (2010).

8. M. Vallet-Regi, A.J. Salina, D. Arcos, *J. Mater Sci: Mater Med,* 17, 1011 (2006).

9. S. Padilla, J. Roman, S. Sanchez-Salcedo, M. Vallet-Regı, *Acta Biomater,* 2, 331 (2006).

10. A. Vulpoi, L. Baia, S. Simon, V. Simon, *Mater Sc iEng C,* 32, 178 (2012).

11. J. Serra, P. Gonzalez, S. Liste, C. Serra, S. Chiussi, B. Leon, M. Perez-Amor, H.O. Ylanen, M. Hupa, *J Non-Cryst. Solids,* 332, 20 (2003).

12. D. Cacaina, H. Ylanen, S. Simon, M. Hupa, *J. Mater Sci: Mater Med,* 19, 1225 (2008).

13. H. Aguiar, J. Serra, P Gonzalez, *Int. J. Appl. Ceram. Technol*., 8 (3), 511 (2011).

14. H. Aguiar, J. Serra, P. Gonzalez, B. Leon, *J Non-Cryst. Solids,* 355, 475 (2009).

15. T.W. Chuang, M.H. Chen, F.H. Lin, *J Biomed Mater Res A,* 85(3), 722 (2008).

16. F. Bosch Reig, J V GimenoAdelantando, MCM Moya Moreno, *Talanta*, 58, 811 (2002).

17. P.B. Sarawade, J.-K. Kim, H.-K. Kim, H.-T. Kim, *Appl. Surf. Sci.,* 254, 574 (2007).

18. H.S. Mansur, R.L. Orefice, W.L. Vasconcelos, Z.P. Lobato, L.J.C. Machado, *J. Mater. Sci. Mater. Med*., 16, 333 (2005).

19. K.S.W. Sing, D.H. Everett, R.A.W. Haul, L. Moscou, R.A. Pierotti, J. Rouquerol, *Pure Appl. Chem*., 57, 603 (1985).

20. A.Grosman, C. Ortega, *Langmuir,* 21, 10515 (2005).

21. J. R. Jones, L. M. Ehrenfried, L.L. Hench, *Biomaterials*, 27, 964 (2006).

22. P. B. Balbuenat, K. E. Gubbins *Langmuir,* 9, 1801 (*1993)* 1801.

STUDIA UBB PHYSICA, Vol. 57(LVII), 2, 2012, pp. 41-47
(RECOMMENDED CITATION)

ELECTRICAL RESISTIVITY AND EXCESS OF CONDUCTIVITY IN BULK (Bi-Pb)2223 SUPERCONDUCTORS

A.V. POP[a], G. STIUFIUC[a], V. POP[b] AND C. LUNG[a,*]

ABSTRACT. Superconducting samples $(Bi_{1.6}Pb_{0.4})(Sr_{1.8}Ba_{0.2})Ca_2Cu_3O_y$ and $(Bi_{1.6}Pb_{0.4})Sr_2Ca_2Cu_3O_y$(Bi-2223) have been obtained by solid state reaction method and characterized by electrical resistivity and X-Ray diffraction measurements. The effect of sintering temperature on the electrical resistivity and excess conductivity were investigated. The parameters obtained from temperature dependence of resistivity data in the normal state and superconducting transition are sensitive to the sintering temperature. The fluctuation induced conductivity analysis of the samples were performed in the light of Aslamasov–Larkin (AL) theory.The composition and sintering temperature dependence of crossover reduced temperature between 2D and 3D regimes in excess conductivity have been analysed.

Keywords: ceramic (Bi,Pb):2223 superconductor, XRD, electrical resistivity, excess conductivity.

INTRODUCTION

The Bi:2223 superconducting phase has attracted much attention due to its higher T_c and the potential for applications. Bi-based superconductors have a relatively high T_c and some advantages of easy formability high chemical stability. The values for the critical transition temperature, T_c, and critical current density, J_c, are sensitive to the hole concentration and the oxygen content in the sample [1-4]. The bulk (Bi,Pb):2223 material consists of grains weakly coupled at the grain boundaries by junctions or weak links.

Since the oxide superconductors have a very short Ginzburg–Landau coherence length, $\xi_{GL}(0)$, it is therefore essential to look into the fluctuation induced conductivity analysis of excess conductivity $\Delta\sigma(T)$ at temperatures well above the critical

---

[a] Faculty of Physics, University Babes-Bolyai, str. M. Kogalniceanu 1, 40084 Cluj-Napoca, Romania
[*] Corresponding author: claudiu.lung@phys.ubbcluj.ro
[b] Department of Physics, Technical University, Cluj-Napoca, Romania

temperature. The fluctuation excess conductivity has been usually well interpreted in the Ginzburg-Landau (GL) formalism in terms of gaussian amplitude fluctuations of the order parameter [5]. Among the different contributions which can be at play, the Aslamazov-Larkin (AL) term either in 2D or 3D appear the most relevant in high-Tc cuprates [6-10]. Lawrence–Doniach LD model [11]. It predicts a crossover from three-dimensional 3D electronic state of the system to a two-dimensional one 2D with increasing temperature.

In this paper we report the effect of sintering temperature on the electrical resistivity, excess of conductivity and superconducting properties of (Bi,Pb):2223 bulk systems, by measurements of XRD and electrical resistivity function of temperature.

EXPERIMENTAL

Bulk samples with nominal composition $(Bi_{1.6}\,Pb_{0.4})Sr_2\,Ca_2\,Cu_3\,O_y$ (sample A1) and $(Bi_{1.6}\,Pb_{0.4})(Sr_{1.8}\,Ba_{0.2})\,Ca_2\,Cu_3\,O_y$ (samples T1 and T2) were obtained by the conventional solid-state reaction of appropriate amounts of the metal oxides and carbonates of 99.99% purity. The partial substitution of Sr by Ba was used to induce the reduction of the modulation period [12].Appropriate amounts of Bi_2O_3, PbO, $SrCO_3$, Ca CO_3, La_2O_3 and CuO were mixed in agate mortar and calcined at 800 ^{0}C for 36 hours. The calcinated powder was pressed into pellets and presintered at 840 ^{0}C for 200 hours. The pellets were grinding, pressed and resintered as following: the first (named sample A1)for 60 hours at 845 ^{0}C, the second (named sample T1) for 60 hours at 845 ^{0}C, and the last sample (named T2) for 60 hours at 850 ^{0}C.

The X-ray diffraction (XRD) analysis confirmed the majority of peaks belong to the “2223” phase with a few of peaks belonging to the “2212” phase in S samples.

The four probe method was used for electrical resistance measurements. We used conductive silver paste with which golden leads were attached to the specimens.

RESULTS AND DISCUSSIONS

The temperature dependencies of electrical resistance, ρ (T), for the samples A1, T1 and T2 are shown in Fig. 1. Above the excess conductivity region, in the 190K-300K temperature range, all samples show a linear temperature dependence of the electrical resistivity:

$$\rho_L = \rho_0 + a*T \qquad [1]$$

where ρ_0 is the residual resistivity and a is the slope of resistivity in the normal state.

As shown in Table 1, the ρ_0 and a values changes function of sample composition (A1 and T1) and function of sintering temperature (for samples T1 and T2 with the same chemical composition). The partial substitution of Sr by x=0.02Ba and the increase of sintering temperature decreases residual resistivity. The decrease of ρ_0

suggest that the number of scattering centers in the intra-and intergrain regions decrease. The granular microstructure and the nature of contacts between the grains strongly influenced the residual resistivity.

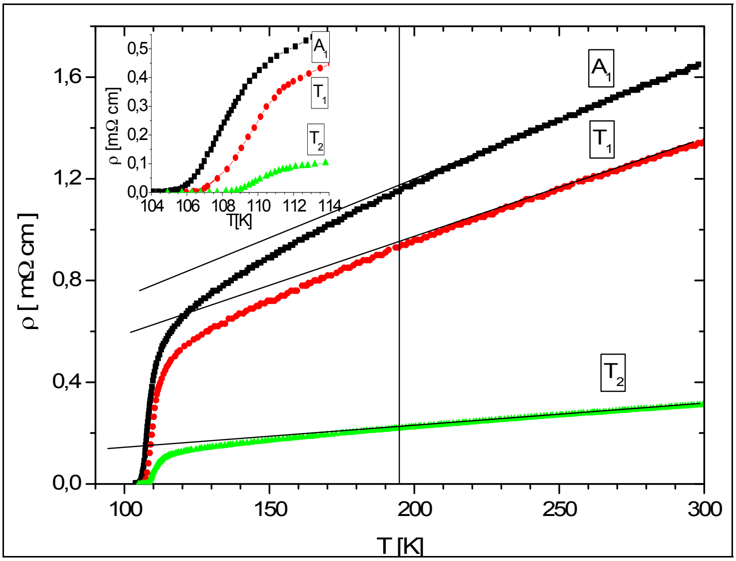

Fig. 1. The temperature dependence of the electrical resistance for samples A1,T1 and T2. The inserts show the transition region.

The measured normal resistivity in bulk samples is related to the intrinsic resistivity in CuO_2 (a-b) plane of a single crystal, by the relation [13,14]:

$$\rho = p(\rho_{ab} + \rho_{ct}). \qquad [2]$$

The coefficient p account for a mean percolative lengthening of the conduction paths and for the mean shrinking of the current cross-section, ρ_{ab} is the in plane resistivity for a single crystal and ρ_{ct} is associated with the contact resistance between the grains. The in plane resistivity for a single crystal is: $\rho_{ab} = \rho_{0i} + \alpha_i\, {}_i{*}T$, where ρ_{0i} is the intrinsic residual resistivity and $\alpha_i = d\rho_{ab}/dT$ is the intrinsic slope of linear dependence of $\rho_{ab}(T)$.The coefficient p were extracted for each sample by assuming that $\alpha_i = d\rho_{ab}/dT$ in x=0.00 single crystal is weakly affected by a small concentration of La. We obtain $p = a/\ \alpha_i$, therefore the increase of parameter p for S1 samples and the decrease for S2 samples [Table 1].

For single crystal the intrinsic value is $\alpha_i = 0.5\ \mu\Omega\ cm\ K^{-1}$ [14] The partial substitution of Sr by x=0.02Ba and the increase of sintering temperature lead to the decrease of geometric factor for percolation p, and of intergrain contact resistivity. $\rho_{ct.}$

Table 1. The resistivity parameters in studied samples.

Sample	T_c [K]	$T_c(\rho=0)$ [K]	$\rho(0)$ [$\mu\Omega$.cm]	$a=d\rho/dT$ [$\mu\Omega$.cm/K]	p	$\rho_{ct.}$ [$\mu\Omega$.cm]
A1	108	105	228	4.65	6.2	37
T1	109	106.5	196	3.88	5.17	38
T2	109.5	108	50	1.27	1.7	29

Anothers parameters sensitive to partial Sr substitution with Ba and sintering temperature are the midpoint critical transition temperature (T_c), the transition width and the temperature for zero resistivity ($T_c(\rho=0)$). [see Table 1]. $T_c(\rho=0)$ change may be in relation by phase content and intergrain dissipation processes. Tc(0) is the temperature below which the whole sample is transferred to zero resistance state. The samples with weak intergrain coupling possess low values of Tc(0) as well as higher normal state resistivity as compared to the sample having strong intergrain connectivity.The effects of partial substittution of Sr with Ba and the increase of sintering temperature is the increase of intergrain coupling.

The analysis of results for the fluctuation contribution on electrical conductivity is performed by assuming that the conductivity excess is given by:

$$\Delta\sigma = \sigma(T) - \sigma_L(T) \tag{3}$$

where σ (T)=1/ρ(T) is the measured conductivity and σ_L (T) =1/ρ_L(T) is the term extrapolated from the high-temperature behavior (linear part of ρ_L(T)).

According to the Aslamasov-Larkin (A–L) theory, the fluctuation conductivity diverges as a power law of the type:

$$\Delta\sigma = A\varepsilon^{\lambda} \tag{4}$$

where A is the fluctuation amplitude, ε= (T-Tc)/Tc represents the reduced temperature and λ is the critical exponent.

In order to compare the experimental data with the theoretical expressions for superconducting fluctuating behaviour, we plot ln($\Delta\sigma$) versus ln(ε) of polycrystalline A1,T1 and T2 samples (figure 2)

Three Gaussian fluctuation regions were clearly identified above Tc. Critical exponent λ is -3/2 for 1D (one dimensional) fluctuations), λ= -1 for 2D (two dimensional) fluctuations and λ=-1/2 for 3D (three dimensional) fluctuations. It can be seen from Figure 2 that all the samples have shown 3D fluctuations in the lower temperature region with a cross-over to 2D fluctuations in the higher temperature region. The 2D and 3D fluctuations were also observed in our samples but the 2D–3D cross-over temperature of all the samples has been shifted to higher value for sample T1 (by partial substitution of Sr with Ba).

Lawrence and Donaich (LD) modified the AL theory and they predicted a dimensional cross-over from 2D to 3D fluctuations near Tc.

$$\Delta\sigma = A\varepsilon^{-1}(1+(2\xi_c(0)/d)^2 \tag{5}$$

The temperature at which 3D–2D cross-over takes place is given as

$$T_{LD}=T_c\ (1+(2\xi_c(0)/d)^2 \tag{6}$$

The second term in the above equation is the interlayer coupling strength J, which is related to the reduced cross-over temperature ε^* through $J = \varepsilon^*/4$. In the case of polycrystalline samples the AL theory describes fluctuations in the intergrain as well as intragrain regions; however, the LD theory is associated only with the fluctuations in the intragrain regions [15].

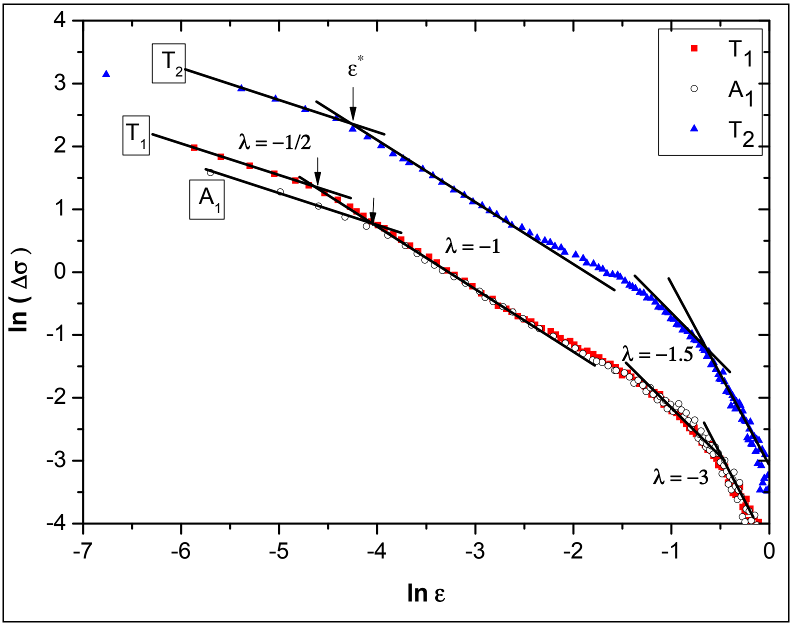

Fig. 2. Fluctuation Induced Conductivity analysis of A1, T1, and T2 samples. The solid lines are the 3D and 2D theoretical fits of experimental data following AL theory.

By using the experimental value of reduced cross-over temperature ε^* and the interlayer thickness d=15 Å the the coupling constant J and zero temperature coherence length ξ_c (0) were obtained (see Table 2). It can be seen from Table 2 that ξ_c (0) decrease after the partial substitution of Sr with Ba.

On the other hand by increasing sintering temperature the values for both parameters Tc and ξ_c (0) have been increased.

Table 2. Parameters extracted from the excess conductivity analysis of the A1,T1 and T2 samples.

Sample	T_c [K]	J	$\xi_c(0)$ [Å]
A1	108	0.0045	1.01
T1	109	0.0024	0.74
T2	109.5	0.0032	0.88

Recentely was evidenced that disorder introduced by electron irradiation increases the phase fluctuation regime above T_c, in Y123 system, and that the spatial pair extension at high T is limited by the actual density of carriers available for pairing [16]. In Bi2212 thin film, the increase of phase fluctuation by decreasing doping is related by the presence of disorder introduced by Zn ions, and the possible magnetic fluctuation in hole poor island with weak superconductivity [17]. In our Bi-2223 the excess of conductivity $\Delta\sigma$ is the same in 2D regime for A1 and T1 samples, but in 3D regime excess of conductivity increase for T1 sample (see fig. 2). This suggest that the partial substitution of Sr with Ba increases the phase fluctuation regime.

CONCLUSIONS

We synthesized the superconducting samples with nominal composition $(Bi_{1.6}\ Pb_{0.4})Sr_2\ Ca_2\ Cu_3\ O_y$ (sample A1) and $(Bi_{1.6}\ Pb_{0.4})(Sr_{1.8}\ Ba_{0.2})\ Ca_2\ Cu_3\ O_y$ (samples T1 and T2) by the standard solid state reaction method.
Above the excess conductivity region, in the 190K-300K temperature range, all samples show a linear temperature dependence of the electrical resistivity. The partial substitution of Sr by x=0.02Ba and the increase of sintering temperature lead to the decrease of geometric factor for percolation p, and of intergrain contact resistivity. $\rho_{ct.}$ Another parameters sensitive to partial Sr substitution with Ba and sintering temperature are the midpoint critical transition temperature (T_c), zero resistivity transition temperature ($T_c(\rho=0)$).

Close and above T_c, the excess conductivity analysis reveal the occurrence of two fluctuation regimes characterized by the critical exponents around $\lambda_{3D}=-0.5$ and $\lambda_{2D}=-1$ respectively. These regions were interpreted as corresponding to 3D and 2D Gaussian regimes, respectively. Another intermediated regime was identified, which is related with 1D fluctuations.

Zero temperature coherence length ξ_c (0) obtained by using LD theory (and associated only with the fluctuations in the intragrain regions) is different influenced by partial atomic substitution of Sr with Ba and sintering temperature, respectively.

REFERENCES

1. J.B. Goodenough, *Supercond. Sci. Technol.*, 3, 26, 1990.
2. J.B. Torrance, Y. Tokura, A.I. Nazzal, A. Bezinge, T.C. Huang and S.S.P. Parkin, *Phys. Rev.Lett.,* 61, 107, 1988.
3. Y. Tokura, J.B. Torrance, T.C. Huang, A.I. Nazzal, *Phys. Rev. B,* 38, 7156, 1988.
4. Y. Idemoto and K. Fueki, *Physica C,* 168, 167, 1990.
5. G. Aslamasov and A.L. Larkin, *Phys. Lett. A,* 26, 238, 1968.
6. A. Larkin and A.A. Varlamov, Theory of fluctuations in superconductors (Oxford University Press), Oxford, 2005.
7. R. Hopfengartner, B. Hensel and G. Saemann-Ischenko, *Phys. Rev. B*, 44, 741 (1991).
8. P. Mandal et al., *Physica C,* 169, 43 (1990).
9. H.M. Duan et al., *Phys. Rev. B,* 43, 12925 (1991).
10. M.R. Cimberle et al., *Phys. Rev. B*, 55, R14745 (1997).
11. L.W.E. Lawrence and S. Doniach, in *Proceedings of the 12th International Conference on Low Temperature Physics*, Kyoto, edited by E. Kanda Keigaku, Tokyo, 1971, p. 361.
12. H.K. Liu, S.X. Dou, N.Savvides, J.P. Zhou, N.X.Tan, A.J.Bourdillon and C. Sorrell, *Physica C*, 157, 93 (1988).
13. A. Marino and J.E. Rodriguez, *Physica C*, 235-240, 1425, 1994.
14. A. Diaz, A. Pomar, G. Demarco, J. Maza and F. Vidal, *J. Appl. Phys.,* 77, 765, 1995.
15. C.A.C. Passos, M.T.D. Orlando, J.L. Passamai Jr., E.V.L. de Mello, H.P.S. Correa, L.G. Martinez, *Phys. Rev. B*, 74 (2006) 094514.
16. F. Rullier-Albenque, H. Alloul and G. Rikken, arxiv 1102.2804v1 cond-mat supracon.11 Febr.2011.
17. D. Marconi,M. Pop, A.V. Pop, *Journal of Alloys and Compounds*, 513, 586-591, 2012.

STUDIA UBB PHYSICA, Vol. 57(LVII), 2, 2012, pp. 49-52
(RECOMMENDED CITATION)

LOGICAL OPERATOR REPRESENTATION OF VELOCITY ADDITION

D.A. POP[a], G.R. MOCANU[b,c,*]

ABSTRACT. This work analyses the possibility that velocity addition (both Galilean and in the framework of Special Relativity) can be *represented* with Boolean algebra.

Keywords: *logical operator, velocity composition.*

INTRODUCTION

Boolean algebra has gained an extremely wide applicability in all fields of science, be it with a representation function or actually as a built in factor in the fundamentals of the respective field. For example, logical operations in electronics are indispensable to the field. It is in electronics that logical operations are used with a very interesting purpose, namely to detect and implement limitation values. One of the most simple and elegant examples of this is the usage of logical gates [1]. Of course, in electronics these limitation values are set by humans and have a clear purpose.

Starting from this type of representation, we propose that natural phenomena with intrinsic limiting values can be **represented** by using Boolean algebra. In the next Section such a representation is described in detail for velocity composition, both in the Galilean framework and in Special Relativity. The final Section contains the Conclusions, with an emphasis on the possibility to use this type of representation to describe physical phenomena which exhibit a saturation behavior.

---

[a] "Gheorghe Sincai" High School Zalau, 15A Crisan Str., Zalau, Romania

[b] Babes Bolyai University, Faculty of Physics, 1 Kogalniceanu str., 400084, Cluj-Napoca, Romania

* Corresponding author: gabriela.mocanu@ubbcluj.ro

[c] Technical University, Faculty of Automation and Computer Science, 26-28 Baritiu Street, 400027, Cluj Napoca, Romania

VELOCITY ADDITION REPRESENTATION

If a reference system is moving with respect to a fixed observer with velocity v_1 and a body is moving with respect to the reference system with velocity v_2, velocity addition answers the question "what is the velocity of the body with respect to the fixed observer?" This question is solved in the Galilean description by the simple addition of velocities of the two systems, the reference system and the moving body [2]. For the simple one dimensional case, the mathematics is contained in the following equation

$$1.\ \vec{v} = \vec{v}_1 + \vec{v}_2$$

It is of course known that this framework is not complete. For large velocities, it becomes necessary to introduce the notion of a limiting velocity (a maximum velocity for the propagation of information), the velocity of light. With this notion, an answer consistent with what we know about fundamental physics today is obtained by applying the composition law of Special Relativity (SR). For our purposes, the mathematics of this theory is contained in

$$2.\ v = \frac{v_1 + v_2}{1 + \frac{v_1 v_2}{c^2}},$$

where c is the velocity of light.

We are not challenging any of the two frameworks, we are bringing forward a new way of representing them. For this purpose, we define a Boolean algebra. To make the addition law representable in this way, the limitative value of the velocity of light is set to mean 1, i.e. by this argument c=1. We continue with our argument by setting all other velocities (and their numerical value) to be 0 (false).

The Galilean composition of velocities can be represented in this way by the "AND" relation. The general element $x \in \{0,1\}$ obeys the following relationships [1,3]

$$3.\ x \cdot 0 = 0,$$

namely that some velocity AND a velocity that is not c, give a velocity that is not c.

$$4.\ x \cdot 1 = x,$$

namely that some velocity AND c give a velocity that is not c (this is possible in Galilean dynamics).

$$5.\ x \cdot x = x,$$

namely that some velocity AND some velocity give some velocity, and

$$6.\ x \cdot \bar{x} = 0,$$

which states that some velocity x AND its conjugate $\overline{x}$ give some velocity. If x is c, then the relation states that c AND non-c (some other velocity) gives some velocity that is non-c. If x is not c, then the relation states that some velocity AND c give some velocity which is not c (again, this type of calculation is allowed by the Galilean framework).

A concise way of seeing the ***representation*** value of this framework is to look at the Truth Table of the Galilean composition (Table 1) of velocities and of the logical AND (Table 2). The forth row which appears in the formal definition of the AND truth table is missing in the Galilean framework for the simple reason that there is no limiting entry in the case of the Galilean composition of velocity.

It is known that Nature obeys this rule of addition for small values of v. We propose that as soon as the necessity for an entry of a limiting velocity appears, Nature commutes to calculating the velocity by SR composition, i.e. the OR.

Table 1. The truth table of the Galilean composition of velocities, viewed as a Boolean operation.

velocity	velocity	Result
v	v	v
v	c	v
c	v	v

Table 2. The truth table of the logical AND.

A	B	Result
0	0	0
0	1	0
1	0	0
1	1	1

The SR composition of velocities can be represented in this way by the "OR" relation. The general element $x \in \{0,1\}$ obeys the relations [1,3]

$$7.\ x + 0 = 0\,.$$

If x is not c, this means that the addition of some velocity other than c with some other velocity other than c outputs to some velocity other than c. If x is c, then according to the table of truth of SR composition shown in Table 3 (and OR shown in Table 4) the relation becomes c+0=1.

$$8.\ x + 1 = 1\,,$$

which translates the fact that there is a built-in limitation to the velocity, the addition of some velocity with c gives c (i.e., 1) (this also works for x=c).

$$9.\ x + x = x\,,$$

which states that the addition of two velocities that are not c will give a velocity that is not c.

$$10.\ x+\overline{x}=1,$$

which states that the addition of a velocity that is not c with c is limited to c (this also works for x=c). All these issues are better understood by the comparative analysis of the table of truth for the SR composition (Table 3) and for logical OR (Table 4).

Table 3. The truth table of the SR composition of velocities, viewed as a Boolean operation.

velocity	velocity	Result
v	v	v
v	c	c
c	v	c
c	c	c

Table 4. The truth table of the logical OR.

A	B	Result
0	0	0
0	1	1
1	0	1
1	1	1

CONCLUSIONS

This article details the possibility of representing velocity addition in the real case of a limiting velocity by simple logical operations. The classical description of velocity addition is suitably done by the AND operator with no last entry for the limiting parameter. The post-classical description (Special Relativity) of the velocity addition conceptually allows for a limitation parameter. This is described by using the OR operator.

In this framework it becomes possible to represent saturation phenomena in areas of physics, biology and chemistry.

REFERENCES

[1] S.D. Anghel - Fundaments of analogic and digital electronics, Cluj, Romania, University Press, 2007 (rom.).

[2] R.P. Feynman, R.B. Leighton, M. Sands, The Feynman Lectures on Physics, Addison-Wesley Publishing Company, INC., 1964.

[3] I.R. Safarevici, Notiunile fundamentale ale algebrei, Editura Academia Republicii Socialiste Romania, Bucuresti, 1989.

STUDIA UBB PHYSICA, Vol. 57(LVII), 2, 2012, pp. 53-60
(RECOMMENDED CITATION)

SPECTROSCOPIC INVESTIGATION OF PVA MEMBRANES DOPED WITH BLACK CARBON NANOPARTICLES

T. STEFAN[a], C. LEORDEAN[a], C.V. POP[a],
D. MARCONI[a] AND M. TODICA[a,*]

ABSTRACT. The effect of black carbon particles on the spectroscopic properties of polyvinyl alcohol (PVA) was investigated by Raman and XRD methods, before and after gamma irradiation. Raman spectra of doped membranes contain the characteristic vibration bands of the PVA and of the black carbon. The X ray difractogram contains the specific peak of PVA at $2\theta = 19°$ and other peaks at $2\theta = 24°$ characteristic to black carbon. The amplitude of those peaks increases with the concentration of carbon. Possible applications of these membranes are in building fuel cell electrodes.

Keywords: *PVA; Black carbon; Gamma irradiation.*

INTRODUCTION

Polymeric membranes have multiple applications, being indispensable elements where total or controlled separation of different entities is needed. The qualities which imposed the massive use of these materials were theirs good mechanical properties, (tensile strength and flexibility), high chemical stability, as well as, the possibility to influencing some electrical, optical, chemical, or mechanical behaviors in a desired way after the introduction of additional substances into the pure polymer during the manufacturing process. A particular application of polymeric membrane is the fuel cells construction.

Polymeric materials often provide surprising solutions, both in achieving proton exchange membranes acting as solid electrolytes, as well as the electrodes [1, 2]. Improving the electric conductivity of such membranes is possible by addition of different dopants such as the black carbon. Usually the carbon nanoparticles

---

[a] ”Babes-Bolyai” University, Faculty of Physics, M. Kogalniceanu No 1, 400084 Cluj-Napoca, Romania.
* Corresponding author: mihai.todica@phys.ubbcluj.ro

induce great increase of the electronic conductivity of doped materials. On the other hands, such dopant can modify some microscopic properties of the polymeric matrix. These modifications can be observed by specific methods like XRD and Raman spectroscopy.

Other possibility to increase the electric conductivity may be the generation of free electrons along the polymeric chain by irradiation with high energy photons i.e. gamma radiation. But such aggression exerted on the polymeric matrix may induce dramatic modification on the local structure and order of polymeric chain.

The aim of this study was the observation by spectroscopic methods of possible modification induced by the addition of carbon nanoparticles and gamma exposure on the local structure of PVA membranes.

EXPERIMENTAL

Polyvinyl alcohol has the C_2H_3O monomer and it is a fine-grained, white powder. It is very soluble in water, forming a transparent gel, but insoluble in pure methanol.

A 99.9% purity carbon was used, presented in the form of fine black nanoparticles. The membranes were made by dissolving PVA powder in distilled water, adding carbon nanoparticles, vigorously stirring to homogenize, stretching on a flat surface and drying at room temperature. The polymeric concentration (PVA solution in water) was 10 % weight and the carbon dopant was added in percentages of 1, 5, 15, 30 and 50% of carbon nanoparticles with respect to PVA initial mass.

The porosity of PVA membrane increases progressively with the carbon addition and, when a 50% carbon is excelled, the binding role of PVA disappears and the membrane is falling apart. Depending on the size of the dryer support, membranes of different thicknesses can be obtained – in this case, the required thicknesses are larger than 1 mm in order to obtain a considerable absorbent amount for reactants.

The obtained membranes were subjected to spectroscopic investigations, to observe the effect of carbon on their behavior compared with the situation when they are made of pure PVA. Spectroscopic measurements aimed with Raman and X-ray diffraction investigations. Investigations were also conducted for gamma irradiated membranes with a cumulative dose of approximately 8000 Gy.

The gamma exposure was realized using a ^{60}Co source with the dose rate of 5.6 Gy per hour. The Raman investigation were performed with R 3000 CN systems, with excitation power 150 mW at wavelength λ = 785 nm. The X-ray diffraction (XRD) was performed with a Brucker X-ray difractometer with Cr K_α 228 nm at 45 KV and 40 mA. The 2 teta range of 10-90 was recorded.

RESULTS AND DISCUSSION

Generally the polymeric materials are very stable chemical compounds with very low chemical reactivity after polymerization. For this reason the addition of supplementary chemical elements, like the black carbon for ours systems, leads to the formation of dispersion of the dopant into the polymeric matrix, without the apparition of new chemical bonds. However the presence of the dopant in the vicinity of the polymeric segments can induces small modification of the vibration modes of some chemical bonds of the monomer. Such changes can be observed by comparing the Raman spectra of pure polymeric matrix before doping with the spectra of doped membranes. Special care will be done to the vibration bonds of the bending OH group of PVA, which are susceptible to be affected by the presences of dopant in their vicinity. In order to obsrev possible modification we recorded the spectrum of the pure PVA and then the spectrum of doped membranes, (Fig. 1). The most important bands observed in the spectrum of pure PVA are located at 1710 cm^{-1}, 1440 cm^{-1} corresponding to C-H and O-H bending mixture, 1232 cm^{-1} corresponding to C-H wagging, 1145 cm^{-1} corresponding to C-O and C-C bending, 918 cm^{-1} and 856 cm^{-1} corresponding to C-C torsion, [5, 6]. The peaks belonging to the doped samples appear at the following wave numbers: 1710 cm^{-1}, 1598 cm^{-1}, 1440 cm^{-1}, 1349 cm^{-1} 1232 cm^{-1}, 1145 cm^{-1}, 918 cm^{-1} and 856 cm^{-1}. For the doped membranes the Raman spectra were recorded at different concentration of black carbon, from 1% to 50%. Such spectrum contains the specific vibration bands of pure PVA, observed at the some wave membranes, 1710, 1440, 1232, 1145, 918 and 856 cm^{-1}. In addition, two intense bands were observed at 1349 cm^{-1} and 1598 cm^{-1}. Theirs amplitude increases significantly with the increase of the amplitude of carbon, whereas the amplitude of other bands remains almost constant. (Fig. 1).

Knowing that the amplitude of the vibration bands increases with the number of chemical bonds involved in such vibration, we conclude that these bonds are assigned to carbon dopants. On the other hand, the position of the specific vibration bands of the PVA, don’t change with the increase of the concentration. The Raman spectrum of the doped membranes contains the characteristic bands of pure PVA to which are added the bands corresponding to amorphous carbon.

Consequently, the spectrum of the doped sample appears as a simple superposition of spectra. Each component of this combination preserves its own identity, as the intermolecular bonds are weak physical bonds. From this observation we can conclude that none new chemical bonds appear between the dopant and the polymeric matrix.

Generally the interaction of high energy radiation, such gamma radiation, with the polymeric chains, has as effect the excitation of the electronic levels, ionization of the atoms and even breaking of some chemical bonds. Breaking of chemical bonds means the vanishing of vibrations associated to these bonds. In the Raman spectrum the effect is associated with the decrease of the amplitude of the vibration bonds corresponding to these vibrations, or in the extreme event where all the chemical bonds were broken, the complete vanishing of these bands. Comparison of the Raman spectra before and after irradiation is very useful to establish such effect of irradiation. For this propose, we recorded the Raman spectra for all the samples after irradiation at dose 8000 Gy.

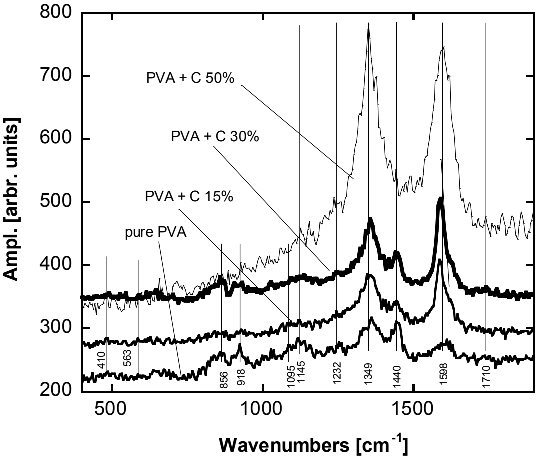

Fig. 1. The Raman spectra of pure PVA and PVA doped with different concentrations of black carbon.

The spectrum of the pure PVA irradiated at this dose contains the same vibration bands, without displacement, as the spectrum of pure PVA before irradiation (Fig. 2). Only a small modification of the amplitude of all the vibration bands was observed after irradiation. The main vibration bands at 856, 918, 1145 and 1440 cm^{-1} can be seen in both the spectra, (irradiated and un irradiated samples).

Similar behavior was observed also for the samples containing black carbon. We found peaks at 918, 1095, 1232, 1349, 1440 and 1598 cm^{-1}. It's observed only a slight decrease in amplitude of these bands, which is due to splitting of polymeric macromolecules, increasing of molecular dynamics and initiation of a rearrangement process of these molecules. The characteristic vibration bands of black carbon appear clearly in these spectra at the same wave numbers 1349 and 1598 cm^{-1} (Fig. 2). None vibration bands vanish completely after irradiation, meaning that the breaking effect of chemical bonds have only a limited character. These observations confirm the high chemical stability of this system even at moderate gamma exposure.

Although Raman spectroscopy gives complementally information concerning the local structure of the polymeric system, the more detailed characterization of the local order of polymeric chains, before and after irradiation, is provided by XRD method. Polymeric materials are know as amorphous materials, but in many situations, a local order arrangement of the polymeric chains, can occur [9].

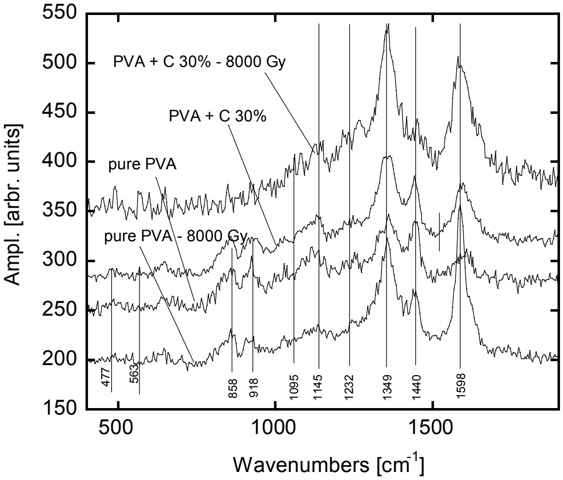

Fig. 2. Comparison between the Raman spectra of pure PVA and PVA with 30% Carbon in initial state and after gamma irradiation.

Such local structures, named crystalline domains, behave like a solid state crystalline network, producing maximum and minimum of interference when they are under the incidence of a parallel beam of X rays. The breaking of chemical bonds or scission of polymeric chains determined by gamma radiation can modify the size, and the distribution of such ordered structures in the entire volume of samples. The amplitude, the shape of width of diffraction peaks are correlated with the size and distribution of the ordered domains. Observing these parameters before and after irradiation we can describe the effect of radiation on the structure of the system.

Pure PVA exhibits a broad maximum of diffraction centered at 2θ = 19° by reflection on the bundles of macromolecular chains, where the persistence of a predominant distance between macromolecules generates some interference planes [7], (Fig. 3). This maximum of diffraction is associated pattern of the crystalline grid plan (1, 0, 1). The crystalline nature of PVA is determined by the hydrogen bonds occurring between H atoms and OH side groups of the same chain or parallel chains. The basic unit of such a structure is monoclinic with parameters a = 7.81Å, b = 2.5Å, c = 5.51Å and x = 91.42° and contains two vinyl alcohol monomer units (CH_2CHOH), [4, 8].

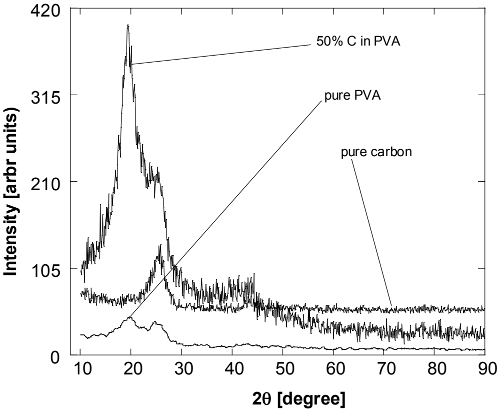

Fig. 3. The X-Ray difractogram for pure PVA, pure black carbon and PVA with 50% black carbon.

The difractogram of pure PVA is typical to amorphous substances or to substances with a low degree of crystalline structure.

The X-ray difractogram of doped PVA membrane contains specific peaks of pure PVA at 2θ = 19° and other one at 2θ = 25°, characteristic to black carbon (Fig. 3). The amplitudes of this peak increases with the carbon concentration but, at the lowest concentration of 1%, they are not visible in the spectrogram. However the deconvolution of difractogram shows clearly the existence of this peak for all the concentrations and its increase of amplitude with the concentration of carbon, (Fig 4).

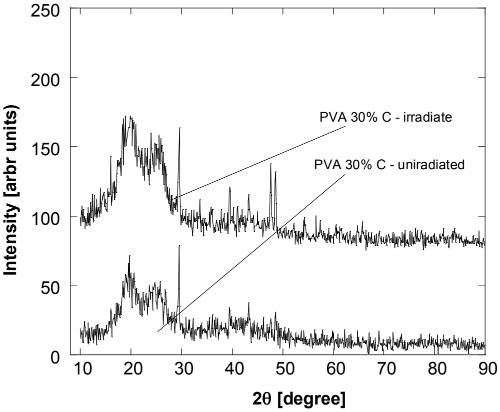

Fig. 4. The X-Ray difractogram of PVA doped membranes with 30% before and after gamma irradiation

The deconvolution shows only weak variation of the intensity of the PVA's peak with the carbon concentration, meaning that the local order of polymeric chains is not strongly affected by the presence of the black carbon. This conclusion is in accord with the Raman observation.

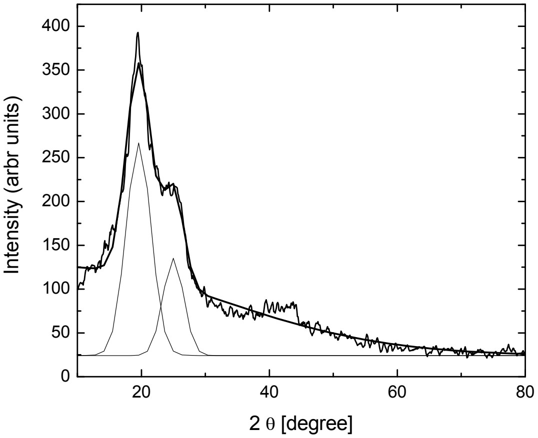

Fig. 5. Deconvolution of difractogram of PVA doped membranes with 30% black carbon

After the gamma irradiation, there weren't observed significant changes in the X-ray difractogram, only a small modification of the amplitude of the pure PVA is observed. This behavior can be attributed to a little modification of the local order of the polymer determined by possible breaking of the chains. The doped membranes behave after irradiation as the unirradiated ones, indicating good stability of the system, (Fig.5). Also these conclusions are in accord with the Raman observations.

CONCLUSIONS

PVA membranes doped with black carbon nanoparticles, having 1, 5, 15, 30 and 50% carbon concentrations from the initial mass, were prepared.

Raman spectra don't show modification of the vibration bands of the polymer after the introduction of the dopant. The bonds between the PVA polymeric macromolecule and the carbon atoms, used as dopants, are weak physical bonds. The polymeric matrix is characterized by amorphous state with a weak degree of local ordering. These characteristics remain unchanged after the introduction of black carbon nanoparticle. The difractograms show only an increase of the characteristic peaks of carbon with the increase of its concentration, without modification of the diffraction angle. The prepared membranes show enough stability at exposure to high doses of gamma irradiation. High-dose gamma irradiation causes low degree of scission of polymer macromolecules, followed by molecular rearrangement processes without modification of their chemical properties.

ACKNOWLEDGEMENTS

T. Stefan acknowledges *Investing in people!* Ph.D. scholarship, Project co-financed by the SECTORAL OPERATIONAL PROGRAM FOR HUMAN RESOURCES DEVELOPMENT 2007 – 2013, Contract nr.: **POSDRU/107/1.5/S/76841** – “Innovative doctoral studies in a Knowledge Based Society”, Babeş-Bolyai University, Cluj-Napoca, Romania.

REFERENCES

[1] C.-C. Yang, *J. Membrane Sci.,* 288 (2007) 51.

[2] X. Cui, F. Cui, Q. He, L. Guo, M. Ruan and J. Shi, *Fuel*, 89 (2010) 372.

[3] W.H. Eisa, Y.K. Abdel-Moneam, Y. Shaaban, A.A. Abdel-Fattah and A.M. Abou Zeid, *Mater. Chem. Phys.,* 128 (2011) 109.

[4] M. Todica, L. Udrescu and S. Simon, *Cent. Eur. J. Phys.,* 10 (2012) 329.

[5] Y. Badr and M.A. Mahmoud*, J. Mater. Sci.,* 41 (2006) 3947.

[6] S. Astilean, Methods and modern techniques of optical spectroscopy, Vol. 1, Home of Science Book, Cluj-Napoca, 2002.

[7] A. Rogojanu, C.F. Dascalu, B.C. Zelinschi, M. Caprosu and D.O. Dorohoi, *Spectrochim. Acta A,* 81 (2011) 334.

[8] H.M. Zidan, *Polym. Test.,* 18 (1999) 449.

[9] M. Todica, Proprietati fizice ale polimerilor*,* Presa Universitara Clujeana (2005).

STUDIA UBB PHYSICA, Vol. 57(LVII), 2, 2012, pp. 61-68
(RECOMMENDED CITATION)

SOLID STATE NMR PRELIMINARY STUDY ON ARCHAELOGICAL BONES

R.V.F. TURCU[a], B. KELEMEN[b], O. POPESCU[c,d], S. SIMON[a,*]

ABSTRACT. Bone is a composite material with a hierarchical structure. Human skeleton bones represent important resources for archeological investigations. This study reports preliminary results obtained by solid-state nuclear magnetic resonance on two-millennia old human bone artifacts. Hydrogen, carbon and phosphorus analysis allow structural characterization, which could be further useful in assessment of burial/cremation religious ritual, preservation methods, as well as preservation environment.

Keywords: *solid-state nuclear magnetic resonance, human bones, archaeology*

INTRODUCTION

Over the last decades magnetic resonance methods in general and nuclear magnetic resonance (NMR) in particular [1, 2] expand the fields of usage due to technological developments in areas like superconducting magnet, electronics, radio-frequency or mechanics/dynamic/flow [3-5]. Regardless of the state of the system as gaseous, liquid or solid, the method provides important molecular structure and dynamic information. In solid-state NMR the technique of Magic Angle Spinning (MAS) [6, 7] is the most widespread NMR method due to its capability of high resolution NMR spectra acquisition.

Bone comprises about 30% organic matrix, interwoven with a framework of about 70% poorly crystallized mineral matter composed primarily of calcium phosphate with a carbonated hydroxyapatite-like structure [8]. Postmortem processes

---

[a] Babes-Bolyai University, Faculty of Physics & National Magnetic Resonance Center, 1 Kogalniceanu, 400084 Cluj-Napoca, Romania

[*] Corresponding author: simion.simon@phys.ubbcluj.ro

[b] Babes-Bolyai University, Faculty of Biology & Molecular Biology Center of Interdisciplinary Research Institute on Bio-Nano-Sciences, 1 Kogalniceanu, 400084 Cluj-Napoca, Romania

[c] Babes-Bolyai University, Molecular Biology Center of Interdisciplinary Research Institute on Bio-Nano-Sciences, 1 Kogalniceanu, 400084 Cluj-Napoca, Romania

[d] Romanian Academy, Institute of Biology,125 Calea Victoriei, 010071 Bucharest, Romania

affecting human remains are themselves important for archeological sciences. These processes are most of the time associated with religious rituals. Depending on the burial/cremation rituals and on preservation environment, the bones structure can change and, indirectly, it can be used to characterize the processes to which the investigated bones were subjected [9, 10]. These changes are caused by multiple physical, chemical and biological factors and are named diagenesis [11]. The loss of nitrogen and carbon, the uptake of fluoride and uranium, and bone mineral crystallinity are examples of diagenetic phenomena which have long been used for relative dating purposes [12]. Mineral phase of the bone contains structural details that could deliver to archaeologists useful information for assessment of aspects related to funeral traditions and inclusively on the social status of the person the bone remains come from.

NMR studies bring information on the resonant elements/nuclei irrespective of whether the sample is crystalline or not. NMR is useful in giving structural information which may not be obtained from X-ray diffraction (XRD), either because the lack of peaks in case of the vireous samples or because as the phases are present in quantities too small to be detected by XRD. In addition, NMR also gives information about the presence and mobility of hydrogen atoms which are not detectable by XRD.

In this study we applied solid-state NMR and XRD analysis for a preliminary investigation of two millennia old human bone artifacts.

EXPERIMENTAL

Bone samples were collected from human skeletons found in archeological sites from highland Transylvania. Different skeleton parts were on-site and on-lab cleaned, then the samples to be analyzed were prevailed using a pneumatic drill machine with drill bit made of 316 stainless. Low diameter bit (300 µm) was used to better control the bone depth from which samples were collected. Investigated bone samples were collected from femurs of buried or incinerated adults.

The structure of the investigated samples was first analyzed by X-ray diffraction (XRD) with a Shimadzu XRD-600 diffractometer using Cu Kα radiation (λ=1.5418 Å).

^{1}H and ^{31}P solid-state MAS NMR analysis was performed on Bruker Avance III spectrometer operated at 14.1 Tesla magnetic field (^{1}H Larmor frequency 600.13 MHz and ^{31}P – Larmor frequency 242.93 MHz).

^{1}H and ^{31}P MAS NMR spectra were externally referenced relative to proton and phosphorus signal of tetramethylsilane and 85% phosphoric acid solution, respectively as 0 ppm. All spectra were processed using Bruker's TopSpin^{TM} [3] program and deconvoluted with DMfit [13].

RESULTS AND DISSCUSION

Bones are composite materials with a hierarchical structure. Heating and burning influence the structure of bone mineral phase and lead to a characteristic signature of structural change. This knowledge could deliver valuable information in the investigation of burned human remains from archaeological contexts in funerary practice.

The X-ray diffraction patterns of the investigated samples (Fig. 1) show hydroxyapatite (JCPDS 9-0432) as main crystalline phase. For the incinerated sample, a weak calcite diffraction line (JCPDS 5-0586) also occurs. Changes in crystallite size are notable, and a higher crystallinity is evidenced for the incinerated bone. The lack of CaO (JCPDS 82-1691) phase could prove that the incineration temperature was below 800 °C [14].

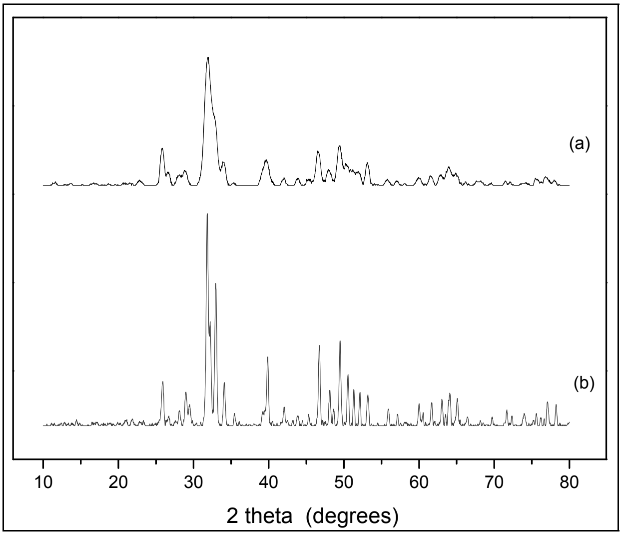

Fig. 1. XRD patterns of (a) buried and (b) incinerated bone samples.

In bone apatite the basic structural unit is PO_4 tetrahedron. The connectivity of PO_4 tetrahedra according to $Q^{(n)}$ terminology based on n-number of the bridging oxygen atoms is well delivered by ^{31}P MAS NMR analysis [15]. One of the four P – O bonds is double (P = O) while the other three are simple (P – O). Through these three oxygen atoms the PO_4 basic unit is further connected. Depending on the number of P–O–P bonds, the phosphate structural units are classified as $Q^{(n)}$ type units with n = 0, 1, 2, 3 [16].

For both bone samples, the ^{31}P MAS NMR spectra (Fig. 2) point out chemical shift and sidebands characteristic of hydroxyapatite (HAp). Buried bone sample spectra show a single peak, relatively broad, centered at about 2.0 ppm typical for amorphous materials. The peaks are covering $Q^{(0)}$ range which indicate a phosphate network depolymerization. The increased linewidth of top ^{31}P spectrum can be attributed to HAp with Ca substituted by ions like Mg and Zn [17, 18].

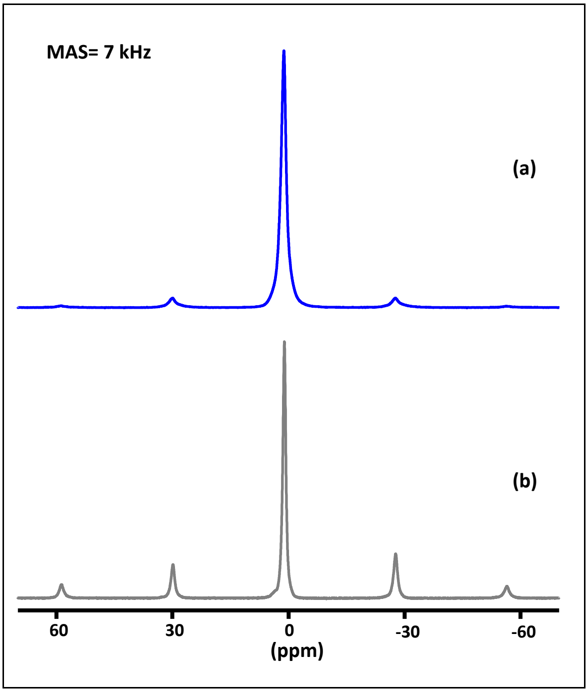

Fig. 2. ^{31}P MAS NMR spectra of (a) buried and (b) incinerated bone samples, recorded under magic angle spinning of 7 kHz.

At expanded scale (Fig. 3), one observes that the incinerated bone sample spectrum presents two quite narrow peaks with isotropic chemical shifts of 2.3 and 4.6 ppm, respectively which are not completely separated. The existence of two peaks slightly overleaped in the $Q^{(0)}$ range is due to the phosphorus with different second coordination sphere. The dominant peak at 2.3 ppm is attributed to pure hydroxyapatite ($Ca_5(PO_4)_3OH$) [19], while the second one may be attributed to calcium-deficient hydroxyapatite or to phosphate surface species. Calcium-deficient hydroxyapatites are structures in which Ca:PO_4 ratio is lower than 1.67, namely 1.33 for octacalcium phosphate ($Ca_8H_2(PO_4)_6{\cdot}5H_2O$) and 1 for dicalcium phosphate dihydrated ($CaHPO_4{\cdot}2H_2O$).

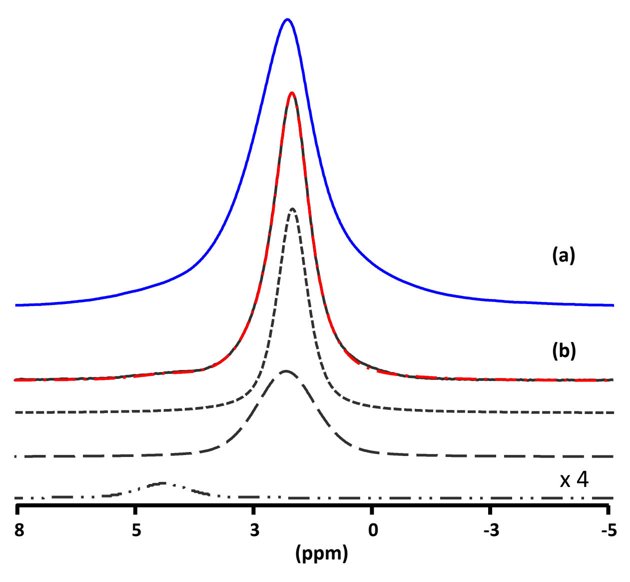

Fig. 3. ^{31}P MAS spectra of (a) buried and (b) incinerated bone samples and deconvolution of the latter one.

On the other hand the line broadening of the buried bone samples does not allow a unique Gaussian like line-shape simulation of multiple signals. Obviously, the line width for the incinerated sample is narrower than that of buried bone and the full width at half maximum could be further used to determine the specific surface area. The specific surface are values of apatites in bone cementum cannot be measured directly using standard adsorption methods. The obstacle is the organic matrix. Instead, it can be estimated using ^{31}P MAS NMR by comparison linewidths of cross-polarization and Bloch-decay peaks, because it was demonstrated [20] that the linewidth parameter shows explicit dependence on specific surface area.

The bone mineral phase in these samples was further described by ^{1}H NMR analysis. The peak coming from Hap's OH group is centered at 0.8 ppm and in the buried bone sample is overlapped by other broad signals (Fig. 4). These are attributed to both organic and inorganic phases entering the bone structure, and also to new structures formed by bone – environment interaction over the time [21, 22]. A broad feature, centred around 5 ppm can be assigned to the presence of hydration water, an intense signal at 4.8 ppm was reported as typical of $CaCO_3,\cdot nH_2O$ and $NaHCO_3$ and could be associated to calcite which was deposited on bones by groundwater [23].

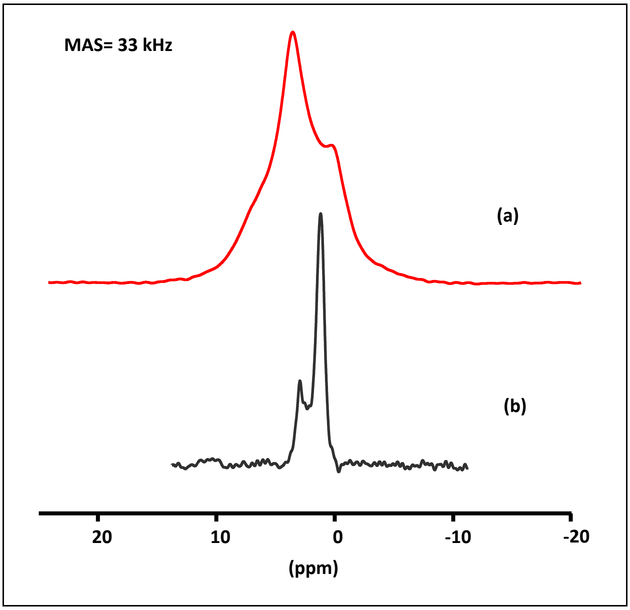

Fig. 4. ^{1}H MAS NMR spectra of (a) buried and (b) incinerated bone samples, recorded under magic angle spinning of 33 kHz

It was also reported [23, 24] that a signal around 1.7 ppm in 1H MAS NMR spectra is related to type-I collagen of the organic phase of bone and the diminishing of this signal shows the degradation of collagen during the time. The lack of any future around 1.7 ppm suggests that none of the investigated samples kept undegradated collagen.

The higher crystallinity of hydroxyapatite phase is even better shown by ^{1}H MAS spectrum of incinerated sample (Fig. 4). Not that the heat lead to organic phase disintegration but the temperature value itself was high enough to increase the crystallization level.

CONCLUSION

Both buried and incinerated bone samples overwhelmingly consist of mineral hydoxyapaptite phase. The XRD analysis suggests that the firing temperature of the incinerated bone was bellow 800 ^{o}C. Changes obtained in the full width at half maximum of ^{31}P MAS NMR analysis could be further used to determine the specific surface area values. ^{1}H MAS NMR results of two millennia old human bone artifacts suggest that none of the investigated samples kept undegradated type-I collagen.

The preliminary data obtained in this study present solid-state NMR capability to investigate this type of complex materials in which amorphous and crystalline, organic and inorganic phases coexist.

ACKNOWLEDGEMENTS

This research was co-financed by project "Socio-humanistic sciences in the context of global evolution – the development and implementation of studies and postdoctoral research" code POSDRU/89/1.5/S/61104, project financed by European Social Fund through Sectorial Operational Program for Human Resource Development 2007-1013.

REFERENCES

1. F. Bloch, W.W. Hansen, M. Packard, *Phys. Rev*., 69, 127 (1946).
2. E.M. Purcell, H.C. Torrey, and R.V. Pound, *Phys. Rev*., 69, 37 (1946).
3. www.bruker-biospin.com/nmr.html
4. http://www.chem.agilent.com/en-US/Products-Services/Instruments-Systems/Nuclear-Magnetic-Resonance/Pages/default.aspx
5. www.revolutionnmr.com
6. E.R. Andrew, A. Bradbury, R.G. Eades, *Nature,* 182, 1659 (1959).
7. I.J. Lowe, *Phys. Rev. Lett.*, 2, 285 (1959).
8. A. Sillen, 1989. Diagenesis of the inorganic phase of cortical bone. In: Price, T.D. (Ed.), The Chemistry of Prehistoric Human Bone. Cambridge University Press, Cambridge, pp. 211–229.
9. F.M. Guarino, F. Angelini, C. Vollona, C. Orefice, *J. Archaeol. Sc*i., 33, 513 (2006).
10. A.R. Liveres, A.W. Weber, O.I. Goriunova, *J. Archaeol. Sci*., 33, 1141 (2006).
11. S. Pfeiffer, Palaeohistology: health and disease, in: *Biological Anthropology of the Human*; Skeleton M.A. Katzenber, S.R. Saunders (Eds.), Wiley-Liss, New York, 2000, pp. 287-302.
12. A. Sillen, J. Parkington, *J. Archaeol. Sci.,* 23, 535 (1996).
13. D. Massiot, F. Fayon, M. Capron, I. King, S. LeCalve, B. Alonso, J.O. Durand, B. Bujoli, Z. Gan, G. Hutson, *Magn. Reson. Chem*., 40, 70 (2002).
14. L.E. Munro, F.J. Longstaffe, C.D. White, *Palaeogeogr. Palaeocl*., 249, 90 (2007).
15. C. Mirestean, H. Mocuta, R.V.F. Turcu, S. Simon, *J. Opt. Adv. Mat*., 9 (3), 764 (2007).
16. R.K. Brow, *J. Non-Cryst. Solids,* 263&264, 1-28 (2000).

17. M. BraunP. Hartmann, C. Jana, *J. Material Sci: Mat. In Med.,* 6, 150 (1995).
18. E. Fujii, M. Ohkubo, K. Tsuru, S. Hayakawa, A. Osaka, K. Kawabata, C. Bonhomme, F. Bobanneau, *Acta Biomaterialia, 2, 69* (2006).
19. C. Jager, T. Wlzel, W. Meyer-Zaika, M. Epple, *Magn. Reson. Chem*., 44, 573 (2006).
20. J. Kolmas, A. Slosarczyk, A. Wojtowicz, W. Kolodziejski, *Solid State Nucl. Magn. Res.,* 32, 53 (2007).
21. M.E. Malainey, *A Consumer's Guide to Archaeological Science. Analytical Techniques*, in: Manuals in Archaeological Method, Theory and Techniques, Orser, Jr., Charles, E., Michael, B. (Eds.), Springer, 2011
22. E.M. White, L.A. Hannus, *Am. Antiq*., 48, 316 (1983).
23. D. Alfano, A.R. Albunia, O. Motta, A. Proto, *J. Cult. Herit.,* 10, 509 (2009).
24. D. Capitani, V. Di Tullio, N.Proietti, *Prog. Nucl. Magn. Res. Sp.*, 64, 29 (2012).

STUDIA UBB PHYSICA, Vol. 57(LVII), 2, 2012, pp. 69-80
(RECOMMENDED CITATION)

OPTICAL WAVEGUIDE AMPLIFIERS IN HIGHLY ER-DOPED SILICA GLASS SUBSTRATES

PAREKHAN M. ALJAFF[a]

ABSTRACT. Short amplifiers are currently attracting increased interest, especially for use in integrated optics. In this study the simulated gain performance and noise figure of Erbium doped on Silica glass substrate pumped in the forward direction are obtained taking into account the up conversion effect from the Er^{3+} levels ($4I_{13/2}$ and $4I_{11/2}$). The influence of waveguide length, pump power, Er-doping concentration and the co-operative up-conversion coefficient on the gain curves and on the waveguide noise figure is studied. Optimum results are obtained using a 3-cm length waveguide at Erbium ions density of N_{Er} (15×10^{26} at/m^3) and at the up-conversion coefficient value of $1x10^{-24}$ m^3/s^{-1}. The up-conversion process, however, puts limits on both the amplifier gain and the maximum favorable concentration.

Keywords: *Erbium, waveguide amplifiers, optical amplifiers, waveguide components*

INTRODUCTION

Erbium-doped silica fiber pumped at 1480 nm or 980 nm shows a linear gain response, temperature insensitivity over 100 °C, polarization independence and a low noise figure [1], which are all properties predetermining the use of erbium doped waveguide amplifiers (EDFA) in commercial transmission systems. On the other hand, the typical length of an EDFA is up to 50 m, which limits its applicability in the access networks where compact and integral devices are desired. Therefore, in the last fifteen years the attention was turned to the planar analogy of EDFAs, erbium doped waveguide amplifiers (EDWA). In EDWAs the signal enhancement is achieved in a few cm long, highly doped waveguide, which can be integrated with other functions to produce lossless' and small-size network components.

---

[a] Department of Physics, College of Science, University of Sulaimania, Iraq

Waveguide amplifiers fabricated in multicomponent silicate and phosphate glass substrates belong among the most common and successful EDWA realizations. Glass as a substrate material for integrated optics has many advantages: is highly transparent, mechanically rigid and stable, relatively cheap and compatible with the current commercial fiber technology. Furthermore, by adjusting the glass composition one can control important optical and spectroscopic properties. In this way, the amplifier substrates may be optimized and amplifiers without standing performance are achieved. To date, a number of glass waveguide amplifiers has been presented and it was demonstrated that Er-doped glasses are suitable as tunable laser sources as well as broadband signal amplifiers in modern Wave Division Multiplexing networks[2-3].

The main topics studied in this paper is the signal gain and noise figure variations with the waveguide lengths, pump power, Er-ion density and the co-operative up-conversion at higher value of Erbium ion density [4].

THEORY

Since the advent of Erbium doped fiber amplifiers, researchers have investigated the possibility of reducing the size of an Optical Fiber Amplifiers (OFA) to be comparable to an Semiconductor Optical Amplifiers (SOA). The primary restriction was the active fiber length (<3 m); hence, the desire to replace this fiber with a planar waveguide. The Planar Waveguide Amplifier (PWA) is basically the same as the OFA, except that the active fiber is replaced by an active planar waveguide and the Wave Division Multiplexing (WDM) is usually integrated on the same substrates.

The doped waveguide may present more than one mode at the pump or at the signal frequencies/wavelength. This is common in integrated optics, in which the discontinuity between the refractive index of the core and the cladding is raised on purpose to provoke a high confinement of the pump field and, thus, obtain higher gain [5].

We can presume that the device is externally excited by a beam with Gaussian field distribution $\Phi(x, y, \omega)$, with different spatial widths at the pump and signal wavelengths. This supposition is experimentally sustained when a beam that it is being coupled through a set of lenses excites an integrated optical device. Consider that at the wavelengths λ_s and λ_p (signal and pump wavelength, respectively), N_s and N_p modes with field's distributions ϕ^i $(x, y, \lambda_{s/p})$ can propagate. The input beam can then be described through a modal expansion of the modes present in the waveguide, that is:

$$\Phi(x, y, \lambda_{s/p})_{gauss} = \sum_{i=1}^{N_q} c_i \phi(x, y, \lambda_{s/p})_i \qquad \ldots\ldots\ldots\ldots 1$$

Where N_q can assume N_s and N_p, and C_i represents the coupling coefficient between the field of the Gaussian input beam and the field of the corresponding mode. Then, the fraction of the total power allocated in each expansion mode for the pumping and for the signal will be;

$$\eta_{pi} = \frac{c_{pi} c_{pi}^*}{\sum_{j=1}^{N_p} c_{pj} c_{pj}^*} \qquad \ldots\ldots\ldots\ldots 2$$

$$\eta_{si} = \frac{c_{si} c_{si}^*}{\sum_{j=1}^{N_s} c_{sj} c_{sj}^*} \qquad \ldots\ldots\ldots\ldots 3$$

In this way, for multimode waveguides, the normalized intensity profile for the signals and the pump can be calculated as;

$$\Psi_{s/p} = \sum_{i=1}^{N_q} \eta_{si/pi} \Psi_{s/p}^i \qquad \ldots\ldots\ldots\ldots 4$$

where ψ^i_s (x, y) and ψ^i_p (x, y) are the normalized intensity profiles at the signals and the pump wavelength, respectively. In this way, for multimode waveguides, the normalized intensity profile for the signals and the pump can be calculated as:

$$I_s(x, y, z) = \Psi_s(x, y) P_s(z) \qquad \ldots\ldots\ldots\ldots 5$$

$$I_p(x, y, z) = \Psi_p(x, y) P_{p(z)} \qquad \ldots\ldots\ldots\ldots 6$$

$$I^j_{ASE\pm}(x, y, z) = \Psi_s(x, y) P^j_{ASE\pm}(z) \qquad \ldots\ldots\ldots\ldots 7$$

SIMULATION RESULTS

Optical gain measurements were performed on 3-cm long waveguide sample using the experimental setup depicted in Fig. 1. The waveguide parameter's are shown in Table 1.

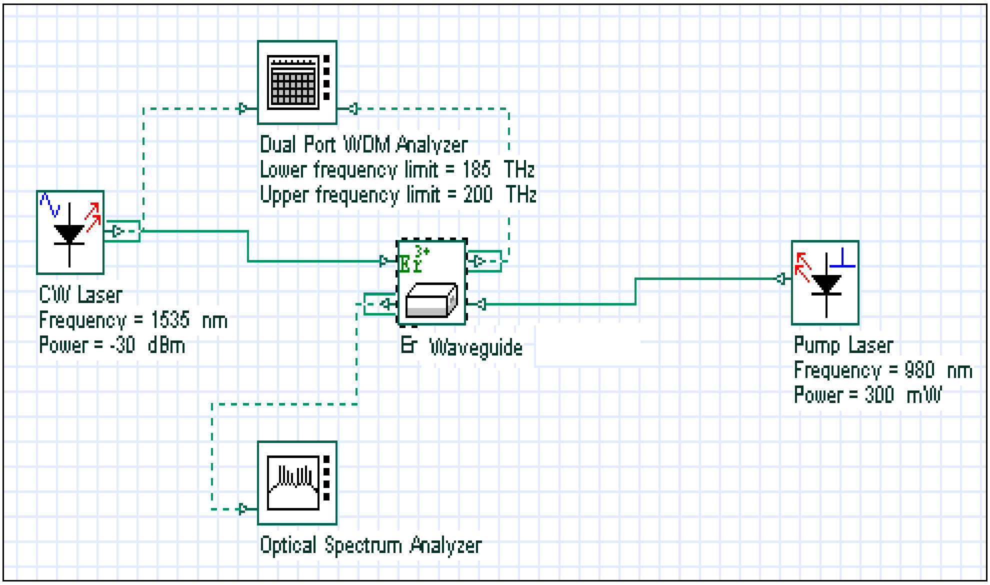

Fig. 1. Devise configuration

Table 1. Waveguide characteristics

Name	Value	Units
Er ion density	1.5exp (27)	m^{-3}
Er metastable lifetime	11	ms
Er signal excess loss	80	dB/m
Er pump excess loss	100	dB/m

A. Signal Gain Variation with Pump Power and Waveguide Length

The typical signal gain characteristics were examined for a purely Er-doped amplifier as function of pump power and the active waveguide length. In Fig. 2 the signal gain dependence on the amplifier length is plotted for four different pump powers. Initially, the signal gain increases approximately linearly with the amplifier length and starts to saturate. Naturally, the higher the pump power, the longer the propagation distance at which the saturation occurs. For given pump power there always exist an optimum waveguide length above which the amplifier performance is strongly degraded. For instance, since the waveguide losses are rather high relatively high pump powers of order of 100 mW are needed to achieve a sufficient gain.

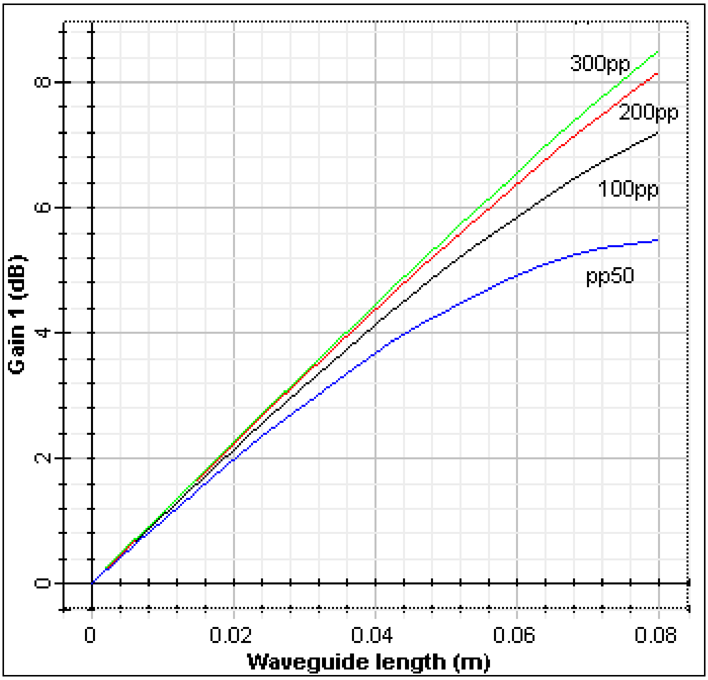

Fig. 2. Signal gain versus amplifier length for four different pump powers (50, 100, 200 and 300mW)

Table 2. Spectroscopic characteristics

Name	Value
Signal wavelength	λ_s 1535 nm
Pump wavelength	λ_p 980 nm
Signal power	-30dBm

Figure 3 shows the plot of signal gain versus pump power calculated for four different waveguides varying in their lengths. Short waveguides exhibit a low threshold power (the pump power at which the amplifier gain just compensates the waveguide losses), however, the maximum achievable gain is low. On the contrary, long waveguides must be pumped heavily to overcome the propagation losses, but the saturated gain reaches much higher values. The maximum achievable gain increases approximately linearly with the amplifier length.

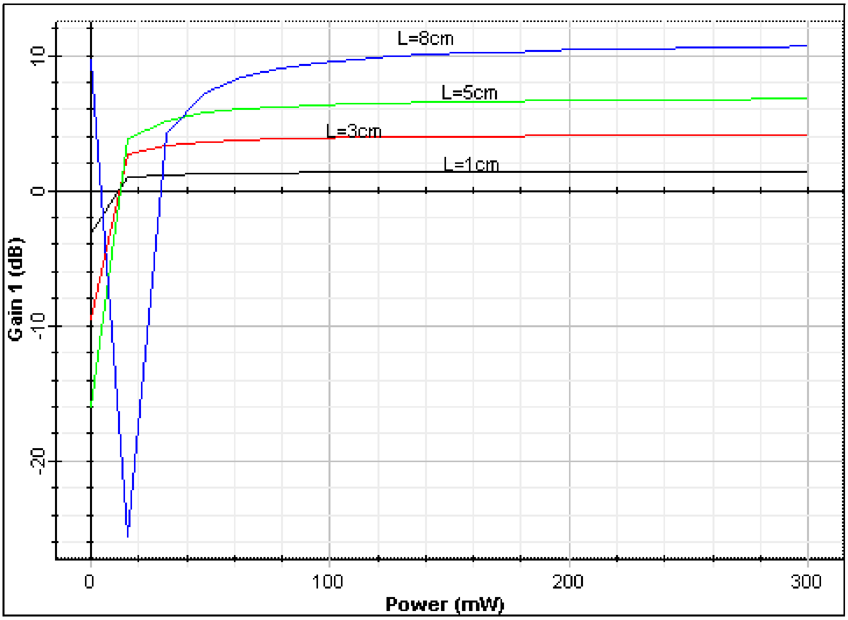

Fig. 3. Signal gain as a function of pump power for varying waveguide length, at $C_{up} = 1 \times 10^{-24}\ m^3/s^{-1}$.

B. The Influence of Er^{3+} Concentration and Co-Operative Up-Conversion

The co-operative up-conversion is a substantial gain limiting process that becomes important especially at high Er^{3+} doping concentrations. Since the up-conversion and Er^{3+} doping level are linked closely together, it is almost impossible to discuss their effects on the amplifier performance separately.

First, the influence of erbium concentration is studied for a case of $C_{up} = 1 \times 10^{-24}\ m^3/s^{-1}$, and shown in Figure 4 the signal gain versus propagation length is shown for five different values of N_{Er}, varying from 0.5×10^{26} at/m^3 to 15×10^{26} at/m^3. The pump power is set to 100 mW. The maximum achievable gain increases with increasing erbium concentration and the optimum propagation length decreases.

A 33dB gain is obtained at $N_{Er} = 15 \times 10^{26}$ for 3-cm length waveguide. In literature at N_{Er}.= 1.1×10^{25} at/m^3 the gain obtained is only 4 dB [4].

The effect of up-conversion is shown also in Figure 5 where the signal gain is plotted as a function of Erbium ion density for three different up-conversion coefficients $C_{up} = 1 \times 10^{-25}$, 1×10^{-24} and $1 \times 10^{-23}\ m^3/s^{-1}$.

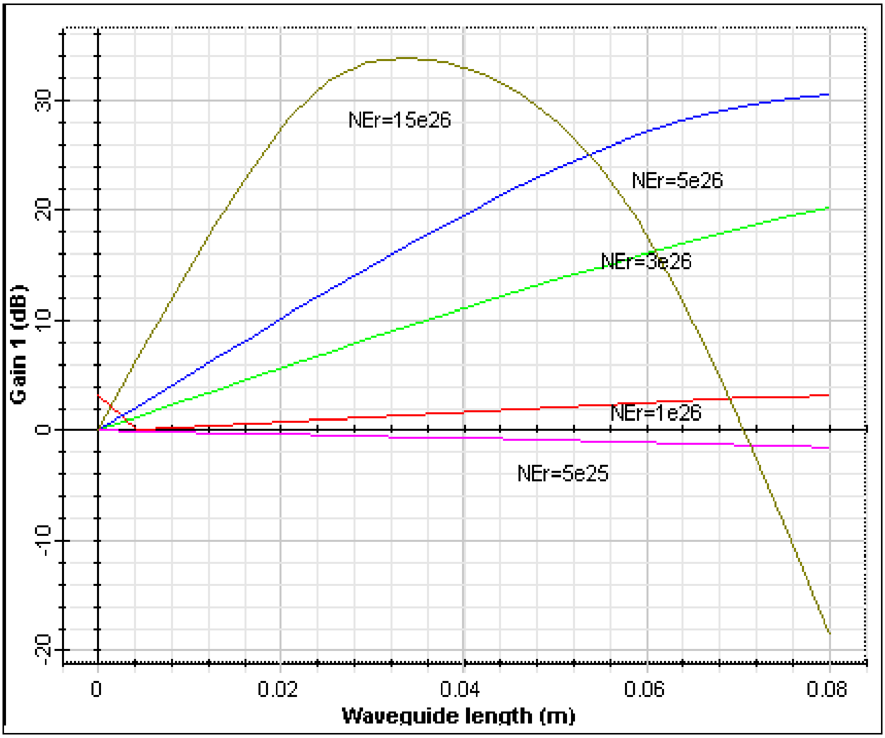

Fig. 4. The influence of Er^{3+} concentration on signal gain for up-conversion coefficient C_{up} = 1 x10^{-24} m^3/s^{-1} .

Figure 5 proves that at higher up conversion values the overall gain is almost lower than in the lower cases especially at higher Er3+ concentrations the influence of up-conversion is enhanced and the maximum achievable gain decreases. For low up-conversion values the maximum possible Er-doping level would be desired and a high optical gain could be achieved. The up-conversion process, however, puts limits on both the amplifier gain and the maximum favorable erbium concentration.

The effect of up-conversion is also demonstrated in Figure 6 where the signal gain is plotted as a function of pump power for three different up-conversion coefficients C_{up} =1x10^{-25}, 1x10^{-24} and 1x10^{-23} m3/s^{-1}. A three dB maximum gain is obtained for C_{up} = 1x10^{-24} m3/s^{-1} at 100 mW.

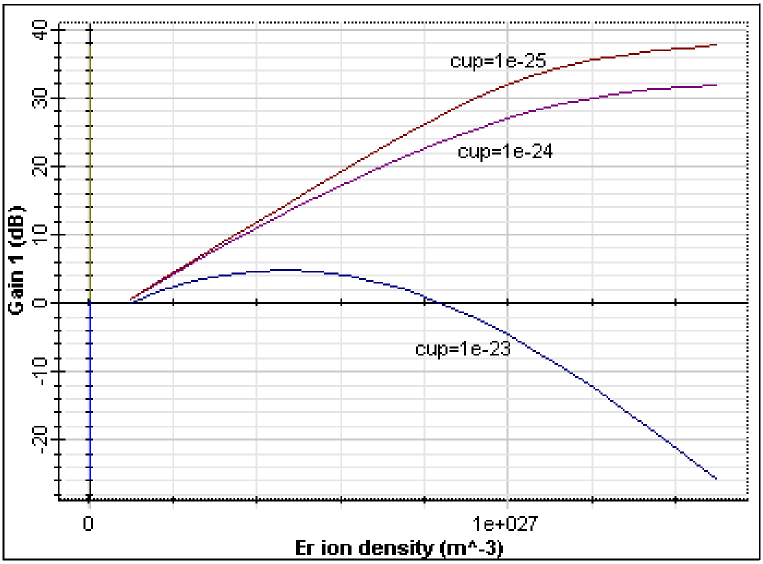

Fig. 5. Gain versus Er^{3+} concentration for three different up-conversion coefficients values.

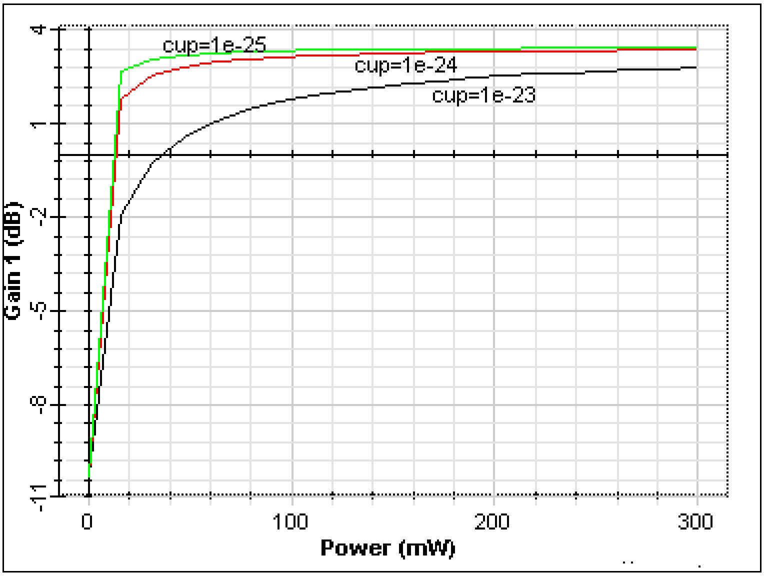

Fig. 6. The influence of the co-operative up-conversion on the amplifier gain plotted as a function of pump power. The up-conversion coefficients $C_{up} = 1x10^{-25}$, $1x10^{-24}$ and $1x10^{-23}$ m3/s^{-1} were considered.

C. The Influence of Noise Figure (NF)

The amplified spontaneous emission represents a major source of amplifier noise and it can deteriorate the amplifier performance especially for long and low loss waveguides. The noise as consequence of amplified spontaneous emission is depicted in Figures 7, 8 and 9 for a 3-cm long Erbium-doped waveguide amplifier pumped at 100 mW.

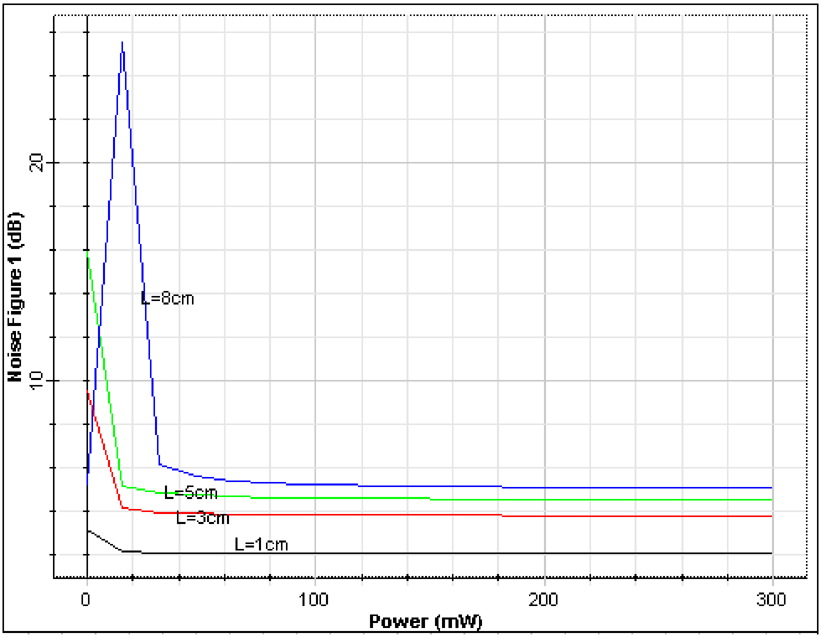

Fig. 7. The variation of noise with signal input power

Figure 7 shows the noise figure variation as function of pump power for different fiber lengths (1, 3, 5 and 8 cm) at -30 dBm signal input power and constant erbium ion density, N_{Er} =15x10^{26}, the noise figure decreases with increasing the pump power, and at low pump power the noise figure is large for longer fiber length than shorter fibers.

The variation of noise figure with waveguide length for five different values of N_{Er} is shown in Figure 8, for a waveguide of 3-cm lengths, the noise value is approximately constant and not changed by changing N_{Er}. At the maximum value of N_{Er} = 1.5exp27 the noise obtained is 4 dB, the typical value of noise figure in erbium waveguide amplifiers is from 4 to 5 dB.

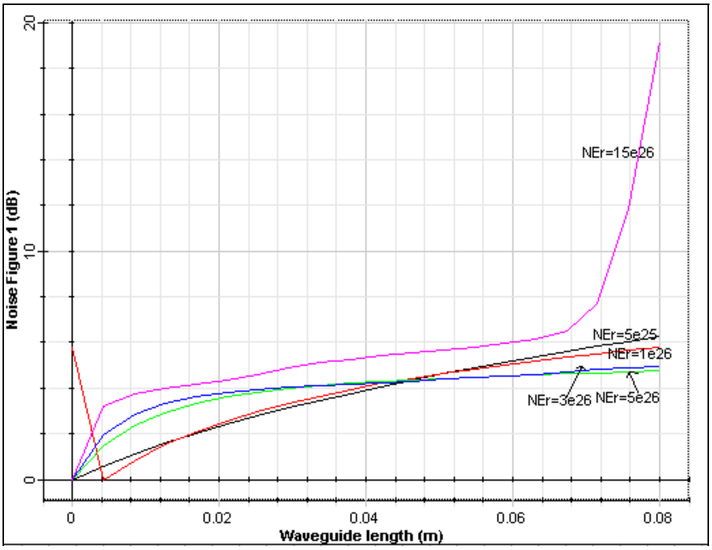

Fig. 8. The variation of noise figure with waveguide lengths at different values of N_{Er} (3exp26-15exp26) an C_{up} =1x10^{-24} m3/s^{-1}.

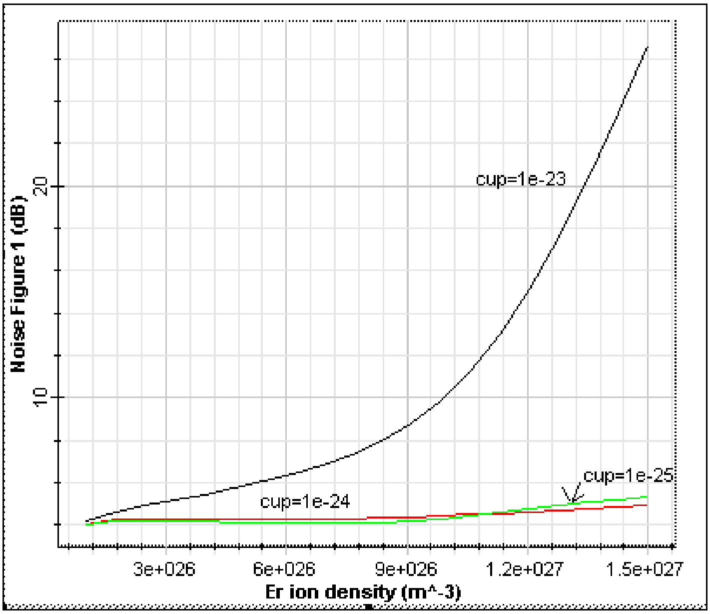

Fig. 9. The influence of the co-operative up-conversion on the amplifier noise figure plotted as a function of Er-ion density the up-conversion coefficients C_{up} = 1x10^{-25}, 1x10^{-24} and 1x10^{-23} m^3/s^{-1} were considered.

In Figure 9 the obtained noise at Cup = $1x10^{-23}$ is noticeable and increases with Er-ion density. Especially at higher Er3+ concentration the influence of up-conversion is enhanced and the achievable noise increases. On the contrary the obtained noise at the other two values of Cup $1x10^{-24}$ and $1x10^{-25}$ m3/s−1 is low and not changes by changing the Er3+ density.

CONCLUSION

1. First the typical signal gain characteristics were examined for a purely Er-doped amplifier as function of pump power and the active waveguide length. The results demonstrates that a maximum gain is obtained for a waveguide amplifier of length 3 cm at 100 mw pump power.
2. Second part of the amplification measurement consisted in determining the influence of Er^{3+} concentration on signal gain for different waveguide lengths, at Erbium ion density (1.5xexp27*)* and *C*up = ($1x10^{-24}$ m^3/s^{-1}) at waveguide length of 3cm.The results obtained from the up-conversion coefficients prove that at height Er^{3+} concentrations the influence of up-conversion is enhanced and the maximum achievable gain increases. Maximum gain and minimum noise figure obtained at C_{up} = ($1x10^{-24}$ m^3/s^{-1}).
3. The NF is strongly dependence on the waveguide length, Erbium ion density and the up-conversion coefficients value. A 3-cm length waveguide has a typical value of noise of 4 dB for the values fixed in the tables.

REFERENCES

[1] Barbier, D. and Hyde, L.: Erbium Doped Glass Waveguide Devices. Integrated Optical Circuits and Components, edited by E. J. Murphy, chap. 5, pp. 89–126, New York: Marcel Dekker, ISBN 0-8247-7577-5, 1999.

[2] Čapek, P.: Erbium Doped Planar Waveguides in Dielectric Materials. Ph.D. thesis, Czech Technical University in Prague, Faculty of Electrical Engineering, Praha, 2004.

[3] Philipsen, J.L. *et al.*: Erbium-Doped Waveguide Amplifier Technology and Components, In 29th European Conference on Optical Communication, Rimini, 2003.

[4] Jageriska Jana: Optical Waveguide Amplifiers in Er-Doped Glass Substrates, Diploma Thesis, 2006.

[5] Barbier, D.: Performance and Potential Applications of Erbium Doped Planer Waveguides and Lasers. Optical Amplifiers and their Aplications victorea, B.C. Canada 72-92, 1997.

[6]. Federighi, M. and Di Pasquale, F.: The Effect of Pair-Induced Energy Transfer on the Performance of Silica Waveguide Amplifiers with High Er+3 Concentration", IEEE Photonics Technology Letters, Vol.7, No.3, p.303-305, 1995.

[7] Honkanen, S., Najafi, S.I. and Wang, W.J.: Composite Rare-Earth Doped Glass Waveguides, IEEE Electronics Letters, V ol.28, No.8, p.746-747, 1992.

STUDIA UBB PHYSICA, Vol. 57(LVII), 2, 2012, pp. 81-89
(RECOMMENDED CITATION)

A NEW APPROACH: ^{29}SI MAS NMR AND EDX APPLIED TO THE STUDY OF MIDDLE BRONZE AGE POTTERY

M. VASILESCU[a, b, c,*], A.A. FARCAŞ[a], V. VASILACHE[d], N. BOLOHAN[b, e]

ABSTRACT. For many millennia ceramics was the main material used for storage or food preparation. Archaeological sites usually contain large amounts of pottery, which can be used for cultural and chronological assessment. Ceramic fragments belonging to Middle Bronze Age in Eastern Romania were analyzed by ^{29}Si MAS NMR spectroscopy for characterization of the local structure. Quantitative analyze was done for different structural arrangements: Q^2, Q^3, Q^4. We obtained the elemental composition by EDX spectroscopy. We compared the results for two pottery groups, Monteoru and Costişa, all samples being founded in the same archaeological site.

Keywords: *NMR, EDX, Middle Bronze Age, Pottery*

INTRODUCTION

The NMR (Nuclear Magnetic Resonance) spectroscopy is one of the most frequently used methods of analysis for study of ceramics and glasses [1-3]. However, NMR techniques were rarely used to study pottery from the Bronze Age. A literature search reveals no report about the study on such materials by ^{29}Si Magic Angle Spinning (MAS) NMR and Energy Dispersive X-ray (EDX).

Nuclear Magnetic Resonance Spectroscopy applied to Bronze Age ceramics can be useful for cultural framing of the monument, determination of the technology or the relationship with neighboring and contemporary civilization [4].

---

[a] Babes-Bolyai University, Faculty of Physics, 1 Kogalniceanu str., 400084 Cluj-Napoca, Romania
[b] Babes-Bolyai University, Interdisciplinary Research Institute on Bio-Nano-Sciences, 42 Treboniu Laurian str., 400271 Cluj-Napoca, Romania
[c] Romanian Academy, 125 Calea Victoriei, 010071 Sector 1, Bucharest, Romania
*Corresponding author: mihai.vasilescu@phys.ubbcluj.ro
[d] Alexandru Ioan Cuza University, ARHEOINVEST Interdisciplinary Platform, 22 Carol I Bd, 700506 Iasi, Romania
[e] Alexandru Ioan Cuza University, Faculty of History, 11 Carol I Bd., 700506 Iasi, Romania

In this study solid-state MAS NMR has been used to monitor structural composition and phases of different ceramic fragments belonging to Middle Bronze Age found in archaeological sites from Costişa, Neamţ County, Romania. Significant differences were found between the results of analyzes.

CULTURAL BACKGROUND

The Costişa and the Monteoru pottery groups represent for the area situated in Eastern Romania the main cultural and chronological frame for the final stage of the Early and Middle Bronze Age.

Even if there are a lot of archaeological results coming out from the eponymous site, there is a permanent need for improving the image about it. Thus, starting with the first assertion concerning the periodization and chronology of the Costişa pottery group, the eponymous site was considered that it belongs to the Middle Bronze Age. The area under study was marked by the contact with different communities belonging to the Southern Monteoru group. They have contributed in good measure to reconfigure the Middle Bronze Age in Moldavia. This idea is confirmed by the archaeological excavations in Siliştea, Borleşti and other places situated in west-central Moldavia, mainly in the Cracău-Bistriţa depression.

Recently, based on combining archaeological data with the radiometric ones was reconfirmed the position of Costişa site as belonging to the Middle Bronze. [5, 6]

EXPERIMENTAL

For this study a number of seven shards of pottery taken from the archaeological site of Costişa were selected, named 1C to 7C, the most representative ones, in good conservation state. According to macroscopic observation made by archaeologists the samples 2C, 4C, 6C represent Monteoru pottery group, while the samples 1C, 3C, 5C, 7C are part of Costişa pottery group.

For elemental compositional analysis was used a scanning electron microscope, SEM (Scanning Electron Microscopy) VEGA II LSH model, manufactured by Czech TESCAN, coupled with an EDX detector type QUANTAX QX2, made by BRUKER / ROENTEC Germany. In the last few decades, SEM-EDX techniques have been used increasingly for the analysis of ceramics of this type, providing information about their production process [7].

^{29}Si MAS NMR spectra were recorded with a Bruker Avance 400 Ultra Shield NMR spectrometer, operating at 9.4 Tesla, a rotor of 4 mm diameter and spinning frequency of 8 kHz. For analysis was taken a quantity of about 500 mg per sample and grinding was done to it, thus obtaining a powder. TMS (tetramethylsilane $Si(CH_3)_4$) was used as a reference for reported isotropic chemical shifts.

In oxides, silicon is usually surrounded by four oxygen atoms, forming SiO_4 tetrahedra. One tetrahedron can be connected to other n tetrahedra, via oxygen (Q^n, n = 0, 1, 2, 3, 4) [8]. ^{29}Si NMR isotropic chemical shift shows the type of local structure in which silicon atoms are found.

The deconvolution of the ^{29}Si MAS NMR spectra was performed using DMFIT software [9-10].

RESULTS AND DISCUSSION

According to I. Sandu et al. [11, 12] in the case of ancient pottery, the average values of the gravimetric concentration are relevant in archaeometry for Fe, Ca, Na and Ti. Nevertheless, equally important are the Si/Al ratio (caustic module), the Ca/Mg ratio (alkaline-earth module) and the K/Na ratio (alkaline module), evaluated from weight percent (gravimetric concentration).

For all samples was studied the structure and elemental composition of the inside part, leaving the analysis of the surface (engobe) for a future study. After the elemental composition determination through EDX spectroscopy, on all potteries has been identified the presence of the following elements: Si, Al, Fe, Ca, Mg, K, Na, P, Ti and O (Table 1).

Table 1. Elemental composition of the Costişa pottery

Sample	**Weight %**									
	Fe	**Ca**	**Na**	**Ti**	**O**	**Si**	**Al**	**P**	**Mg**	**K**
1C	5.28	1.93	0.78	0.78	42.58	29.62	10.75	2.04	1.53	3.15
2C	4.86	2.53	0.39	0.75	41.50	31.36	11.81	2.38	1.22	3.20
3C	5.82	1.86	0.52	0.66	39.56	33.47	11.81	2.43	1.30	2.57
4C	5.25	2.09	0.74	0.70	41.07	33.38	11.00	1.45	1.36	2.96
5C	4.82	2.89	0.65	0.65	42.32	30.47	11.71	2.29	1.48	2.72
6C	6.52	2.53	0.60	1.05	42.23	25.27	11.97	6.51	0.90	2.42
7C	4.73	2.83	0.73	0.88	43.76	31.30	10.08	1.94	0.96	2.79
average	**5.33**	**2.38**	**0.63**	**0.78**	**41.86**	**30.70**	**11.30**	**2.72**	**1.25**	**2.83**

For Costişa samples the caustic module (Si/Al ratio) takes values between 2.11 (sample 6C) and 3.11 (7C), with the average of 2.73, the biggest deviation being observed for the shard 6C (Table 2).

The alkaline-earth module for our samples is between 1.26 (sample 1C) and 2.93 (7C), with an average value of 2.00, indicating that this elements are present residues from the combustion. A more aggressive type of soil will increase the Ca/Mg ratio more than 3.00. This corresponds to a contamination from the soil, but we have no such sample here.

Table 2. Si/Al ratio (caustic module), Ca/Mg ratio (alkaline-earth module) and K/Na ratio (alkaline module) for Costişa pottery.

Sample	**weight % ratio**		
	Si/Al	**Ca/Mg**	**K/Na**
1C	2.75	1.26	4.04
2C	2.66	2.08	8.17
3C	2.83	1.43	4.90
4C	3.04	1.54	4.02
5C	2.60	1.96	4.15
6C	2.11	2.81	4.02
7C	3.11	2.93	3.83
average	**2.73**	**2.00**	**4.73**

The K/Na ratio shows the dynamics of the ion exchange, linked to saline soil load. If the alkaline module is high, than is possible to have a more saline soil. This could be the case for the sample 2C (K/Na = 8.17).

Analyzing elemental composition in the case of Costişa shards, we can easily observe that the sample 6C shows more extreme values, suggesting that this object was made of different materials than the other six.

Also, the sample 3C shows values much different than the average of other samples.

NMR spectra allow us to identify the local order around the nuclei. We obtained ^{29}Si MAS NMR spectra for all samples (Fig. 1), using a spectrometer operating at 9.4 Tesla.

The deconvolution of ^{29}Si MAS NMR spectra for Costişa samples (Table 3) revealed the presence of 4 lines, corresponding to different types of arrangement around the silicon nuclei: Q^2, Q^3, Q^4 in amorphous state, with a sweep with between 6.96 and 12.87 ppm, as well as a Q^4 narrow line, showing a well ordered state, probably crystalline, with a sweep-width between 1.89 and 2.29 ppm (Table 4), attributed to the presence of quartz [13]. According to Presciutti et al. [13] small values of sweep-width for this line prove that the firing temperature of clays was below 900^{0}C.

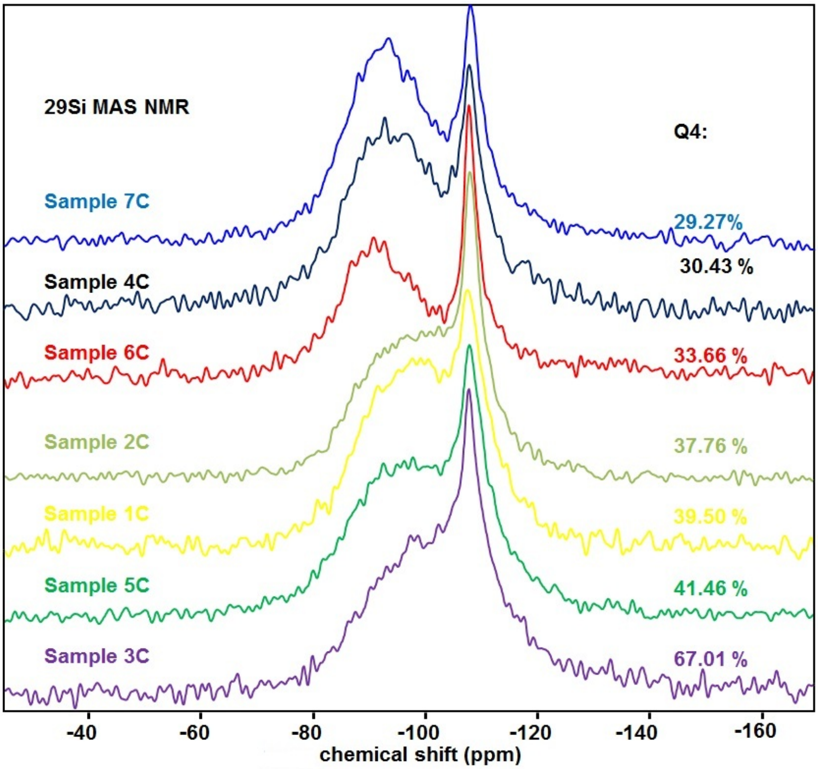

Fig. 1. ^{29}Si MAS NMR spectra of Costişa shards, ordered by total Q^4 percentage

Table 3. Q^2, Q^3, Q^4 and crystalline Q^4 percentage of Costişa shards and Q^3/Q^2 ratio

Sample	**Q^2 (%)**	**Q^3 (%)**	**Q^4 (%)**	**Q^4 cryst. (%)**	**Q^3 / Q^2**
1C	24.18	36.32	37.09	2.41	1.50
2C	29.26	32.98	28.20	9.56	1.13
3C	15.64	21.94	55.95	6.47	1.40
4C	38.11	31.46	26.32	4.11	0.83
5C	27.05	31.49	37.14	4.32	1.16
6C	38.25	28.09	20.05	13.61	0.73
7C	27.24	43.49	23.56	5.71	1.60
Average	**28.53**	**32.25**	**32.61**	**6.59**	**1.6**

Table 4. Sweep-widths corresponding to Q^2, Q^3, Q^4 and crystalline Q^4 resonance lines

Sample	**Sweep-width (ppm)**			
	Q^2	**Q^3**	**Q^4**	**Q^4 cryst.**
1C	9.67	10.76	8.52	2.25
2C	10.90	10.85	7.20	2.29
3C	10.34	10.22	12.87	2.02
4C	12.10	11.52	7.92	1.99
5C	12.02	12.60	9.08	2.04
6C	10.19	12.30	6.96	1.89
7C	9.19	11.78	8.20	1.96
Average	**10.63**	**11.43**	**8.67**	**2.06**

Figure 2 is showing an example of deconvolution, corresponding to ^{29}Si MAS NMR spectrum for the 5C shard.

The ^{29}Si MAS NMR spectrum of the sample 6C give us extreme values after deconvolution confirming that this was made of different materials than the others. This shard contains a high percentage of well-ordered Q^4, 13.63%, which can be caused by a different heat treatment.

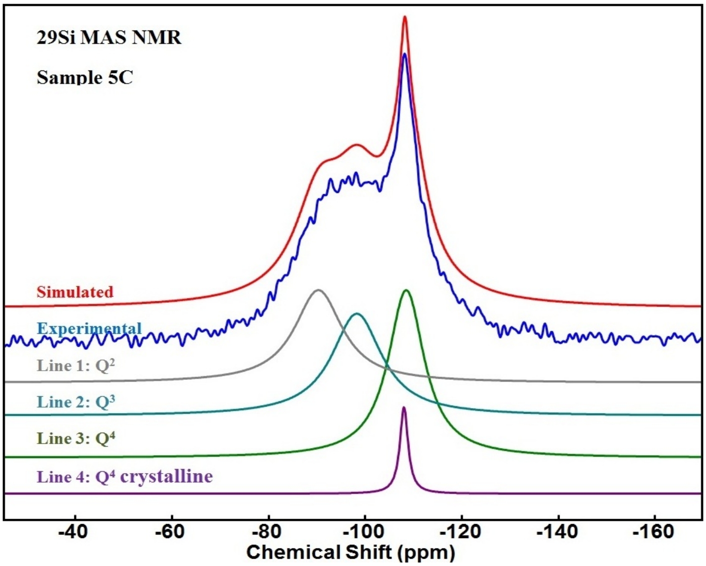

Fig. 2. Deconvolution of ^{29}Si MAS NMR spectrum of Costişa 5C shard

The sample 3C displays small quantities of Q^2 and Q^3, respectively very high percentage of Q^4, which suggest a different type o preparation. This conclusion is confirmed by the values of sweep width of Q^4 resonance line, which is completely unlike the other samples.

Sample 1C exhibit the smallest quantity of narrow Q^4 resonance (2.41 %).

It can be observed that Q^3 / Q^2 ratio could help us to distingue between Monteoru and Costişa pottery groups, as these values are lower than 1.13 for samples 2C, 4C and 6C and bigger than 1.16 for samples 1C, 3C, 5C and 7C. The difference is relatively small, meaning that this parameter has to be followed on some other samples, also. In the same time, to discriminate between these two groups we can follow the quantity of Q^4 (Fig 1 and Table 3), except for the sample 7C, a sample with extreme values for the studied modules (Table 2). The presence of Q^4 is less than 28.2% for samples 2C, 4C and 6C and bigger than 37.09% for samples 1C, 3C and 5C. In this way, the quantitative NMR analyses confirm the macroscopic observation made by archaeologists.

CONCLUSIONS

We analyzed seven shards from Middle Bronze Age pottery, found in the archaeological site from Costişa, Neamţ County, Romania.

Elemental composition was found using EDX spectroscopy and offered some suggestions about the structural and heat treatment differences between the samples.

^{29}Si MAS NMR spectra proved the differences between the samples 3C, 6C and the others. Deconvolution of the spectra made possible a quantitative analyze, observing the Q^2, Q^3 and Q^4 states of SiO_4 tetrahedra, amorphous or crystalline. Q^3 / Q^2 ratio and Q^4 quantity have different values for the Monteoru pottery group finding compared with Costişa pottery group. That confirms the macroscopic observation made by archaeologists. This paper proved that combining SEM / EDX with ^{29}Si MAS NMR spectroscopy can be a powerful tool for analyzing ancient pottery. In the same time, was demonstrated that NMR spectroscopy can make the difference between shards belonging to two different groups, produced from similar clays.

ACKNOWLEDGEMENTS

This research was co-financed by the project with the title “Social-Humanistic Sciences in the Context of Globalized Evolution: Development and Implementation of Post-Doctoral Studies and Research Program”, POSDRU/89/1.5/S/61104, project co-financed by the European Social Fund through the Sectorial Operational Programme for Human Resource Development 2007-1013.

M. Vasilescu thanks for co-financial support by Romanian PCCE 101/2008 grant.

The authors thank to Anca Diana Popescu and Radu Bajenaru, research coordinator from Costişa, for providing us pottery fragments.

REFERENCES

[1] O. Ponta, H. Mocuta, M. Vasilescu, S. Simon, Structural characterization of amorphous and nanostructurated bismuth silicate xerogels, *Journal of Sol-Gel Science and Technology,* 58, 2, 530 (2011);

[2] M. Vasilescu, G. Borodi, S. Simon, MAS NMR and SEM study of local structure changes induced by heat treatment in $La_2B_4Al_2O_{12}$, J. *Optoelectronics and Advanced Materials,* 5, 1, 153-156 (2003);

[3] M. Vasilescu, S. Simon, The local structure of bismuth-borates characterized by-11 MAS NMR, *Modern Physics Letters B*, 16, 12, 423 (2002);

[4] Donatella Capitani, Valeria Di Tullio, Noemi Proietti, Nuclear Magnetic Resonance to characterize and monitor Cultural Heritage, *Progres in NMR spectroscopy*, 64, 26-69 (2012;

[5] Neculai Bolohan, “All in One”. Issues of *Methodology, Paradigms and Radiocarbon Datings Concerning the Outer Eastern Carpathian Area, Signa Praehistorica, Studia in honorem magistri Attila Laszlo septuagesimo anno*, 229 (2010);

[6] Anca Diana Popescu, Radu Bajenaru, Rivalries and conflicts in the Bronze Age: two contemporary communities in the same space, *Dacia NS*, 52, 2008, 5-22 (2009);

[7] Lisa S. Schleicher, J. William Miller, Sarah C. Watkins-Kenney, Linda F. Carnes-McNaughton, Mark U. Wilde-Ramsing, Non-destructive chemical characterization of ceramic sherds from Shipwreck 31CR314 and Brunswick Town, North Carolina, *Journal of Archaeological Science,* 35, 2824 (2008);

[8] D. Freude and J. Kärger: NMR techniques in F. Schüth, K.S.W. Sing and J. Weitkamp (eds.): Handbook of Porous Solids, Wiley-VCH, Weinheim, 1, 465 (2002);

[9] D. Massiot, F. Fayon, M. Capron, I. King, S. Le Calvé, B. Alonso, J-O. Durand, B. Bujoli, Z. Gan, G. Hoatson, "Modelling one- and two-dimensional Solid State NMR spectra", *Magnetic Resonance in Chemistry*, 40, 70 (2002);

[10] M. Maier, V. Parvulescu, M. Tamasan, M. Vasilescu, R.F.V. Turcu, H. Mocuta, S. Simon, Structural Studies of Mesoporous Alumina, *Studia UBB Physica*, LIII, 2, 31 (2008);

[11] I. Sandu, V. Cotiuga, A.V. Sandu, A.C. Ciocan, G.I. Olteanu, V. Vasilache, New Archaeometric Characteristics for Ancient Pottery Identification, *International Journal of Conservation Science,* 1, 2, 75, (2010);

[12] I. Sandu, V. Vasilache, F.A. Tencariu, V. Cotiugă; Scientific Conservation of the Ceramic Artefacts, „Al.I.Cuza” University Publishing House, Iaşi, 2010;

[13] F. Presciutti, D. Capitani, A. Sgamellotti, B.G. Brunetti, F. Constantino, S. Viel, A. Segre, „Electron Paramagnetic Resonance, Scanning Electron Microscopy with Energy Dispersion X-ray Spectrometry, X-ray Powder Diffraction, and NMR Characterization of Iron-Rich Fired Clays”, *J. Phys. Chem.* B, 109, 22147-22158 (2005).

STUDIA UBB PHYSICA, Vol. 57(LVII), 2, 2012, pp. 91-98
(RECOMMENDED CITATION)

STUDY OF LYOPHILIZED FIBRINOGEN, COLLAGEN AND SERUM ALBUMIN BY FOURIER TRANSFORM INFRARED SPECTROSCOPY

K. MAGYARI[a], L. BAIA[a,*], O. POPESCU[b, c], V. SIMON[a]

ABSTRACT. The average secondary structure content of proteins is often evaluated by FTIR spectroscopy. This study is focused on discussing the assessment of the secondary structure of lyophilized bovine serum albumin, fibrinogen and collagen proteins using amide I FTIR band analysis. The comparison of the obtained results with other data reported in the literature warns on the limited reliability of the quantitative information about protein secondary structure extracted from the analysis of the infrared spectra.

Keywords: *FTIR, protein secondary structure*

INTRODUCTION

Interactions of proteins with biomaterials in recent years have become an intensely studied topic because of three main reasons: (1) protein adsorption on the biomaterial surface as biocompatibility indicator [1, 2]; (2) surface functionalization with proteins in order to improve the living cells contact with biomaterials [3]; (3) obtaining of new composite biomimetic materials [4].

In all these studies the most common proteins are serum albumin, fibrinogen and collagen. Serum albumin is the most abundant protein in the circulatory system. The three dimensional structure of bovine serum albumin (BSA) is believed to be very similar to the human serum albumin [5], so in most studies BSA was used [5-8]. It is a globular protein with the molecular mass of 67 kDa. The albumin structure is

---

[a] Babes-Bolyai University, Faculty of Physics & Interdisciplinary Research Institute on Bio-Nano-Sciences, 400084 Cluj-Napoca, Romania

* Corresponding author: lucian.baia@phys.ubbcluj.ro

[b] Babes-Bolyai University, Molecular Biology Center of Interdisciplinary Research Institute on Bio-Nano-Sciences, 400271 Cluj-Napoca, Romania

[c] Romanian Academy, Institute of Biology, 060031 Bucharest, Romania

predominantly helical, approximately 65 %, with the remaining polypeptides occurring in turns and extended or flexible regions between subdomains [9]. The next major protein is globulin, and the third one is fibrinogen, which plays a vital role in regulation of both haemostasis and thrombosis. Human plasma fibrinogen is a 340 kDa dimeric protein. The simplest fibrinogen model comprises three spherical regions, one E domain and two D domains, connected by two narrow rods [1, 2, 10]. The protein has two sets of three non-identical polypeptide chains, held together with disulfide bonds [1, 2, 10]. The amino termini of all six α, β and γ chains fold in the central E domain and the carboxyl termini of the two sets of β and γ chains folds into the two outer D domains [10]. The coiled-coil connector regions between the E and each D domain correspond to the α-helical structure of the three intertwined chains [1, 2, 10].

Due to biodegradability, biocompatibility and role in tissue formation the collagen has long been used as material for biomedical applications [11]. Collagen fibres provide tensile strength and rigidity to a variety of tissues such as bone, tendons, cartilage, skin, and blood vessels [12]. The essential role of collagen is the cell proliferation and differentiation, although the types of collagen responsible for cell proliferation are not yet identified [13]. Actually it was reported to be referenced about 30 types of collagen [14]. The characteristic structure of collagen is right-handed triple helix. Collagen consists of three polypeptide chains, each one composed of at least one gly-X-Y sequence structured in left-handed α helices. These three α-helices organized together form the triple helix [14].

The conformation of proteins would be changed when they are adsorbed onto surface, which has a great effect on the biological activity of substrate materials [15]. FTIR spectroscopy is the most largely used method for the investigation of protein conformation [1, 2, 5, 6, 10, 14]. For investigation of protein secondary structure content the most commonly used spectral region is that of amide I (1700–1600 cm^{-1}), primarily due to its strong signal [16, 18]. The protein solutions are prepared with soluble lyophilized proteins. Before the attachment of the proteins on material surface it is necessary to know the proteins conformation.

Therefore, the aim of this study was to determine the secondary structure of lyophilized proteins by FTIR spectroscopy. The obtained results were compared with results from the literature.

EXPERIMENTAL

Materials

Lyophilized bovine serum albumin (BSA), bovine plasma fibrinogen and calf skin collagen type I were purchased from Sigma-Aldrich.

Methods

FT-IR spectra were recorded in reflection configuration in the range of 4000-400 cm^{-1} with the spectral resolution of 4 cm^{-1} using a Jasco FT-IR-6000 spectrometer. The spectra were smoothed by 5-point Savitzky-Golay smoothing function. Second-derivative spectral analysis was performed by using the JASCO Spectra Manager in order to locate the position of the overlapped components of amide I and to further assign them to different secondary structures. The bands were deconvoluted with a Gaussian band profile, a linear baseline between 1600 cm^{-1} and 1720 cm^{-1} being previously applied.

RESULTS AND DISCUSSION

The FTIR spectra obtained for BSA, fibrinogen and collagen show general characteristics for proteins (Fig. 1). The band around 1650 cm^{-1} (Fig 1A) can be assigned to amide I vibration. This vibration arises from the C=O stretching vibration with minor contribution from out-of-phase C-N stretching vibration [16]. The bands of amide II appear at 1550 cm^{-1} value (Fig. 1A). Amide II results from combination of the N-H in plan bending and the C-N stretching vibration with minor contributions from the C-O in plan bending and C-C as well as N-C stretching vibrations [10, 16]. The absorption signal located in the 1490-1460 cm^{-1} spectral domain (Fig. 1A) is attributed to the amide II mode that arises from the N-deuteration conversion of the amide II mode to the largely stretching vibration [16]. The amide III vibration

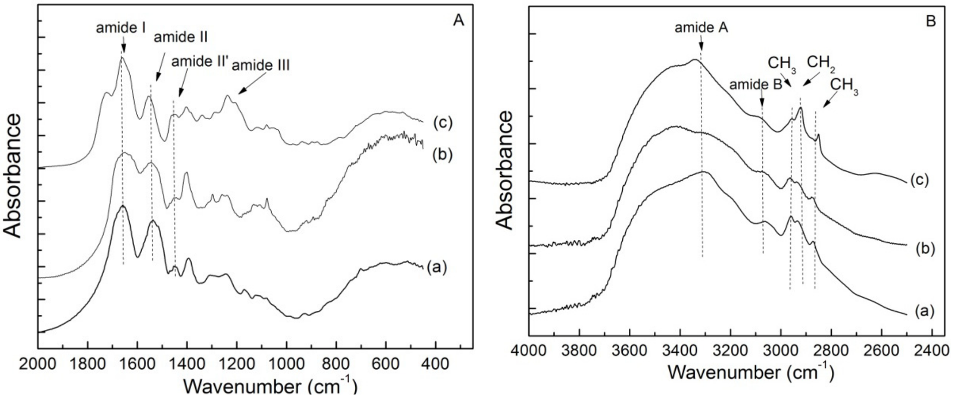

Fig. 1. FT-IR spectra of the lyophilized BSA (a), fibrinogen (b) and collagen (c) for different spectral ranges as follows: 2000–450 cm^{-1} (A) and 4000–2500 cm^{-1} (B).

occurs in the 1400-1200 cm^{-1} spectral region [1, 2, 16] and results from the N-H bending and C-N stretching vibration with small contribution from the C-O in plan bending and C-C stretching vibration [10, 16, 17]. The bands of amide A and amide B appear between 3310-3270 cm^{-1} and 3100-3030 cm^{-1}, respectively (Fig. 1B). They originate from a Fermi resonance between the first overtone of amide II and the N-H stretching vibration, and its frequency depends on the strength of the hydrogen bond [16]. Amide A and B bands of BSA occur at lower values, i.e. 3291 cm^{-1} and 3063 cm^{-1}, respectively (Fig. 1Ba). In contrast, in the case of the collagen they are shifted to the higher values, i.e. 3330 cm^{-1} and 3099 cm^{-1} , respectively (Fig. 1Bc).

The amide I band of proteins appears very sensitive to their secondary structure, therefore it is used to follow their conformational changes [16, 18]. By using amide I absorption signal of the proteins their secondary structure can be determined through different approaches. The two most common ones are: the fitting of the amide I band with component bands after identifying their position with narrowing techniques and decomposing the amide I band into basis spectra which have been calculated from a calibration sets of proteins with known structure [16]. In the present study the secondary structures of proteins were estimated based on the deconvolution of the large absorption amide I band with a Gaussian line function. The number of components and their position were determined by second-derivative FTIR spectra of lyophilized proteins. The baseline of the amide I region was adjusted from 1600 cm^{-1} to 1720 cm^{-1}. Deconvolution of the lyophilized BSA and fibrinogen amide I bands were performed assuming five components, while for the lyophilized collagen six components were considered (Fig. 2). The obtained amide I frequencies were correlated with the presence of the α-helices, β-sheets, β-turns and side chains structures. The α-helix vibrations have been shown to absorb in the 1650-1658 cm^{-1} spectral range. It should be noted that in this region the α-helical structure overlaps with random structure [16, 17]. The native β-sheets and antiparallel β-sheets conformation have spectral characteristics located in the following domains: 1623–1641 cm^{-1}, and 1674–1695 cm^{-1}, respectively [16, 17]. Absorbances between 1662–1686 cm^{-1} have been assigned to the β-turns, or turns by some investigators [1, 2, 10, 16-18].

The percentage of each component was calculated according to the corresponding integrated area (Fig. 3). The obtained values were compared with data reported in the literature [2, 14, 19-21]. In the case of BSA the values indicated in Fig. 3a were calculated from the FTIR spectra of lyophilized BSA. The values of α-helix component are almost identical, but for the β-sheet and β-turns components the deviation is much larger. This may occur due to the bands overlapping.

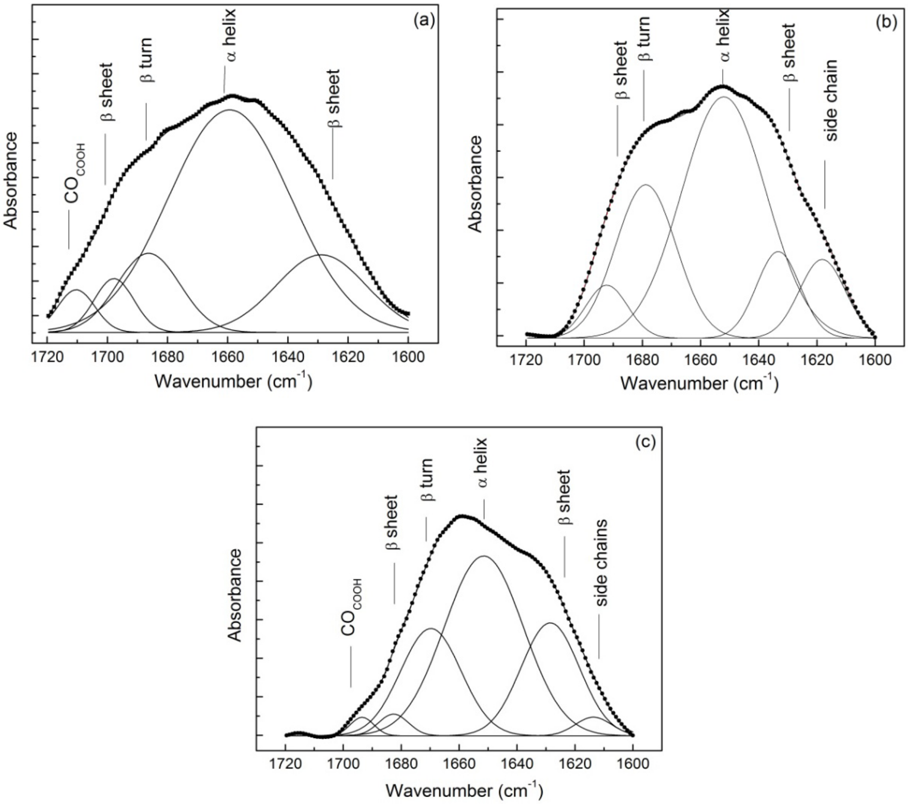

Fig. 2. Deconvolution of the amide I (1700–1600 cm−1) absorption band of lyophilized BSA (a) fibrinogen (b) and collagen (c) with Gaussian line function.

The values obtained for the secondary structure of lyophilized fibrinogen show a much larger deviation (Fig. 3b). Lin at al. [21] obtained these values from FTIR spectra of lyophilized fibrinogen too, and Tunc et al. [2] from FTIR spectra of fibrinogen in solution. The fibrinogen is more sensitive to environmental changes; in lyophilized form should be stored at -20°C. The large variation in the value of secondary structure of fibrinogen obtained by the different groups occurs due to overlapping bands and due to the environmental changes the protein is being exposed.

The secondary structure of collagen is more complex. The literature is not unified; some groups introduced triple helix structure with spectra located at 1638 cm^{-1} [14]. The secondary structure content for lyophilized collagen investigated in our study was calculated with the model used for the other proteins, and the data point out a difference for α-helix component, while the values of β-sheet and β-turn components are almost identical (Fig. 3c).

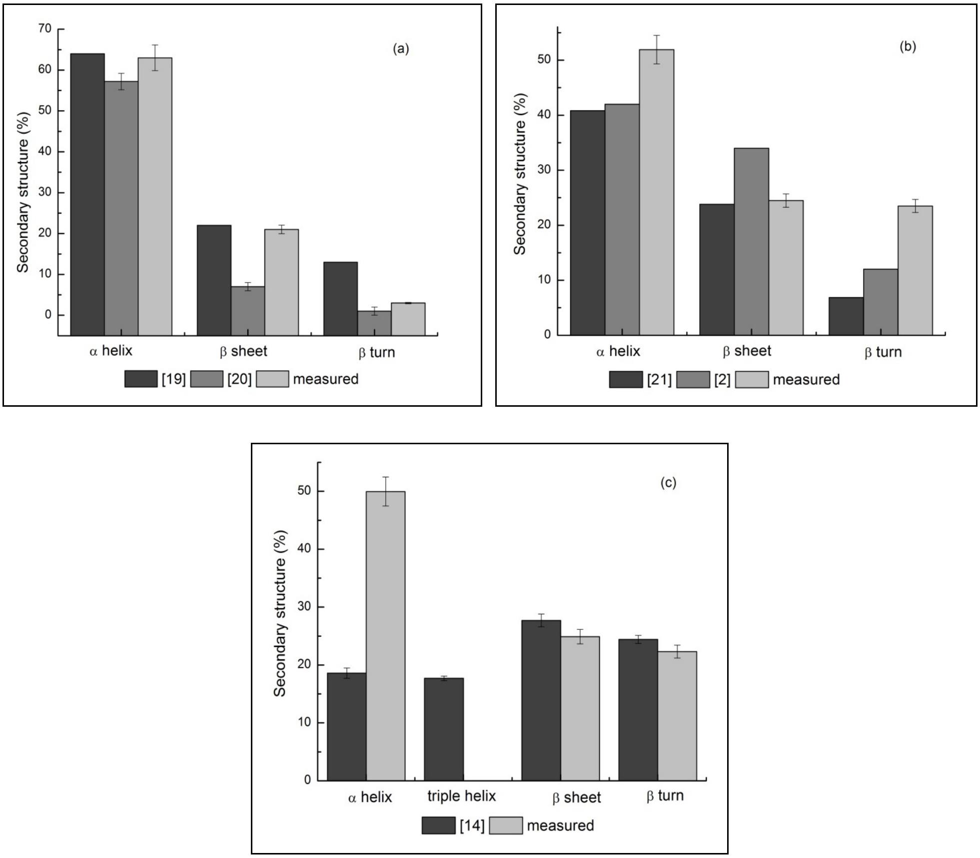

Fig. 3. Distribution of α helix, β sheet and β turn secondary structures in lyophilized BSA (a), fibrinogen (b) and collagen (c).

According to other reported studies [22, 23] the approach of representing the percentages of the particular secondary structure using the relative band area for each components of the band is not rigorously at all, because excitation coefficient for different secondary structures may be different among proteins and within a single proteins and extensive regions would produce sharp bands at characteristic predictable frequencies. Comparing the obtained results with results from the literature we can conclude that this approach can be successfully used for proteins with great stability. Otherwise, the deconvolution of FTIR spectrum in the region of amide I can be used only as qualitative information without representing the percentages of the secondary structure components.

CONCLUSIONS

The secondary structure content of lyophilized bovine serum albumin, fibrinogen and collagen was quantitatively assessed using amide I FTIR band analysis, based on percentage corresponding to the area under the deconvolution components. The comparison of the obtained results with other data reported in the literature denotes a limited accuracy of the quantitative information, which could arise from the overlapping of the bands as well as from the changes in the protein environment in solutions.

ACKNOWLEDGMENTS

This work was possible with the financial support of the Sectoral Operational Program for Human Resources Development 2007-2013, co-financed by the European Social Fund, within the project POSDRU 89/1.5/S/60189 with the title „Postdoctoral Programs for Sustainable Development in a Knowledge Based Society”.

REFERENCES

1. G. Steiner, S. Tunc, M. Maitz, R. Salzer, *Anal. Chem.,* 79, 1311 (2007)
2. S. Tunc, M.F. Maitz, G. Steiner, L. Vazquez, M.T. Pham, R. Salzer, *Colloids Surf. B: Biointerface,* 42, 219 (2005)
3. R.A. Latour, Biomaterials: Protein-Surface Interaction, in Encyclopedia of Biomaterials and Biomedical Engineering (eds. Gary L. Bowlin, Gary Wnek), Informa Healthcare Publ., New York, 2005
4. C. Xu, P.Su, X. Chen, Y. Meng, W. Yu, A. P Xiang, Y Wang, *Biomaterials,* 32, 1051 (2011)
5. G. Falini, E. Foresti, I. G. Lesci, B. Lunelli, P. Sabatino, N. Roveri, *Chem. Eur. J.,* 12, 1968 (2006)
6. K. Magyari, O. Popescu, V. Simon, *J. Mater. Sci: Mater. Med.,* 21, 1913 (2010)
7. E. Mavropoulos, A. M. Costa, L. T. Costa, C. A. Achete, A. Mello, J. M. Granjeiro, A. M. Rossi, *Colloids Surf. B: Biointerface,* 83, 1 (2011)
8. N. Nabian, M. Jahanshahi, S. M. Rabiee, *J. Mol. Struct*., 998, 37 (2011)
9. D.C. Carter, J.X. Ho, Structure of serum albumin in Advances in Protein Chemistry: Lipoproteins, Apolipoproteins, and Lipases, Academic Press INC, San Diego, 1994
10. Q. Yang, Y. Zhang, M. Liu, M. Ye, YQ. Zhang, S. Yao, *Anal. Chim. Acta,* 597, 58 (2007)
11. D Eglin, S. Maalheem, J. Livage, T. Coradin, *J. Mater. Sci: Mater. Med.,* 17, 161 (2006)

12. R. Salsas-Escat, C. M. Stultz, *Proteins: Struct. Funct. Bioinform.,* 78, 325 (2010)

13. Y. Maehata, S. Takamizawa, S. Ozawa, K. Izukuri, Y. Kato, S. Sato, M.-C.-il Lee, A. Kimura, R.-I. Hata, *Matrix Biology,* 26, 371 (2007)

14. K. Belbachir, R. Noreen, G. Gouspillou, C. Petibois, *Anal. Bioanal. Chem*., 395, 829 (2009)

15. K. Wang, C. Zhou, Y. Hong, X. Zhang, *Interface focus,* 2, 259 (2012)

16. A. Barth, *Biochim. Biophys. Acta,* 1767, 1073 (2007)

17. K. Magyari, L. Baia, O. Popescu, S. Simon, V. Simon, *Vib Spec,* 62, 172 (2012)

18. K.K. Chittur, *Biomaterials,* 19, 357 (1998)

19. T. Maruyama, S. Katoh, M. Nakajima, H. Nabetani, T.P. Abbott, A. Shono, K. Satoh, *J. Membr. Sci.,* 192, 201 (2001)

20. P. Sabatino, L. Casella, A. Granada, M. Iafisco, I.G. Lesci, E. Monzani, N. Reveri, *J. Coll. Inter. Sci*., 314, 389 (2007)

21. S.Y. Lin, Y.S. Wei, T.F. Hsieh, M.J. Li, *Biopolymers,* 75, 393 (2004)

22. M.A. Bryan, J.W. Brauner, G. Anderle, C.R. Flach, B. Brodsky, R. Mendelsohn, *J. Am. Chem. Soc.,* 129, 7877 (2007)

23. P. Schwinte, J.-C. Voegel, C. Picart, Y. Haikel, P. Schaaf, B. Szalontai, *J. Phys. Chem. B,* 105, 11906 (2001)